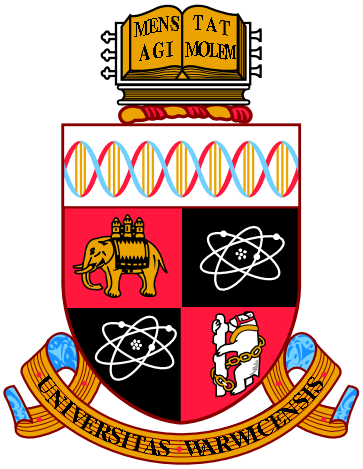

Low Frequency Strip Waveguide Array for Flow Measurement in Hostile Environments

by

Michael Richard Laws

Thesis

Submitted to the University of Warwick

for the degree of

Doctor of Philosophy

Physics

June 2015

THE UNIVERSITY OF WARWICK

Contents

List of Figures

Acknowledgments

First of all I would like to thank Dr Nishal Ramadas and Professor Steve Dixon for all of the help and support they have given me during my PhD and the many amazing opportunities they have provided me with. I would also like to thank Larry Lynnworth for his advice and input as well as Elster Instromet for the support they have provided for my project.

A big thank you goes out to everyone else, both within the Warwick Ultrasound Group and that I have had the pleasure of sharing an office with. Special mentions go to: Sam Hill, for both his constant EMAT advice and constant entertainment in the office; Kevin McAughey, for all the help both with MATLAB and finding a never ending supply of funny videos and of course to Tobias Eriksson, for both our many collaborations and our many "romantic holidays".

I would also like to thank my parents for their support and encouragement over the years. Finally, I would like to thank Anna for putting up with me constantly talking about work and always making me smile, even on my worst days.

Declarations

I declare that the work presented in this thesis is my own except where stated otherwise, and was carried out entirely at the University of Warwick during the period between October 2011 and June 2015, under the supervision of Prof. Steve Dixon and Dr. Nishal Ramadas. No part of this work has been previously submitted to this or any other academic institution, for admission to a higher degree. Parts of this work have been published as journal submissions, a complete list of these publications is given in the introduction to this thesis.

Abstract

A low frequency, waveguide array transducer, for operation in hostile environments, is studied and optimised for operation in fluids. The design consists of multiple stainless steel, rectangular cross-section strips which are used to support Lamb-like guided waves, which with appropriate delays allows the steering of the emitted beam.

Wave propagation within the waveguide strips is discussed and the effect of the strip geometry on the supported wave modes is studied using comprehensive finite element modelling that is validated experimentally. Deviations from Lamb wave behaviour is observed due to coupling that occurs across the finite width of the strip, leading to dispersive behaviour that is slightly different to that of Lamb waves in a plate of the same thickness. As a result of this study, suggestions are made for modifications to the waveguide geometry that may favourably change this dispersive behaviour, over a desired frequency range.

The effect of thermal gradients on the propagation of ultrasonic waves within the waveguide strips is also studied. Using Lamb waves as a basis for the analysis, general trends in the wave behaviour were identified before a series of experiments were conducted to demonstrate similar effects in the waveguide strips. Computational fluid dynamics models were also used to study the heat distribution within the waveguide strips of the transducer to allow the influence of these effects in a practical application to be assessed.

Finally, the phased array capabilities of the strip waveguide array transducer were demonstrated. Initially, finite element modelling was conducted to allow the optimisation of the array geometry before the construction of a prototype. Using this prototype and a custom low frequency phased array controller, experimental steering of the beam emitted from the transducer was demonstrated up to angles of 45°.

Abbreviations

2D-FFT	Two-Dimensional Fast Fourier Transform
CFD	Computational Fluid Dynamics
CMUT	Capacitive Micromachined Ultrasonic Transducer
EMAT	Electromagnetic Acoustic Transducer
FE	Finite Element
FPGA	Field Programmable Gate Array
FWHM	Full Width at Half Maximum
IR	Infra-Red
ITMF	In-Line Thermal Mass Flow
LF-PAC	Low Frequency Phased Array Controller
MEMS	Microelectromechanical System
NDT	Nondestructive Testing
PZT	Lead Zirconate Titanate
SAFE	Semi-Analytical Finite Element

Chapter 1

Introduction

1.1 Motivation

Accurate flow measurement is vital for the modern world, from ensuring that the correct amount of oil and gas arrives in international pipelines, to monitoring blood flow inside the human body during medical procedures. Due to the variation in both the types of fluids that must be monitored, and the scale at which they must be measured, many different techniques have been developed, each with their own range of benefits and limitations. One increasingly common technique uses the delays in the arrival time of a pair of ultrasonic signals to obtain information about the fluid flow. This method of flow measurement has many advantages, such as a large turn down ratio (the ratio of the maximum and minimum flow that can be measured accurately for a specific application), zero pressure drop through the flow meter and a lack of moving parts, making ultrasonic measurement techniques highly appealing.

However, ultrasonic techniques are not without their limitations. These types of flow meters usually contain piezoelectric materials, such as lead zirconate titanate (PZT), which are used to generate and detect ultrasonic waves. These materials are quite sensitive to ambient conditions, such as temperature. At high temperatures the piezoelectric constants of the ceramic decrease, causing a loss in sensitivity and

may eventually lead to the PZT becoming depoled, and ceasing to function entirely.

The a common approach to solving this issue involves placing a buffer between the sensitive piezoelectric element and the hostile environment to thermally isolate the PZT. Several constraints are immediately placed on the design of such a buffer from conception. Firstly, the target environment; the buffer material must be robust enough to survive in the extreme temperatures, high pressures and potentially corrosive conditions of the test fluid. Secondly, the buffer must suitably isolate the sensitive piezoelectric element from the target environment, while retaining a reasonable size (say below 500 mm length) which constrains the material selection based on its thermal conductivity. These criteria usually limit the possible material selections to either a metal or a high temperature ceramic, with titanium and stainless steel being commonly chosen [12]. Additionally, for many applications it is desirable that the addition of the thermal buffer has a minimal impact on the transmitted ultrasonic waves, both in terms of pulse shape and amplitude. This limits the modifications that would be required to the standard data processing techniques that are used to obtain the flow information from the measurements. It is therefore common to design the buffer in such a way that it can support guided waves, with minimal dispersion. This is usually achieved using designs based on two geometries: either thin rods or thin plates [1–7]. These constraints will for the basis of the transducer design discussed in this thesis.

1.2 Aims and Contributions to the Field of Ultrasonics

In this work a waveguide transducer has been developed using a bundle of parallel, rectangular cross-section waveguide strips, for use as a buffer in an ultrasonic transducer for flow applications. Such waveguides should support Lamb like guided waves, with dispersive characteristics due to the similarity between the width of the waveguide and the wavelengths of the waves propagating along them. This effect

has been studied together with the influence of the waveguide geometry on the propagation of ultrasound. This will assist in the design of such waveguides, allowing optimisation of the waveguide to suit ultrasonic waves of a particular frequency, for each specific application.

In addition to the protection provided by the thermal buffer, the multiple waveguide strip design can facilitate the operation of the transducer as a phased array. Ultrasonic waves may be generated in each of the strips individually with arbitrary delays. This provides the possibility of steering the emitted wave front, allowing both electronic correction of the beam path in high flow conditions and the ability to interrogate multiple paths through the test fluid using only a single pair of transducers. Due to the low wave velocities and frequencies often associated with operating in fluids, such as air, constructing a phased array transducer which satisfies the traditional array design rules is difficult; large piezoelectric elements are often required with a small array pitch. The use of waveguides in the transducer presented in this thesis allows the array to approximately satisfy these constraints, at frequencies as low as 150 kHz operating in air. The geometry at the radiating face may be different from the geometry at the other end of the waveguides where the piezoelectric material is mounted. This allows for both a simpler construction and improvements to the beam profile from the array.

1.3 Outline of Thesis

This thesis is divided into nine chapters. Following from the introduction there will be three chapters which lay the foundations for this work. Due to the diverse nature of this background material it has been separated for simplicity, covering the fundamental principles of industrial flow measurement, generation and detection of ultrasonic waves, and wave propagation. The next four chapters discuss the both the modelling and experimental work conducted for this thesis, followed by some

final conclusions.

In Chapter 2, a general introduction to industrial flow measurement will be given. In this chapter a range of current flow measurement techniques will be discussed, including mechanical, electromagnetic, thermal and ultrasonic methods. From this, the benefits offered by the use of ultrasonic methods will be demonstrated, as well as highlighting the issues with current methods, many of which may be dealt with using the transducer that will be described in this work.

Chapter 3 introduces several of the most common methods of generating and detecting ultrasonic waves. The primary focus of the chapter will be on the use of piezoelectric materials as this is the most common method used in the work. However, other techniques which rely on electromagnetic effects and lasers will also be discussed. This chapter aims to give an introduction to both the operating principles of each of these methods as well as the strengths of each method, factors which were considered when determining which techniques to use in each experimental section of this thesis. Ultrasonic arrays will also be introduced in this chapter detailing the theory of generation using an array transducer and the design constraints which will be used later in Chapter 8.

Analytical models of the propagation of ultrasonic waves will be discussed in Chapter 4. This will begin with the general case of propagation of waves in bulk solids and fluids. This will then be developed into a description of Lamb waves. This model will be used as a simplified version of the waveguide strips used in the array transducer, allowing the general trends in wave propagation for the more complex strip waveguides to be identified. This chapter will also introduce dispersion curves, a clear understanding of which will be essential for the following chapters.

In Chapter 5, dispersion in the waveguide strips is discussed. Using finite element modelling to gain insights into the wave propagation behaviour. Details of the finite element study and the technique by which the dispersion curves were extracted will be given. From this a series of models will be discussed, in which the

influence of the strip geometry on propagation within the waveguides was studied. Additionally, experimental validation of these finite element models is also presented.

Thermal effects on the propagation of guided waves will be discussed in Chapter 6. The thermal gradient that would be produced along the length of the waveguide strip will cause variations in wave speed. To begin, an analytical model of a heated plate was used to identify the general trends expected in the behaviour of the guided waves, followed by an experimental study of with a single strip with a range of thermal gradients along the length. In addition to this, a computational fluid dynamics model will be discussed, which was used to identify any variation between the individual strips in the array when heated, as this could interfere with the phased array operation of the array.

In Chapter 7 the design of a matching layer for this transducer is discussed. The use of a stainless steel waveguide allows the isolation of the piezoelectric elements from the test fluid. However, it also causes a large mismatch in acoustic impedance, between the waveguide material and the target fluid. Several materials are suggested as potential matching layers, with both a suitable acoustic impedance and thermal resistance. These materials were then characterised and their properties tailored, forming a composite material by loading them with other materials in order to optimise transmission into water, which was selected as a test fluid. Each of the materials was then evaluated in terms of their effectiveness as a matching layer, using both finite element modelling and experimental measurements.

In Chapter 8, the capabilities of the waveguide transducer to function as a phased array transducer in air is presented. This includes a finite element model of the array which was used to allow the pitch of the waveguide elements to be optimised by studying the directivity of the array, before constructing a prototype. A set of custom phased array electronics, designed for use with low frequency transducers will then be described. These custom electronics were required, as commercially available phased array systems are not designed for the low frequencies at which the

transducer described in this work operates. These electronics were combined with a prototype strip waveguide array transducer to demonstrate the beam steering capabilities of the array experimentally.

Finally, in Chapter 9 some overall conclusions will be drawn, along with suggestions of potential developments which could be made based on the work presented in this thesis.

1.4 Publications Arising from the Thesis

1. M. Laws, S. N. Ramadas, S. Dixon, and L. C. Lynnworth, *A Strip Waveguide Array Transducer for Fluid Coupled Applications,* IEEE Transactions on Ultrasonics, Ferroelectrics, and Frequency Control, (*Submitted March 2015*)

2. M. Laws, S. N. Ramadas, S. Dixon, and L. C. Lynnworth, *Parallel strip waveguide for ultrasonic flow measurement in harsh environments,* IEEE Transactions on Ultrasonics, Ferroelectrics, and Frequency Control, vol. 62, no. 4, p. 697 - 708, 2015.

3. M. Laws, S. Ramadas, and S. Dixon, *Matching layers design for a plate waveguide ultrasonic transducer for flow measurement in hostile environments,* in Proceedings of 2014 IEEE International Ultrasonics Symposium, pp. 2498 - 2501, 2014.

4. M. Laws, S. Ramadas, and S. Dixon, *High temperature studies of a rectangular cross-section waveguide for flow measurement applications,* in 14th Asia Pacific Conference on Non-Destructive Testing Proceedings, 2013.

5. M. Laws, S. Ramadas, and S. Dixon, *Thermal studies of a plate bundle waveguide for use as an ultrasonic flow meter buffer,* in Proceedings of 2013 IEEE International Ultrasonics Symposium, pp. 1618 - 1621, 2013.

6. M. Laws, S. Ramadas, and S. Dixon, *A plate waveguide design for ultrasonic flow measurements in hostile environments,* in Proceedings of 2012 IEEE International Ultrasonics Symposium, pp. 1718 - 1721, 2012.

7. M. Laws, S. Ramadas, and S. Dixon, *A plate waveguide for ultrasonic flow measurements in hostile environments,* in Review of Progress in Quantitative Nondestructive Evaluation, pp. 1512 - 1517, 2012.

Chapter 2

Flow Measurement Techniques

2.1 Overview of Flow Measurement Techniques

We shall begin here with a brief description of several of the most common types of non-ultrasonic flow meters used in industrial settings. A brief introduction to the operating principle of each type will be given, along with the types of applications where such a meter may be used. Additionally the advantages and disadvantages of each type of meter will also be discussed.

2.1.1 Orifice Plates and Venturi Meters

An orifice plate is one of the simplest types of flow meter, from a conceptual stand point. Such a flow meter consists of a plate with a precisely machined hole, which has a diameter smaller than that of the pipe. This causes a convergence of the flow before the plate, creating a jet through the hole in the orifice plate. The jet will continue to converge towards the centre of the pipe for a small distance after passing through the plate, due to the residual inward momentum retained by the fluid. This forms a region known as the vena contracta, where the diameter of the stream is at a minimum. Outside of the area which contains the jet, large vortices are established, forming a recirculation zone [13, 14]. The flow profile eventually

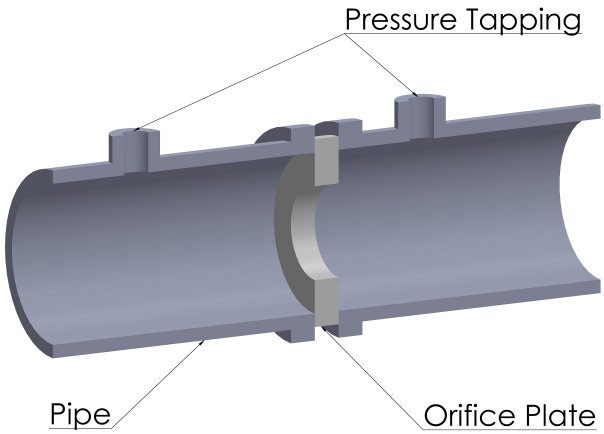

Figure 2.1: A schematic diagram of a classical orifice meter.

recovers further downstream; however there is usually a substantial pressure loss. The mass flow rate can then be obtained by taking two pressure measurement. The first measurement is taken one pipe diameter before the plate, as the plate should have a minimal effect on the flow at this distance. The second pressure measurement is usually taken at a distance of half a pipe diameter after the plate, which would be inside the recirculation zone. The mass flow rate can then be calculated from the pressure drop between these two measurements [13].

Orifice plate based flow meters may be used with most single phase Newtonian fluids and some multi-phase fluids [15]. The use of orifice plates with multi-phase fluids is limited by the design of the flow meter. As mentioned previously, there are several regions around the plate where large vortices are established due to the motion of the fluid through the plate. If the multiple phases in the fluid are significantly different one of the phases may be preferentially trapped in these vortices, causing the phases to separate. In addition, the relative simplicity of the design and the detail in which it has been studied makes it is possible to calculate the an uncertainty for the measured flow rates without the need for calibration. The

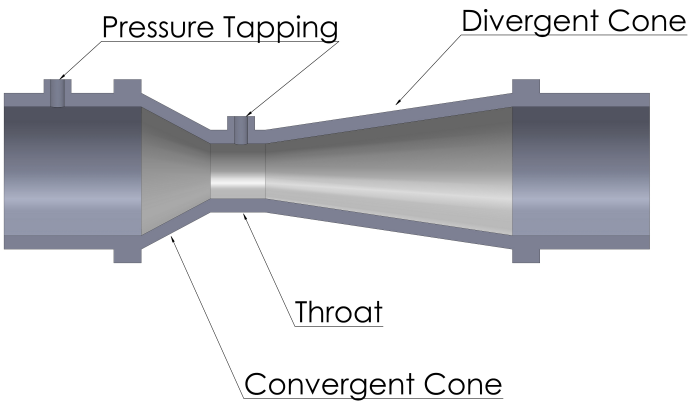

Figure 2.2: A schematic diagram of a classical Venturi meter.

small size of the plate also makes the addition of such a flow meter into a pipeline relatively simple. To ensure the accuracy of the measurements the dimensions of the hole in the orifice plate must be well known, and any damage to this plate, such as from an abrasive fluid or corrosion with time, will significantly reduce the accuracy of the measurements. The large pressure drop across the plate can also be a limiting factor in the viability of using an orifice plate, as this will lead to large energy losses.

Venturi meters also measure mass flow rate by means of a pressure variation, but the design of a such a meter is more complex. A Venturi meter consists of two cones: the first cone causes the flow to converge, typically with an angle of around 20°. This cone gradually reduces the diameter of the pipe until it reaches the mid-section of the meter, known as the throat which has a fixed diameter. Following the throat is a divergent cone, which returns the pipe diameter to the original value. This second cone usually has a smaller angle than the first, in the range of 7° to 15°, allowing a gradual decrease in velocity and increase in pressure. Such a design helps to prevent the vortices formed with an orifice plate, and significantly reduces the pressure drop across the meter. As with the orifice plate, two pressure values

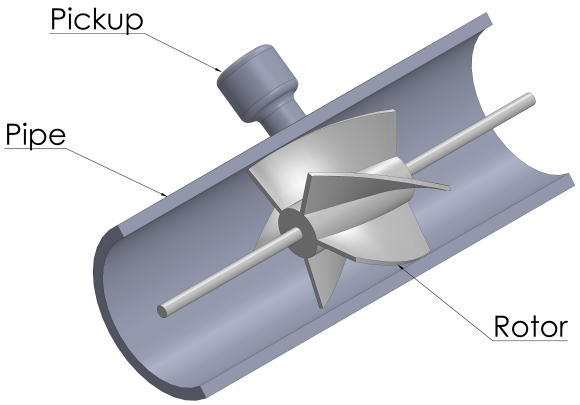

Figure 2.3: A schematic diagram of a classical turbine meter.

are measured to allow the calculation of the mass flow rate. As before, the first measurement is taken in a region before the meter, however the second pressure measurement is taken in the throat region, where the velocity is highest and the pressure variation is greatest.

Like an orifice plate, venturi flow meters may be used with a wide range of fluids, including many multi-phase fluids [16, 17]. The main advantage of this type of flow meter rather than a simple orifice plate is the conservation of energy across the meter, which can be beneficial in some applications. This comes at the cost of increased complexity, affecting both the cost of manufacture and ease of installation.

2.1.2 Turbine

A turbine meter is a mechanical flow meter that uses the energy of the fluid to drive a rotor placed in the flow [18,19]. The rate at which the rotor spins can then directly related to the flow velocity. The rate of rotation may be monitored mechanically, however it is more common to use an electromagnetic pickup to monitor the rotation to limit both the load applied to the flow and the number of parts susceptible

to mechanical wear. A range of electromagnetic methods may be used for this monitoring, including the detection of variations in a magnetic field due to the motion of the blades and optical methods where the motion of the blades physically blocks a beam of light [20,21]. Regardless of the specific technique used, the rotation of the rotor is converted into a series of electrical pulses which may then be used in the calculation of the flow velocity.

Turbine meters can be manufactured relatively cheaply and can be quite compact, when compared to other types of meters. Whilst the pressure loss across a turbine meter is less than that of an orifice plate it can still be significant [13]. The design of such a meter is also quite complex as the drag from the blades and the central hub of the rotor as well as the bearing must be accounted for in order to allow calculation of the flow [22–24]. Ultimately, the disadvantage of this type of flow meter is the susceptibility of the components to mechanical wear, leading to degradation in accuracy and eventual failure of the meter. This can be a particular issue when the fluid is of a non lubricating nature, which may lead to the need for regular maintenance.

2.1.3 Coriolis

Coriolis flow meters measure the deflection of a vibrating pipe, caused by the acceleration to the fluid moving around a centre of rotation, and are one of the few commonly used industrial flow measurement techniques which can give a direct measurement of the mass flow rate. There are a wide range of pipe geometries which have been used for coriolis meters [25,26], here we will discuss a U-shaped design for simplicity, but the underlying physics is essentially the same for other geometries. A schematic diagram, highlighting the fundamental forces involved in the operation of a coriolis meter is shown in figure 2.4. In order to measure the flow rate the fluid is diverted into the U-shaped region of pipe. This region is then vibrated about a pair of fixed points, as shown in figure 2.4, using some type of actuator. The flow of

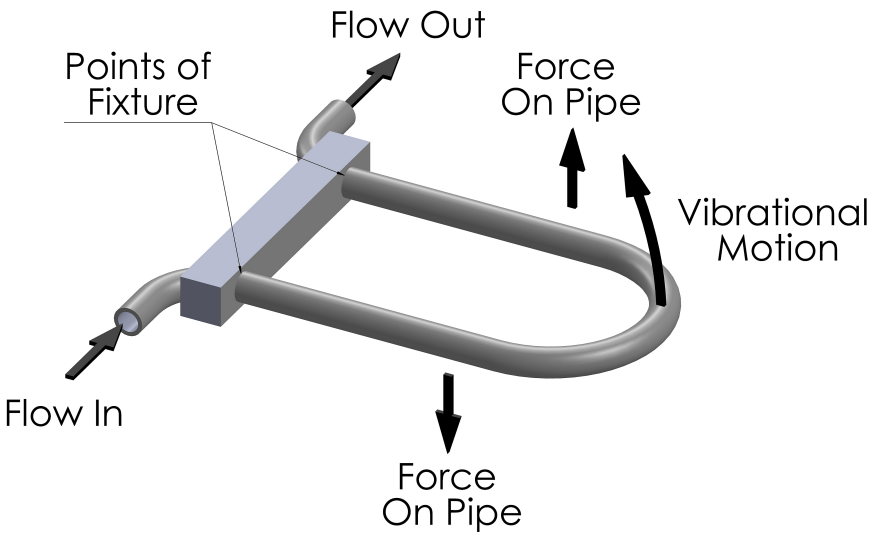

Figure 2.4: A schematic diagram of a U-shaped coriolis meter.

the fluid combined with this vibrational motion gives rise to a coriolis force, which acts in opposite directions on the two sides of the U-shaped pipe, with the first half forced down and the second half forced up, causing the pipe to twist. Of course, during the second half of the vibrational cycle both the direction of the vibrational motion and the forces will be the opposite of those shown in figure 2.4. The deflection caused by this twisting motion can be measured, often with some type of magnetic position sensor, allowing the flow rate to be measured.

Compared to turbine meters, coriolis meters are much more robust, with minimal moving parts, as both the vibrations and distortions are usually so small they cannot be noticed visually. Additionally, as coriolis meters are not affected by density variations, they are suitable for a wide range of fluids, including slurries and other fluids with a high solids content which can make them a highly valuable tool when the composition of the fluid is unknown [27,28]. Much like the previously

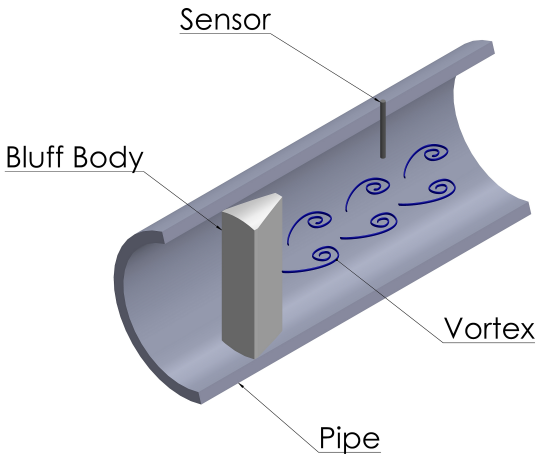

Figure 2.5: A schematic diagram of a vortex-shedding meter.

discussed meters, coriolis techniques can suffer from large pressure drops, dependent on the application [26]. Maintenance can also be an issue with some of the more complex geometries, as removing blockages in the pipes can become problematic. Large thermal variations can also change the material properties of the meter, changing the distortions, which can add uncertainty to the measured velocity, if not also accounted for.

2.1.4 Vortex-Shedding

A vortex-shedding flow meter uses instabilities in the flow due to an obstruction, in order to allow the flow to be measured. The main component in such a device is the bluff body, the obstruction which generates the vortices. A sensor, either a piezoelectric pressure sensor, an electrostatic sensor or a mechanical device, is placed behind the bluff body to monitor the passage to the vortices [29]. The number of vortices formed is proportional to the velocity of the fluid, and these are detected as pulses in the measured quantity, be it pressure, charge, displacement or some other quantity. The frequency of these pulses can then be used to calculate the flow

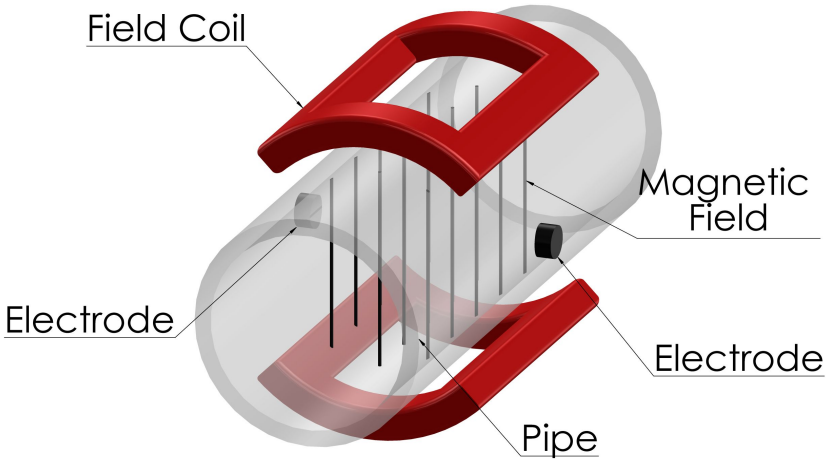

Figure 2.6: A schematic diagram of a electromagnetic meter.

velocity. A wide range of designs have been used for the bluff body, from simple cylinders to T-shapes and even more complex designs with multiple bodies [29, 30].

Low flow velocity limits the use of this type of meter, as at these velocities too few measurable vortices will be generated and the accuracy of the measurements would come into question. Vortex-shedding meters are also susceptible to errors from vibration of the pipes and pulsation of the fluid, both of which can interfere with the accurate measurement of the vortex-shedding frequency. However, if these problems can be avoided, such a meter can be a robust option for a wide range of fluids and, depending on the type of sensor used, temperatures.

2.1.5 Electromagnetic

Electromagnetic flow meters were first developed in the 1930s [31–33],but were not commonly used commercially until the 1950s [34]. Electromagnetic flow meters rely

on Faraday's law of induction to allow the measurement of the flow of a conducting fluid, with the benefit of having no moving parts and a minimal impact on the flow. Such a flow meter has two main components, a pair of field coils which generate an, ideally uniform, magnetic field through the pipe, and a pair of electrodes aligned perpendicularly to the magnetic field, as shown in figure 2.6. As the conducting fluid flows through the field a voltage is generated across the pipe between the two electrodes. The magnitude of this voltage has been shown to be linearly proportional to the mean velocity of the fluid, allowing the velocity to be easily measured by monitoring the voltage between the pair of electrodes.

For the flow meter to function correctly the pipe material must be non-magnetic (for example some type of austenitic steel) to allow the field to penetrate the pipe wall. Additionally the interior of the meter must be lined with an electrically insulating material to prevent the generated voltages from shorting. Commonly used liner materials include rubber, neoprene, PTFE and a range of other polymers and ceramics [13]. These liner materials are susceptible to wear over time, which would damage the meter, so selection of the correct liner material for the fluid is essential, though additional techniques have been developed to enhance the longevity of the liner material [35]. Another limit on the potential applications often imposed by the liner material is the operating temperature, as the most commonly used materials are only suitable up to around 200 °C [14, 36].

2.1.6 Thermal

Thermal flow meters use the thermal properties of the test fluid to determine the flow velocity. There are a range of flow measurement techniques based upon the thermal measurements. Here we will discuss only an in-line thermal mass flow (ITMF) meter, as this is one of the most common types used industrially, shown in figure 2.7. This type of flow meter has two probes which are placed into the fluid flow. One of these probes contains a heating element and a temperature probe. The second probe,

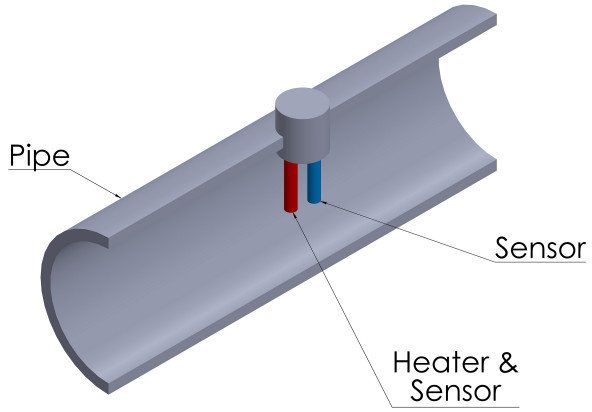

Figure 2.7: A schematic diagram of a ITMF meter.

containing only a temperature sensor, is positioned a small distance away, but often in the same pipe cross-section. The temperature difference between the two probes is measured and electronically fixed. As the fluid flow is increased a greater amount of heat is absorbed by the passing fluid, to retain the fixed temperature difference the more power must be supplied to the heater. By monitoring the power supply to the heater it is possible to calculate the mass flow rate.

The potential application of thermal flow meters is severely limited by the requirement that the thermal properties of the fluid be well known. As such, they are only commonly used for gas flows, when the composition is well known. However, when these parameters are known, thermal flow meters provide a robust method of flow measurement, with no moving parts, and accurate flow measurement, even with low velocities.

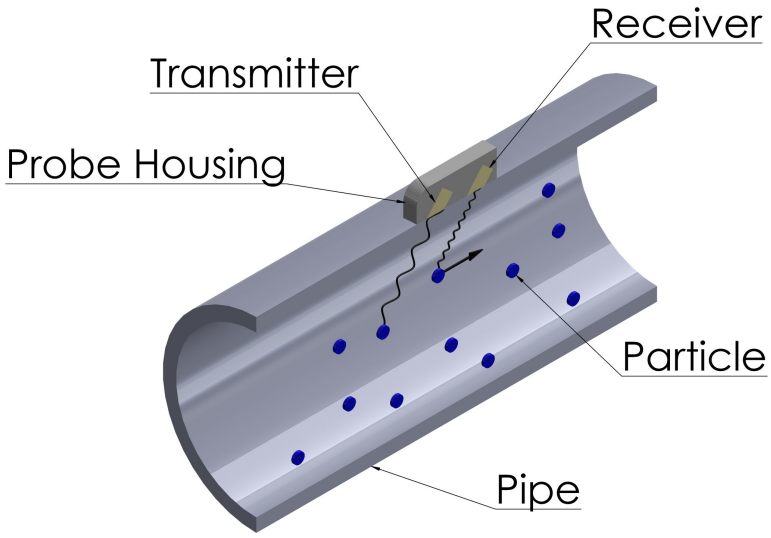

Figure 2.8: A schematic diagram of an ultrasonic Doppler meter.

2.2 Ultrasonic Flow Measurement Techniques

As the focus of this work is designing a transducer for ultrasonic flow measurement, the discussion of these techniques will be in greater depth than the previously mentioned techniques, with particular focus on the time transit technique.

2.2.1 Doppler

Doppler flow measurement is less commonly found in industrial settings, but it is worth mentioning here for completeness. This type of ultrasonic flow meter uses the Doppler effect, measuring the frequency shift of a wave reflected from a moving target, to determine the flow velocity. Such a flow meter typically has a pair of transducers, a transmitter and a receiver housed in a single probe mounted on the

outside of a pipe, shown in figure 2.8. The transmitting element generates ultrasonic waves which pass through the pipe wall and in to the fluid. For a Doppler meter to function there must be some type of reflectors in the fluid, such as gas bubbles or suspended particles, which can reflect the incident ultrasonic waves back towards the sensor. The reflected ultrasonic waves are then detected by the second transducer and the frequency shift can then be used to determine the velocity of the scatterers.

In application it is rarely this straight forward, as the reflecting particles would have a distribution of velocities, there is a range of angles at which the transmitted ultrasonic wave will interact with the particles in the fluid and additional effects due to the surrounding pipe geometry which results in a broadening of the frequency spectrum of the signal [37]. As such, the mean velocity of the fluid must be calculated form an estimation of the mean shift, accounting for these factors, which can lead to large uncertainties in the measurements. Additionally, with Doppler flow meters it can be difficult to know which region of the flow is being probed, as this is dependent on both the distribution of the reflectors and the attenuation of the ultrasonic signal. Thus, relating the velocity measured using this technique to the mean velocity of the fluid in the pipe a non-trivial issue. Another problem that may occur is that the reflecting particles may be propagating at a different velocity to the surrounding fluid.

2.2.2 Transit Time

Transit time or contrapropagation ultrasonic flow meters are far more common than Doppler meters, in industrial settings. At the most simple level, this type of flow meter also relies on a pair of ultrasonic transducers. These transducers are positioned on opposite sides of the pipe and inclined at an angle θ, as shown in figure 2.9. There are two varieties of these type of flow meters; wetted, where the transducer is in contact with the fluid, similar to the one shown in figure 2.9, and clamp-on, where the transducers are attached to the outside of the pipe. Here we will primarily be

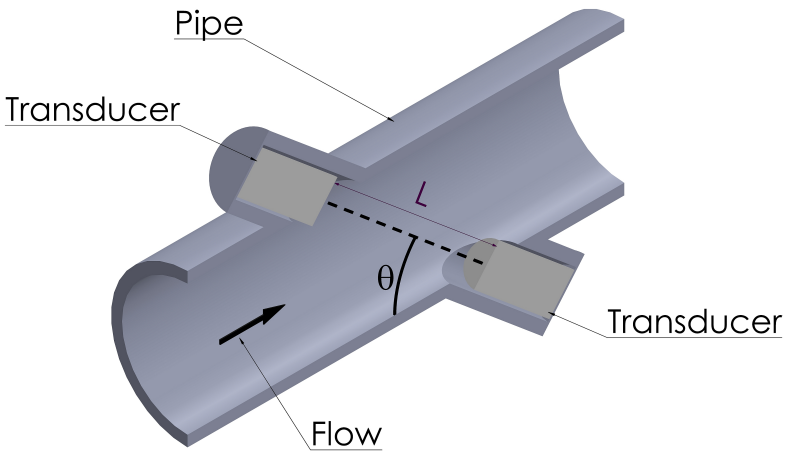

Figure 2.9: A schematic diagram of an ultrasonic transit time meter.

discussing the wetted type, but many of the details being discussed are applicable for both types.

In order to obtain a flow measurement, an ultrasonic pulse is first transmitted from one of the transducers along the path, L shown in figure 2.9, and is received on the opposite transducer, and the transit time is recorded. A second pulse is then transmitted with the roles of the two transducers reversed and a second transit time obtained. With no flow, these transit time measurements should be identical, $t = L/c$, where c is the sound speed in the fluid. However, when the fluid is in motion with a velocity v_f it can be resolved such that it has a component along path L, effectively modifying the sound velocity depending on if the ultrasonic waves are travelling upstream or downstream giving the following:

$$t_{up} = \frac{L}{c - v_f \cos\theta} \tag{2.1}$$

$$t_{down} = \frac{L}{c + v_f \cos\theta}. \tag{2.2}$$

These equations may then be combined to obtain an expression for the flow velocity:

$$v_f = \frac{L}{2\cos\theta}\left(\frac{1}{t_{down}} - \frac{1}{t_{up}}\right). \tag{2.3}$$

By eliminating the sound speed, c, from these equations the measurement becomes independent of pressure, temperature and the composition of the fluid and purely dependent on the geometry of the meter and the accuracy of the time measurements. In addition to calculating the flow velocity the two time measurements can also be used to calculate the sound speed in the fluid:

$$c = \frac{L}{2}\left(\frac{1}{t_{down}} + \frac{1}{t_{up}}\right). \tag{2.4}$$

This additional information can be used to assist in the calibration of the meter [38].

In many applications, such as the petrochemical industry, it is usually desired that the mass flow rate is obtained, rather than the flow velocity. It may seem that this may be obtained my multiplying the flow rate calculated using equation 2.3 by the cross-sectional area of the pipe, and the density of the fluid, however this would only yield an accurate value if the flow profile was uniform. In most real applications this is not the case, and as such, the velocity calculated using equation 2.3 is in fact the mean velocity of the fluid along the path L. Assuming this path crosses the centre of the pipe this can cause the mass flow rate to be over estimated by as much as 33 % [39, 40]. To obtain an accurate value for the mass flow rate an additional correction factor K must be included which compensates for the profile of the flow along the particular path. This leads to the following expression:

$$Q_m = \frac{L}{2\cos\theta}\left(\frac{1}{t_{down}} - \frac{1}{t_{up}}\right) AK\rho(P,T), \tag{2.5}$$

where Q_m is the mass flow rate, A is the cross-sectional area of the pipe and $\rho(P,T)$ is the density of the fluid, which is a function of pressure, P, and temperature, T.

Though K can be used to correct for this variation, there is still an inherent uncertainty associated with the value, due to assumptions made about the profile of the flow in the pipe. One way in which this uncertainty may be further reduced is to use transit paths offset from the centre of the pipe, which has been shown to give more accurate measurements for a range of flow profiles [41].

An additional way that the uncertainty of the measurement may be reduced is by the use of multiple pairs of transducers to take measurements along several different paths. Each of the paths will give a different velocity value. The information from these paths may then be used to obtain a more accurate representation of the flow profile, allowing more precise correction factor K to be obtained. Multiple path flow meters also allow other details about the flow to be obtained. There is no limitation to direct paths, many multiple path meters include paths with one or more reflection off the pipe wall, which allow addition features of the flow, such as swirl and asymmetry to be investigated.

The use of these techniques can allow highly accurate flow measurements to be obtained. Ultrasonic transit time techniques are also highly scalable, with wetted meters with pipe diameters of between 50 mm up to 1600 mm available from manufacturers, with even larger diameters possible with clamp-on systems. Additionally, ultrasonic transit time meters have a large turn down ratio, the variation between the maximum and minimum flow velocity that can be measured accurately, allowing a single meter to be used for a range of applications and with highly variable fluid flows. Much like Doppler, electromagnetic and thermal meters, transit time ultrasonic meters have no mechanical components, so are not susceptible to wear over time and has a zero pressure drop across the meter.

2.3 Issues with Current Ultrasonic Methods and Opportunities

Transit time ultrasonic meters are not without issue though, bubbles and particulate matter in the fluid can attenuate the ultrasonic waves, preventing the signal from being detectable at the other end of the path and making a measurement impossible, which limits the application. High flow rates can also pose an issue for transit time meters, as this can cause beam drift, where ultrasonic waves are carried in the direction of flow [42–45]. This is a particular issue in large diameter pipes and gas applications, where the sound speeds are lower and the transit times are larger, allowing the fluid velocity to have a greater effect. In many cases this beam drift will result in reduction in the amplitude detected, as only the edge of the beam will reach the detector. In more extreme cases the transmitted beam can entirely miss the transmitter. This is particularly common when there are multiple reflections in the path between the transmitter and receiver, as even a small shift in the incident angle on the pipe wall can significantly alter the beam path.

The transducer design discussed in this thesis uses an array of waveguides, allowing electronic steering of the transmitted beam. This could be used for multiple applications. Firstly, the steering could be used to correct for beam drift. This would allow the operation of the flow meter at higher flow rates, even in large pipes with low sound speed gases. Additionally, as the steering angle could be varied rapidly using a purely electronics based system, it would be possible for the flow meter to find the optimum transmission angle, automatically correcting itself when the beam begins to drift.

Ultrasonic flow measurement techniques suffer from the same issues as many ultrasonic techniques which rely on PZT based piezoelectric materials; extreme temperatures can cause damage to the active piezoelectric element. As the temperature of the PZT element is increased, its piezoelectric properties decrease, until it reaches

the Curie point for that material, a temperature at which it loses its piezoelectric properties as the ordered structure inside the material breaks down. These Curie temperatures can often be relatively high, up to 300 °C [46]. However, this value can be deceptive, as the piezoelectric properties of the material will often start to degrade far below this temperature, causing damage to the ceramic and increasing the rate of material ageing. It is generally advisable to keep the temperature of the ceramic below half of the Curie temperature [47]. The piezoelectric properties of PZT materials are also negatively affected by very low temperatures, with significant decrease in the piezoelectric constants reported for many of the commonly used PZT materials as they are reduced to cryogenic temperatures [48–50]. This provides a rather limited range of a few hundred degrees, where ultrasonic techniques may be applied. However this range may be extended through the use of a thermal buffer, as described in the previous chapter, allowing the sensitive piezoelectric element to be isolated from the fluid; the approach that is taken in this work. An alternative to the use of a buffer could be the use of a high temperature piezoelectric material. However, these materials generally are much less efficient at generating ultrasound than PZT based materials, in addition to generally being more expensive than PZT based materials, preventing their widespread use in many industrial applications. A buffer design, such as the one discussed in this work, also has the benefit of protecting the piezoelectric element from other hostile environments, such as very high pressures and corrosive fluids which could damage a standard transducer over time.

Chapter 3

Ultrasonic Transduction Techniques

There are a wide range of techniques available for generating and detecting ultrasound. When operating in a fluid however the options become much more limited. All current industrial ultrasonic flow meters rely on transducers based upon piezoelectric materials, though work is currently being conducted to investigate other possible, non piezoelectric based, transducers for ultrasonic flow metering.

Other means of ultrasonic generation, commonly used in fields such as non-destructive testing (NDT), often rely on the rigid structure and elastic properties of solid materials to allow the generation ultrasonic waves, making these techniques unsuitable for fluid based applications. However, as a solid waveguide is used in this work, it is possible to utilise some of these methods to assist in the characterisation of the waveguide strips. In this chapter several of the most common techniques of ultrasonic transduction will be discussed

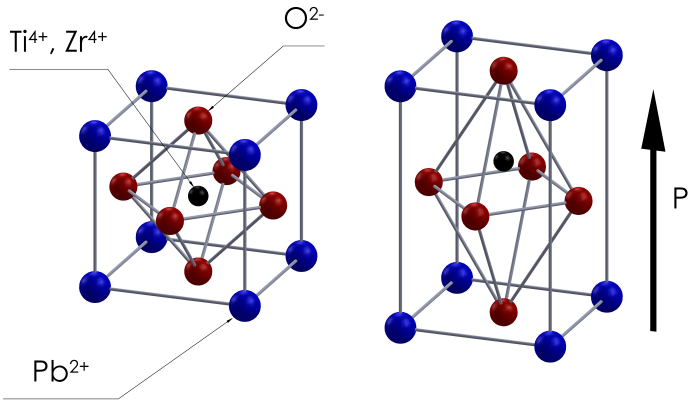

Figure 3.1: The perovskite structure of PZT. On the left, the symmetric structure of the PZT when the material is above the Curie temperature is shown. On the right the polarised PZT structure is shown. The central atom is shifted from the geometric centre of the unit cell, creating a net polarisation.

3.1 Piezoelectric Transduction

Piezoelectric based ultrasonic transducers are by far the most common type of transducer currently in use, found in a wide range of applications, including industrial flow measurement, NDT, medical imaging, sonar and ultrasonic cleaning [12,51–53]. Such widespread usage is a result of many years of study, resulting in well understood materials which can be used to make efficient, versatile and economic transducers. A piezoelectric material allows a coupling between electrical and mechanical energies, allowing an applied stress to cause a change in the polarisation of the material and vice versa. Such a material must have some asymmetry to its structure to allow the development of a spontaneous polarisation. There are twenty such crystallographic point groups which can display piezoelectric behaviour, the most well known of of which is the perovskite structure which is the structure of the commonly used PZT, shown in figure 3.1. Above a temperature known as the Curie temperature, T_C, the

structure is symmetric with no dipole moment. At lower temperatures, the structure of the unit cell changes, causing the central atom to be shifted away from the centre of the structure, imparting a dipole moment on the unit. When large piezoceramics are manufactured it normally contains some form of grain structure [54], consisting of small regions polarised in the same direction, but randomly oriented relative to the surrounding grains, resulting in no net polarisation. To make a functional device these domains must first be aligned. This is achieved by applying a large DC voltage across the ceramic in the desired poling direction, often at an elevated temperature to allow easier alignment of the individual domains [55]. The temperature of the ceramic can then be reduced while the voltage is kept fixed, leaving a polarised ceramic. Due to the initially random orientation of the grains, a perfect alignment of the individual dipoles cannot be achieved. However a good enough alignment can be achieved to give the ceramic a net polarisation. As a result, piezoceramic materials are sensitive to elevated temperatures. As the temperature is increased, individual grains can lose alignment, causing a reduction in the effectiveness of the material even below T_C, as the individual grains retain the local alignment of their polarisation, but not the net polarisation, making the material ineffective as a transducer.

When a pressure is applied to a piezoelectric material, along the axis of polarisation, it causes a distortion of the structure of the unit cell. This will in turn change the dipole moment of each of the individual cells as the positions of the positively and negatively charged atoms shift relative to one another, leading to a net build up of charge on the surfaces of the material, allowing the pressure to be measured as a voltage. This is what is known as the piezoelectric effect and is used in the detection of ultrasonic waves. In order to generate, the reciprocal process is used, applying a voltage across the material. This establishes an electric field that interacts with the dipoles in the material, generating stresses in the piezoelectric material, which can be used to produce ultrasonic waves. This is known as the inverse piezoelectric effect. These two phenomena may be described with a pair of

equations which relate the electrical and mechanical properties of the material [56]:

$$D = dT + \epsilon_T E, \tag{3.1}$$

$$S = s_E T + d^t E. \tag{3.2}$$

Here D is the electric displacement, T is the elastic stress, ϵ_T is the permittivity of the piezoelectric material under a constant stress, E is the electric field, S is the elastic strain, s_E is the mechanical compliance in a constant electric field and d^t is the transposed piezoelectric charge constant, the ratio of the applied mechanical stress and the generated electric polarisation.

Many models exist which relate the electrical input to the mechanical response of practical piezoelectric devices. This is often achieved by constructing an equivalent circuit, using some arrangement of resistors, capacitors and inductors [57–59]. One of the key points of these models is the presence of resonances at which a particular piezoelectric would most efficiently convert electrical energy to mechanical energy. The mathematical equations, and associated derivations, which describe the frequencies at which these resonances occur will be omitted here, however they may be found in many textbooks on the subject of piezoelectric materials [51, 60].

Rather than a full, quantitative, mathematical description of the origin of the resonances (which may be obtained, for example, using the equivalence circuits mentioned previously [57–59]) a brief qualitative description will instead be given, as the frequencies at which the resonances occur can be related to the geometry of the piezoelectric. As an example, a block of piezoelectric material, with a thickness L, will be considered in one dimension. When a voltage is applied to the piezoelectric block, the shaded region in figure 3.2, the sides of the disc will expand, creating waves in the surrounding medium. Inside the disc, the waves from each of the faces will propagate towards the centre of the block. When $L = \lambda/2$, half of a wavelength, the

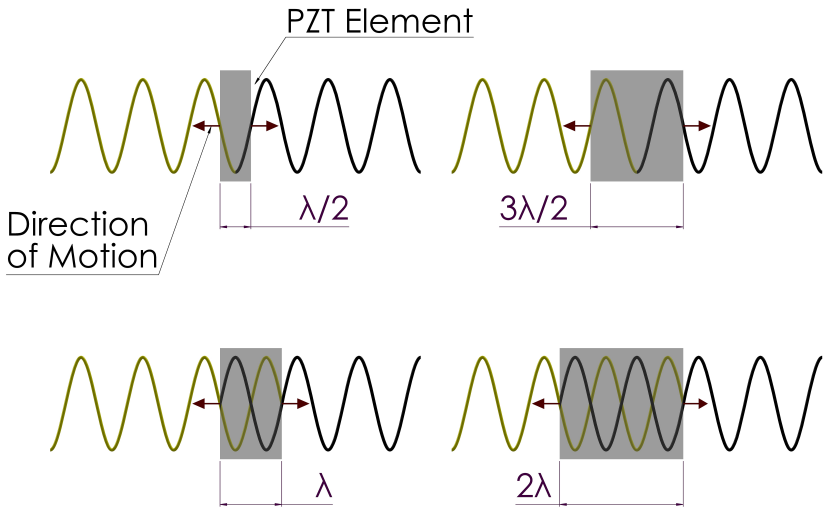

Figure 3.2: The thickness resonances of a piezoelectric crystal demonstrated as a superposition of waves. The two edges of the PZT oscillate symmetrically about the centre of the element, with the yellow wave travelling to the left and the black wave travelling to the right. When the thickness of the PZT is equal to an odd multiple of half wavelengths the waves constructively interfere within the element, giving rise to an enhancement in the efficiency of the transducer.

waves from each of the surfaces will constructively interfere, leading to a resonance. As the width is further increased, the phase difference between the waves from each of the faces increases, until when the thickness of the block reaches λ the waves will destructively interfere [61,62]. The cycle of constructive and destructive interference will continue with increasing thickness, with additional higher frequency harmonics when the thickness of the block is equal to an odd multiple of half wavelengths:

$$f_n = \frac{(2n-1)c}{L} \tag{3.3}$$

where $n = 1, 2, 3....$ and c is the sound speed in the piezoelectric material.

One problem when using piezoelectric materials to generate ultrasound is that there is often a mismatch between the acoustic impedance of the piezoelectric

material and the target material. This mismatch is particularly large in fluid coupled applications, leading to large amounts of energy being reflected from the interface between the two materials. Liquids typically have acoustic impedances on the order of 1-2 MRayls, for example water has an acoustic impedance of 1.5 MRayls, compared to PZT which is typically around 35 MRayls. Effective coupling into gases is much more difficult as gases tend to have significantly lower acoustic impedances, for air 0.43 kRayls, giving a mismatch of approximately 5 orders of magnitude. Often this effect is minimised by the addition of a matching layer with an intermediate impedance to the front of the piezoelectric material, this will discussed in more detail in Chapter 7. In applications where the piezoelectric material is radiating into a solid, there is an added issue of coupling. In almost all such applications some type of couplant material, usually a liquid or gel, is required to allow the ultrasound to be transmitted effectively into the test medium, as even a thin layer of air can significantly reduce the effectiveness of the transducer. This can also lead to inconsistencies in measurements if there is variation between the coupling of the piezoelectric element.

3.2 Electromagnetic Transduction

Electromagnetic acoustic transducers (EMATs) provide a non-contact technique for generating ultrasound in an electrically conductive solid. Though EMATs may not be ideally suited to flow applications as they are unable to generate ultrasound in a fluid directly, they have been used several times in this work to both generate and detect ultrasonic waves in the metallic waveguide strips, in Chapters 5 and 7. As such it is beneficial to explain the principles of EMAT operation here.

An EMAT generally consists of two components, a coil and a permanent magnet, as shown in figure 3.3. In order to generate ultrasound in the sample a large current, varying at an ultrasonic frequency is passed through the coil of the

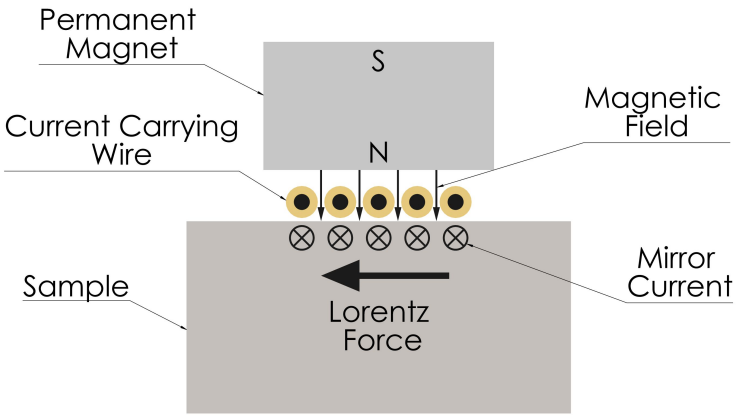

Figure 3.3: A schematic diagram of the structure of a EMAT.

EMAT. This time varying current generates a a magnetic field which penetrates into the electromagnetic skindepth of the conducting material [63], which will in turn generate a current at the surface of the sample, which, externally to the sample, appears to mirror the current applied to the coil (an eddy current). These induced currents then interact with both the induced magnetic field and the field from the permanent magnet, generating a force on the electrons in the conductor via the Lorentz mechanism. The momentum from the electrons is then transferred to the nuclei, creating a stress in the material, allowing the generation of ultrasonic waves. Due to the large difference between the mass of an electron and the mass of the nuclei large currents are required to give the electrons sufficient momentum to generate ultrasonic waves in the material, making EMAT generation quite inefficient. The type of ultrasonic waves generated and their propagation direction is determined both by the design of the coil and the alignment of the permanent magnet [63]. There are other mechanisms which can contribute to the generation of ultrasonic waves with an EMAT [63], but in the stainless steel waveguides used in this work, it will primarily be the Lorentz mechanism that is responsible for the generation.

Detection of ultrasonic waves using EMATs also occurs via the Lorentz force mechanism. The incident wave causes the material in the sample to oscillate, both the nuclei and electrons. The presence of the large static magnetic field causes the motion of these particles to generate a Lorentz force which acts upon them, causing them to accelerate. This acceleration gives rise to an electric field, which in turn induces a current in the coil of an EMAT placed close to the surface. As the electrons have a much smaller mass than the nuclei the Lorentz force will cause them to experience a much greater acceleration, making the electrons primarily responsible for EMAT detection of ultrasonic waves. Much like when generating ultrasonic waves with an EMAT, the alignment of the coil relative to the magnetic field changes the direction in which the EMAT is sensitive to the motion of the electrons, allowing both the in-plane and out-of-plane velocities of the electrons to be probed separately. EMAT detection of ultrasonic waves is often more efficient than generation, as both the electrons and nuclei are set in motion by the incident wave, removing the need for momentum transfer between the two by way of collisions.

As EMATs use electromagnetic waves to transmit and detect ultrasound there is no need for any additional couplant material and EMATs can even function effectively with a small lift-off between the transducer coil and the sample surface [64–66]. However, EMATs are much less efficient than piezoelectric based transducers, requiring large currents to generate ultrasonic waves, which can prevent the use of EMATs in some applications, both due to the high power requirements and the potential dangers related to high currents.

3.3 Electrostatic Transducers

Capacitive micromachined ultrasonic transducers (CMUTs) are microelectromechanical system (MEMS) based devices designed to generate ultrasonic waves in fluids such as air, water and blood [67–70]. A basic CMUT cell consists of a mem-

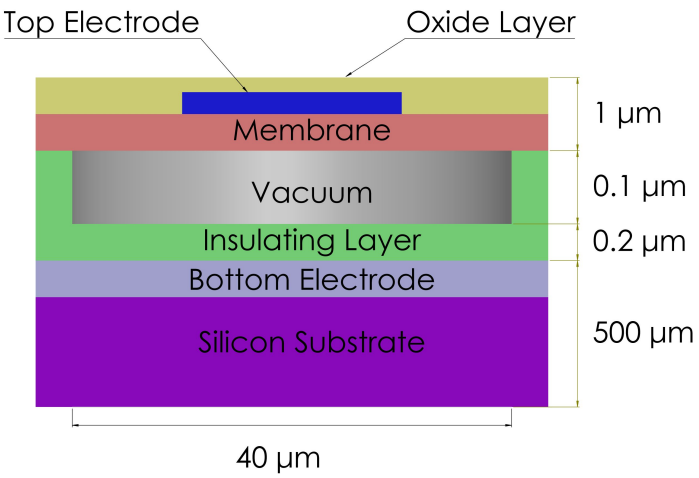

Figure 3.4: A schematic diagram of the structure of a CMUT.

brane with a thin electrode suspended over a doped silicon substrate, which acts as the second electrode, with a small vacuum filled cavity between the two. A cross-section of a CMUT cell is given in figure 3.4, along with some dimensions intended to give an indication of the sizes involved in CMUT devices [68]. To generate ultrasonic waves a DC bias is applied to the electrodes, causing the membrane to be attracted towards the substrate which is resisted by stresses in the membrane. An additional AC voltage is then applied which causes the membrane to oscillate. Detection with a CMUT also requires a DC bias voltage. An incident ultrasonic wave causes the membrane to oscillate, which produces a current as the capacitance of the CMUT varies while subjected to a fixed DC voltage across the electrodes.

Due to the small nature of the individual cell, a typical CMUT transducer device will consist of an array of cells, allowing a larger amount of energy to be transmitted, with 2D arrays as large as 128 x 128 being produced [71]. Unlike piezoelectric transducers, the acoustic impedance of a CMUT transducer is well matched to that of air, avoiding losses due to internal reflections [51]. Additionally, CMUTs are able to operate well at elevated temperatures, and are relatively

simple to consistently produce in large quantities as they use the same fabrication techniques used in standard integrated circuitry [68].

3.4 Laser Generation

Pulsed lasers can provide a non-contact method for producing ultrasonic waves, generally used in solid materials, though some work has been conducted with fluids [72, 73]. Again, though this technique is not ideal for directly generating in a fluid; it could potentially be used in conjunction with some type of waveguide, as such it is mentioned briefly here.

Generation of ultrasound using lasers may occur as a result of two effects; thermal expansion or ablation. In both cases a high power laser beam pulse is directed at the surface of a sample. Some of the incident laser energy is absorbed by the surface of the material, with the remainder either lost via reflections or scattering. For lower laser beam energy densities, the incident laser light absorbed by the surface will cause localised heating, this will cause a rapid thermal expansion. This will create thermoelastic stresses. These stresses will lead to the generation of elastic waves in the bulk of the material, with the frequency content dependent on the duration of the laser pulse and the properties of both the target material and the laser.

Ablative laser generation functions in a similar manner, using a pulsed laser beam, however in this case the power of the laser is generally higher. This higher power laser causes the area struck by the laser beam to ablate, causing surface damage to the target material typically extending to a depth of several microns. The resulting stresses then lead to the generation of ultrasonic waves [73].

In addition to the ultrasonic generation being a non-contact method of generating ultrasound, bringing with it many of the benefits previously described for EMATs, the small size of the laser beam allows the ultrasonic waves to be generated

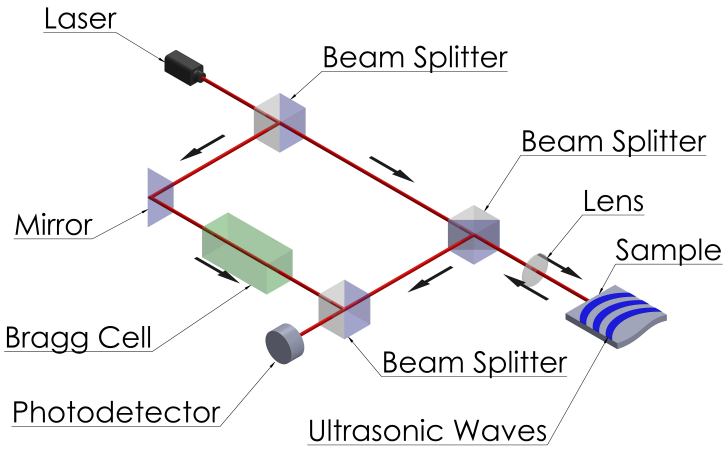

Figure 3.5: A schematic diagram of a simple laser vibrometer.

in very precise locations and on a range of surface geometries. However, the power requirements for such laser systems are high, as is the cost of the laser equipment required to generate the ultrasound. Additionally, lasers bring with them a large number of safety concerns, which can render these techniques difficult to use in an industrial setting.

3.5 Laser Detection

Though laser generation is not used in this work, laser detection of ultrasound is used throughout, in the from of laser vibrometry. Laser vibrometry has many advantages, including non-contact detection, preventing any mass loading which could influence the measurement, a wide bandwidth and precise measurement locations. Also, for detection only applications, the lasers used can be of much lower power, making them smaller, cheaper and inherently safer.

A laser vibrometer detects ultrasonic waves through an application of the Doppler effect. A single laser source which provides the beam used for the measure-

ments, this beam passes through a beam splitter, forming two separate coherent beams; a measurement beam and a reference beam. The measurement beam continues on through a lens which focuses the beam onto the surface of the sample in which the ultrasonic waves are to be measured. The laser is then reflected by the sample surface, the motion of which causes a shift in the frequency of the laser light Δf_D, given by:

$$\Delta f_D = \frac{2v}{\lambda}, \tag{3.4}$$

where v is the velocity of the target, and λ is the wavelength of the laser.

The Doppler shifted light then passes back into the vibrometer, where it is reflected towards a photodetector. Before reaching the detector the reference beam and the measurement beam are combined at a beam splitter. At the detector, either the velocity of the target material or the relative displacement may be measured.

As an ultrasonic wave passes through the point monitored by the laser vibrometer the length of the measurement beam path varies. This variation in the path length causes a modulation in the intensity of the combined beam given by [73]:

$$I_T = I_M + I_R + 2\sqrt{I_M I_R}\cos\left(\frac{2\pi(L_M - L_R)}{\lambda}\right). \tag{3.5}$$

Here I_T is the intensity of the summed beam; I_M and I_R are the intensities of the reference and measurement beams respectively; and L_M and L_R are the respective path lengths for the measurement and reference beams. The velocity and displacement measurements may then be monitoring the modulation of the intensity in time.

Equation 3.5 highlights one issue with this technique, the term which causes the modulation is symmetric about zero. This means that the direction of the displacement cannot be determined, only the magnitude. To allow the direction of the displacement to also be obtained an additional frequency shift is applied to the reference beam, using a Bragg cell, of the order of 40 MHz [73] which allows the

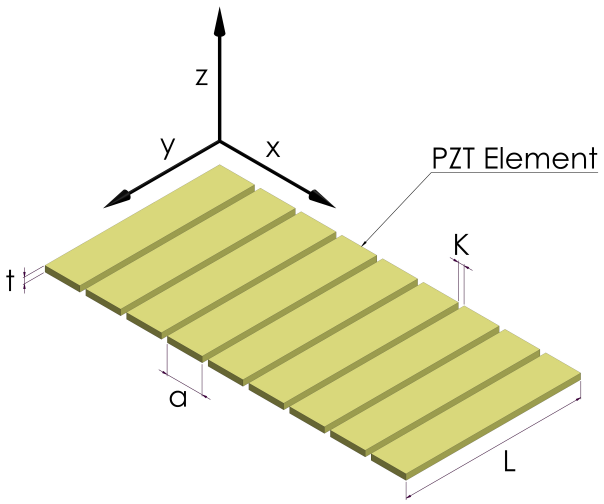

Figure 3.6: The element layout of a one dimensional/linear array. The array consists of several individual PZT elements, of length L, width a and thickness t, separated by a kerf of K.

direction of the vibration to be distinguished.

3.6 Ultrasonic Phased Arrays

A phased array transducer is a more advanced method of generating ultrasound, which allows a much greater control over the emitted wavefront. An array transducer is made up of multiple individual transducer elements, each of which may be fired separately. This allows variable delays to be added to the ultrasonic waves transmitted from each of the elements, allowing the possibilities of electronic steering and focusing which have facilitated a huge range of new applications of ultrasonic techniques in fields such as NDT and medical imaging [52, 74–77]. Ultrasonic arrays may have a range of designs, including one dimensional linear arrays, two dimensional arrays and annular arrays. Primarily one dimensional arrays will be discussed here, as this is the simplest and most common design.

A one dimensional array is typically composed of a series of linearly dis-

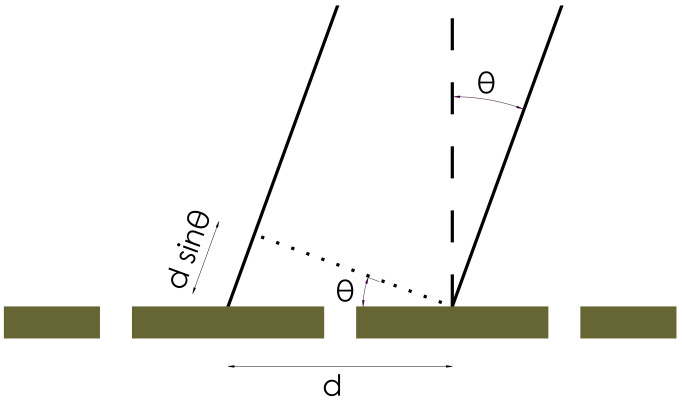

Figure 3.7: A schematic diagram demonstrating steering on a 1D linear array.

tributed rectangular elements, with an inter-element spacing (also known as kerf) of K, as shown in figure 3.6. The length of each individual element, L is generally much larger than the width a, allowing the length of the elements to be considered as effectively infinite such that the emission from the array may be considered on a two dimensional plane.

To steer the output from the array, appropriate delays, or focal laws, are calculated for each of the individual elements such that the waves from each element constructively interfere along the desired steering angle or focal point. For steering to an angle θ, the delay required for each element, Δt_n, is given by [76]:

$$\Delta t_n = \frac{nd}{c} \sin\theta + t_0. \tag{3.6}$$

Here, $n = 0, \pm 1, \pm 2, ...$, which refers to the position of each element in the array, relative to the central element; d is the array pitch, the separation between the centres of adjacent elements; c is the sound velocity in the target medium; and t_0 is an additional arbitrary delay, which may be added to prevent negative delays, which

are unphysical. To focus a linear array at a specific point, the individual element delays may be calculated using [78]:

$$\Delta t_n = \frac{r_n - r_0}{c} + t_0, \tag{3.7}$$

where r_n is the distance between the element n and the focal point and r_0 is the distance between the central element and the focal point. Though equations 3.6 and 3.7 describe the delays required for a one dimensional array, they may be modified to accommodate steering and focusing in additional dimensions, for example in the case of a two dimensional array [79].

To allow the output from the array to be steered or focused ideally, the array would be required to have an infinite number of elements, each of which acts as a point source, which is clearly is not practical. As such the finite number of elements and finite size of each of the elements will affect the field emitted by the array and limit the ability to manipulate the field through the use of delays. A more realistic model considers each element as a line source than as a point source. This causes each element to emit waves with a preferred direction, known as the directivity of the element. This is calculated by integrating the fields of a line of point sources, radiating uniformly in two dimensions [80, 81]:

$$\begin{aligned} D(\omega,\theta) &= \frac{1}{a}\int_{-\infty}^{\infty} \text{Rect}\left(\frac{x}{a}\right) e^{-ikx} dx \\ &= \frac{1}{a}\int_{-\frac{a}{2}}^{\frac{a}{2}} e^{-ikx} dx \\ &= \text{sinc}\left(\frac{ka}{2}\right) = \text{sinc}\left(\frac{\pi a \sin\theta}{\lambda(\omega)}\right). \end{aligned} \tag{3.8}$$

For arrays coupled to surfaces, there will be a additional complexity, as each wave mode, shear and longitudinal, will have a separate directivity [75]. However, equation 3.8 is a suitable approximation for fluid coupled applications, such as those

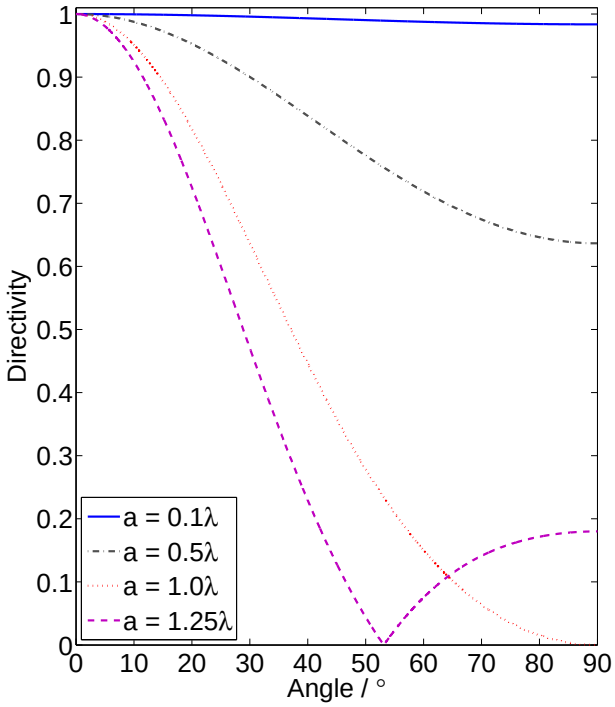

Figure 3.8: The directivity of a transducer element as the size of the element, a, is varied relative to the wavelength.

discussed in this work. From this equation it is clear that the width of the element, a relative to the wavelength, λ, will significantly affect the directivity of the element [82]. When a is is small relative to λ the element will radiate almost uniformly in all directions. As a is increased, the emitted energy will become focused around $\theta = 0$, as shown in figure 3.8. Additionally, when a is larger than λ the term inside the sinc function can take values larger than π, which causes side lobes to occur at high angles. An example of these side lobes can be seen in figure 3.8 for the case of $a = 1.25\lambda$. Such side lobes not only divert energy away from the desired direction, but can also give rise unwanted signals. As such, when designing arrays it is desirable to have elements with a width less than one wavelength to suppress these effects.

Another aspect of an array design which can have a significant influence on

the emission from the array is the element spacing, d. Due to the periodic nature of a typical array, constructive interference may occur between the waves emitted from adjacent elements. This causes the array to behave like a diffraction grating, with grating lobes emitted at an angle of θ_G [83]:

$$\sin\theta_G = \frac{n\lambda}{2d}. \tag{3.9}$$

From this equation it is clear that in order to suppress these grating lobes the array should be designed such that the element spacing is less than $\lambda/2$. In many applications ultrasonic arrays are driven with short pulses, rather than continuous wave signals, which lessens the effect of grating lobes, allowing the $\lambda/2$ condition to be relaxed [84].

3.6.1 Waveguide Buffers

Waveguides have been in use as a thermal buffers since the 1930s, to overcome the difficulties associated with using piezoelectric materials at elevated temperatures [8]. In some of the earliest applications of such waveguides metallic cylinders were used to measure the specific heat of gaseous carbon dioxide at temperatures of up to 1000 °C. Since this early work, ultrasonic waveguides with a wide array of geometries have been used in a range of applications.

The most common geometry used for ultrasonic buffers is that of a rod [1–5]. Such waveguides have been used to study extreme temperature materials, at both high and low temperatures. In the earliest work, simple cylindrical rods were used, but rapidly, work began on improving this simple design. One area that has received much attention is the reduction of reflections and mode conversion that may occur at the radial boundary of such cylindrical waveguides. A range of techniques have been investigated to allow the reduction in these effects, including knurling of the surface [85], or by the inclusion of some type of threading along the length of

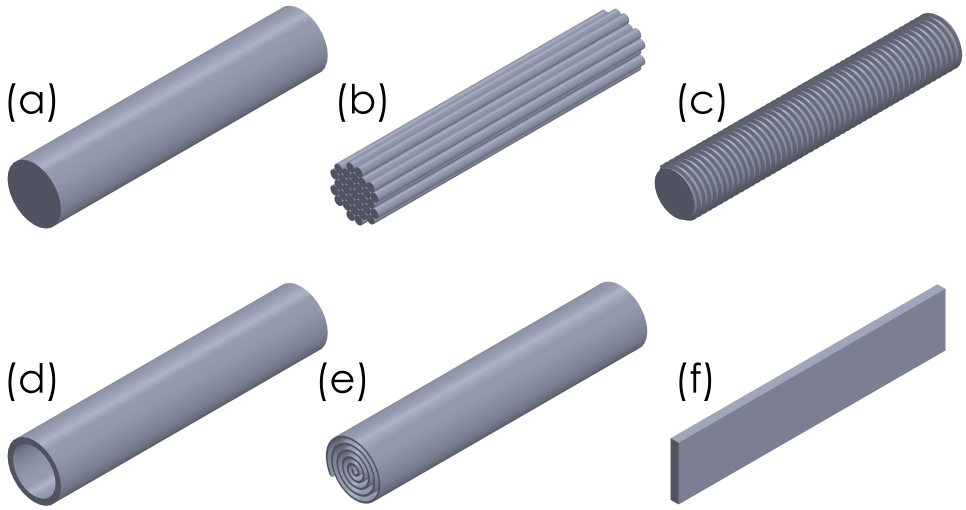

Figure 3.9: A selection of waveguide geometries which have been used to isolate piezoelectric materials from hostile environments: (a) a simple rod [1–5], (b) a bundle of narrow rods [6, 7], (c) a threaded rod [4], (d) a hollow cylinder [8], (e) a spiralled plate [9] and (f) a thin strip [6, 10, 11].

waveguide [4]. Though these techniques have been shown to be effective, they have the drawback of introducing additional noise into the signal. More recent techniques attempt to retain some of these benefits, while avoiding the increased noise involve the addition of a layer of cladding around the central waveguide core [86–88].

Another development in the use of rods as waveguides was the discovery of the relationship between the wavelength of an ultrasonic wave and the rod radius on the propagation of the wave. By selecting a rod with a specific wavelength to radius ratio, both the velocity of the wave in the waveguide and the amount of dispersion may be effectively tuned [3]. By using rods with small radii, of the order 1 mm for frequencies in the 100 kHz range, ultrasonic waves may propagate across large distances, with minimal dispersion [1, 89]. This low dispersion behaviour is essential in retaining the shape of the pulse, which is beneficial in many applications. The limitation of such a waveguide is the restriction placed upon the cross-section of the rod, which can limit the total energy transfer through the waveguide. To overcome

this, waveguide transducers were developed which incorporated many of these thin waveguides into a bundle [6,7]. Such a design has been shown to remain substantially dispersion free, despite the contact between the individual rods.

In comparison to rod based waveguide buffers, much less work has been conducted using thin plate based waveguides, due to a range of practical limitations. In a similar manner to the rod waveguides, propagation with low dispersion requires that the thickness of the waveguide plate be small, compared the wavelength of the ultrasonic waves, exciting guided Lamb waves. However, to excite these modes it is also required that the other dimensions of the plate are much larger than the wavelength, reducing any interactions with these boundaries. Designing such a waveguide is feasible for high frequency applications, > 2 MHz, where the wavelengths are small, allowing rectangular cross-section waveguides to be used in fields such as NDT [90] with little dispersion. For lower frequency applications, such as fluid-coupled ultrasonics, where frequencies below 1 MHz are commonly used, the wavelengths are significantly larger, on the order of 10 mm for common waveguide materials. This makes designing a practical device difficult, as the width dimension will generally be comparable to the wavelength, leading to some dispersive behaviour. There have been some attempts to overcome this limitation, for example by coiling the plate inside a cylindrical housing, allowing the exploitation of the plate like characteristics while allowing a large energy transfer in a small area [9]. Other plate based designs, instead utilise shear waves inside the waveguide in an effort to avoid dispersive behaviour. These designs have been shown to be usable in air coupled flow metering applications [6, 10, 11].

3.7 Conclusions

In this chapter some of the most common techniques used in the generation and detection of ultrasonic waves have been introduced and briefly discussed, including

both the method by which each technique generates ultrasonic waves as well as the advantages and disadvantages of each technique. Several of these methods, will be used throughout the experimental sections this work, in Chapters 5, 6, 7 and 8. Additionally, the theory introduced in this chapter to describe an array transducer will be used later in Chapter 8, to inform the design of a waveguide array transducer. In the following chapter the way in which ultrasonic waves propagate once they have been created in a medium will be discussed.

Chapter 4

Ultrasonic Wave Propagation

In the previous chapter a range of methods of generating and detecting ultrasound were introduced. This chapter will be concerned with how ultrasonic waves propagate once they have left the transducer and entered another material. When considering propagating ultrasonic waves there are two fundamentally separate categories of waves which should be considered, bulk waves and guided waves [51, 91, 92]. The majority of this work will be concerned with guided waves, but to be able to understand guided waves, it is useful to start with an introduction to the general case of bulk waves. In this chapter bulk waves in both solids and fluids will be discussed, followed by an introduction to Lamb waves, a group of guided waves that can propagate in thin plates.

4.1 Ultrasonic Waves in Bulk Media

A bulk wave is a wave which travels in the bulk of a material, i.e. far enough from any boundaries for them to have negligible effect on the wave propagation characteristics. The bulk waves described here are not used explicitly in this work. A basic understanding of wave propagation in bulk solids can provide a useful base for understanding more complex situations discussed later.

4.1.1 Bulk Waves in Elastic Solids

An ultrasonic wave propagating in a solid may be considered as a deformation resulting from the application of a force. At a particular point in time, this deformations may be described by the strain, ϵ, and stress, σ, tensors respectively, which in Cartesian coordinates may be written as [51]:

$$\epsilon = \begin{bmatrix} \epsilon_{11} & \epsilon_{12} & \epsilon_{13} \\ \epsilon_{21} & \epsilon_{22} & \epsilon_{23} \\ \epsilon_{31} & \epsilon_{32} & \epsilon_{33} \end{bmatrix}, \tag{4.1}$$

$$\sigma = \begin{bmatrix} \sigma_{11} & \sigma_{12} & \sigma_{13} \\ \sigma_{21} & \sigma_{22} & \sigma_{23} \\ \sigma_{31} & \sigma_{32} & \sigma_{33} \end{bmatrix}. \tag{4.2}$$

The components of strain tensor, equation 4.1, correspond to an extension in the direction of the first index, per unit length in the direction denoted by the second index. For the stress tensor, the first index corresponds to direction of an applied force and the second corresponds to the direction perpendicular to plane to which the force is applied. In the elastic regime, which is considered to be the case for solids considered in this work, these two quantities are proportional, through Hooke's Law [91].

Hooke's law may be obtained by expanding the stress tensor as a Taylor series in terms of the strain tensor:

$$\sigma_{ij} = \sigma_{ij}(0) + \left(\frac{\partial \sigma_{ij}}{\partial \epsilon_{kl}}\right)_{\epsilon_{kl}=0} \epsilon_{kl} + \left(\frac{\partial^2 \sigma_{kl}}{\partial \epsilon_{ij} \partial \epsilon_{mn}}\right)_{\epsilon_{ij}=0, \epsilon_{mn}=0} \epsilon_{ij}\epsilon_{mn} + \ldots \tag{4.3}$$

When evaluated at $\epsilon_{ij} = 0$, the first term $\sigma_{ij}(0) \equiv 0$, due to the nature of elastic solids, if the strain is reduced to zero, the stress also becomes zero. The higher order terms give rise to non-linear effects and will be neglected here. This allows

equation 4.3 to be represented as:

$$\sigma_{ij} = c_{ijkl}\epsilon_{kl}, \tag{4.4}$$

where

$$c_{ijkl} = \left(\frac{\partial \sigma_{ij}}{\partial \epsilon_{kl}}\right)_{\epsilon_{kl}=0}. \tag{4.5}$$

This is often known as the stiffness tensor and is a three dimensional representation of Hooke's law, relating stress and strain. The general form of this can be represented as:

$$c_{IJ} = \begin{bmatrix} c_{11} & c_{12} & c_{13} & c_{14} & c_{15} & c_{16} \\ c_{21} & c_{22} & c_{23} & c_{24} & c_{25} & c_{26} \\ c_{31} & c_{32} & c_{33} & c_{34} & c_{35} & c_{36} \\ c_{41} & c_{42} & c_{43} & c_{44} & c_{45} & c_{46} \\ c_{51} & c_{52} & c_{53} & c_{54} & c_{55} & c_{56} \\ c_{61} & c_{62} & c_{63} & c_{64} & c_{65} & c_{66} \end{bmatrix}. \tag{4.6}$$

However, (by applying the symmetry relations for ϵ and σ) c_{IJ} for an isotropic material may be represented as:

$$c_{IJ} = \begin{bmatrix} \lambda+2\mu & \lambda & \lambda & 0 & 0 & 0 \\ \lambda & \lambda+2\mu & \lambda & 0 & 0 & 0 \\ \lambda & \lambda & \lambda+2\mu & 0 & 0 & 0 \\ 0 & 0 & 0 & \mu & 0 & 0 \\ 0 & 0 & 0 & 0 & \mu & 0 \\ 0 & 0 & 0 & & 0 & \mu \end{bmatrix}, \tag{4.7}$$

where λ and μ are the Lamé parameters [51]. In this form, a reduced notation is used, with only two indices, I and J, rather than four. The indices i, j, k and l can be considered as two pairs, ij and kl. Each pair may only take one of six sets values due to symmetry, given in table 4.1, allowing each pair to be represented by

Table 4.1: The conversion between the four index notation to the reduced, two index, notation.

I, J	ij, kl
1	11
2	22
3	33
4	$23 = 32$
5	$31 = 13$
6	$12 = 21$

a single index, simplifying the notation [51].

Hooke's law, equation 4.4, can then be combined with Newton's second law,

$$\frac{\partial \sigma_{ij}}{\partial x_j} = \rho_0 \frac{\partial^2 u_i}{\partial t^2}, \tag{4.8}$$

where x_j indicates direction, ρ_0 is the density and u_i is an extension in the i direction, to obtain the wave equation. For the isotropic material previously discussed, this takes the form:

$$\rho \frac{\partial^2 u_i}{\partial t^2} = \frac{\partial}{\partial x_i}\left[(c_{11} - c_{44})\frac{\partial u_i}{\partial x_i}\right] + c_{44}\frac{\partial^2 u_i}{\partial x_j^2} + c_{44}\frac{\partial}{\partial x_i}\left(\frac{\partial u_i}{\partial x_j}\right). \tag{4.9}$$

This equation can be separated into two parts, one which describes longitudinal waves, and a second which describes transverse waves:

$$\frac{\partial^2 u_L}{\partial t^2} = c_L^2 \nabla^2 u_L, \tag{4.10}$$

$$\frac{\partial^2 u_T}{\partial t^2} = c_T^2 \nabla^2 u_T, \tag{4.11}$$

where the longitudinal and transverse velocities are given by:

$$c_L = \sqrt{\frac{c_{11}}{\rho}}, \tag{4.12}$$

$$c_T = \sqrt{\frac{c_{44}}{\rho}}. \tag{4.13}$$

4.1.2 Bulk Waves in Fluids

When considering wave propagation in fluids, a slightly different approach to deriving the wave equations is needed, as Hooke's Laws is no longer valid. For fluids we base our approach on pressure, P, as this is a quantity which is commonly measured experimentally. It is simplest to begin by considering only a single dimension which may later be extrapolated into the full three-dimensional case. A one dimensional force, applied to a singular volume element, between x and $x + dx$, will give rise to a pressure increase in that region:

$$dF_x = \left[P(x) - \left(P(x) + \frac{\partial P}{\partial x}dx\right)\right] A = -\frac{\partial P}{\partial x}dxA. \tag{4.14}$$

Here dF_x is the change in the force in the x direction and A is the cross-sectional area of the volume element. The mass of this volume element is give by $\rho_0 dxA$, which allows equation 4.14 to be combined with Newton's law, to give:

$$\frac{\partial P}{\partial x} = -\rho_0 \frac{\partial^2 u}{\partial t^2}. \tag{4.15}$$

A new term, compressibility, χ, can be defined to link the pressure change to a volume change:

$$\chi = -\frac{1}{V}\left(\frac{\partial V}{\partial P}\right). \tag{4.16}$$

This term can then be substituted into equation 4.15 to give an alternate form of the wave equation:

$$\frac{\partial^2 u}{\partial t^2} = V_0^2 \frac{\partial^2 u}{\partial x^2}, \tag{4.17}$$

where

$$V_0^2 = \frac{1}{\rho_0 \chi} = \frac{\partial P}{\partial \rho}, \tag{4.18}$$

which is the sound velocity in the fluid.

4.2 Ultrasonic Guided Waves

Unlike bulk waves, a guided wave has its energy and motion restricted by a set of boundaries. This results in the creation of an infinite number of individual propagation modes which may be calculated by solving the wave equation with specific sets of boundary conditions. For many applications, such as in the field of NDT, the beneficial properties of particular guided wave modes are exploited, in order to allow ultrasonic waves to travel large distances with minimal dispersion while losing minimal energy.

4.2.1 Dispersion of Guided Waves

Dispersion occurs when the velocity of an ultrasonic wave has a dependence on frequency. This is not usually an issue with bulk waves, but dispersion is common in many types of guided waves. Dispersion causes a propagating ultrasonic pulse to spread out in space and time, as the individual frequency components within the pulse propagate with slightly different velocities.

This effect is often detrimental to obtaining accurate measurements, as the energy of the wave-packet becomes distributed, the maximum amplitude decreases and the signal spreads out in both space and time, both of which are problems in any measurement application [93]. Dispersion can also pose challenges for flow

measurement, as cross-correlation is commonly used to determine transit times that are required to calculate flow rates [94]. Such distortion of the transmitted signal, introduced by dispersion in a waveguide, can increase the difficulty of obtaining an accurate measurement of a flow velocity.

Guided wave modes are not equally dispersive at all frequencies, and by selecting the correct frequency for a specific geometry it is possible to limit the dispersion of a guided wave. For many applications, thin rods and plates are often used as waveguides, as the modes in such geometries are well understood and they support modes with low dispersion regions [92].

This thesis is primarily concerned with waveguides consisting of thin metallic strips with a rectangular cross-section. It is expected that the modes supported by such strips should be similar to those in a semi-infinite thin plate. Therefore it is helpful to start by discussing guided waves in such thin plates, as they are well understood and straightforward.

4.2.2 Lamb Waves in Thin Plates

Lamb waves are a type of guided wave that can propagate in a thin plate, which are described by the Rayleigh-Lamb equations [91, 92, 95]. In order to derive these equations we must first state several assumptions about the material. Firstly, it is assumed that the material is isotropic and homogeneous. Next, the surfaces of the plate being considered should be traction free, meaning that there is no stress on these boundaries. Finally, the plate is assumed to be "semi-infinite". In practical terms, this means that the dimensions of the plate, other than the thickness, are much larger than the particular wavelength of interest. This allows any additional boundaries to be neglected which simplifies the calculation.

Applying these conditions, two sets of solutions may be obtained; one set which describes modes that have a displacement which is symmetric about the mid-plane of the plate, S-modes, and a second set of modes which have antisymmetric

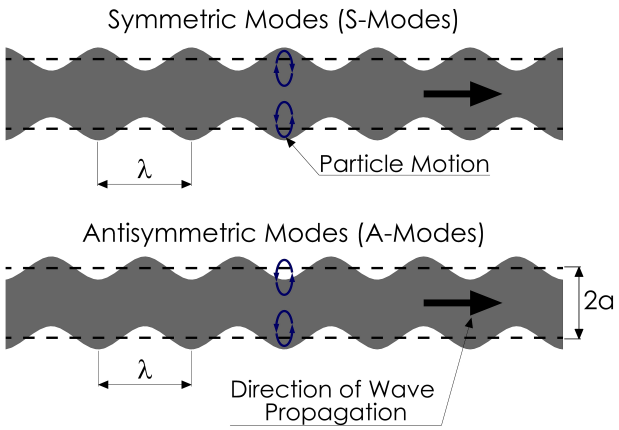

Figure 4.1: A schematic diagram of the displacement of the surfaces of a thin plate due to Lamb waves. The motion of the individual particles in the plate, along elliptical paths, is also shown to demonstrate the origin of these mode shapes.

displacements about the mid plane, the A-modes, given here respectively:

$$\frac{\tan(qa)}{q} + \frac{4k^2 p \tan(pa)}{(q^2 - k^2)^2} = 0, \tag{4.19}$$

$$q\tan(qa) + \frac{(q^2 - k^2)^2 \tan(pa)}{4k^2 p} = 0, \tag{4.20}$$

where k is the wavenumber (the spatial frequency of the wave, $k = \frac{2\pi}{\lambda}$), $2a$ is the thickness and the variables p and q are defined as:

$$p^2 = \left(\frac{\omega}{c_L}\right)^2 - k^2, \tag{4.21}$$

$$q^2 = \left(\frac{\omega}{c_T}\right)^2 - k^2. \tag{4.22}$$

Here ω is the angular frequency and c_L and c_T are the longitudinal and transverse sound velocities in the material, respectively. A complete derivation of these solutions can be found in Appendix A. A schematic diagram of the surface displacements due to these two types of Lamb modes is shown in figure 4.1.

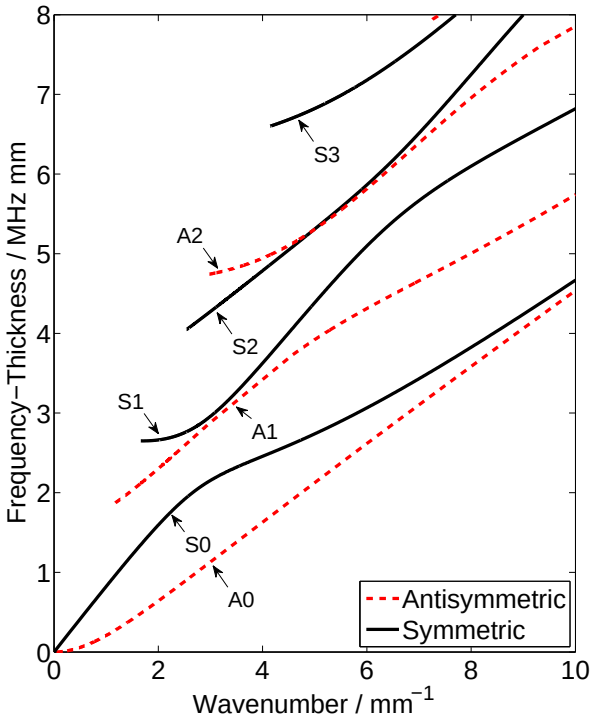

Figure 4.2: Analytically calculated Lamb modes for a 1 mm thick "semi-infinite" stainless steel plate.

From these equations, dispersion curves may be produced which show the relationship between the frequency, ω, and wavenumber, k of the various Lamb modes. An example of dispersion curves for Lamb waves in a stainless steel plate is shown in figure 4.2. For many applications which use Lamb waves, the frequency-thickness product is kept low. This has several benefits; firstly, the number of possible wave modes which can be excited is limited, which reduces the complexity of the signal. For example, in the case of the stainless steel plate, for a frequency-thickness product below approximately 1 MHz mm, only two modes may be excited: the S0 and A0 modes. An additional benefit of using Lamb modes in the low frequency-thickness region is the linearity of the S0 mode. The phase velocity c_p and the group velocity c_g of the Lamb modes can be related to the frequency and

wavenumber in the following way:

$$c_p = \frac{\omega}{k}, \tag{4.23}$$

$$c_g = \frac{\partial \omega}{\partial k}. \tag{4.24}$$

From these two equations, it is clear that in regions where the S0 dispersion curve is linear the phase and group velocities are equal, with a fixed value for all waves with a frequency within the linear region. This low dispersive behaviour is beneficial for techniques such as cross-correlation, commonly used in measurement applications, as the pulse retains its shape within this region.

4.2.3 Finite Element Modelling

There are many ways in which the propagation of guided waves may be modelled. Perhaps the most obvious method is to solve the analytically calculated dispersion relations. In many cases, such as Lamb waves, this is straight forward and can be achieved using numerical methods. However, the analytical description of the waves becomes incredibly complicated, making numerical calculations difficult. In order to avoid this complexity many alternative techniques have been developed to model the propagation of ultrasonic waves.

One common method of doing this is the use of finite element (FE) modelling [96, 97]. In FE modelling, the system to be modelled is divided into small, discrete elements, known as a mesh. This technique allows approximate solutions for more realistic geometries to be obtained. For each element, the solution to a differential wave is calculated with the application of stress and strain, an ultrasonic wave, and specific boundary conditions for that node. This process is then repeated for each element in the model, creating a series of simultaneous equation to be solved. Assuming the solutions for each of the individual elements are compatible with those of neighbouring elements, solutions for the system can be found,

allowing properties such as displacement and pressure to be found at each point in the mesh. The calculated properties are then used as the basis for the next set of calculations at the next time step, allowing the propagation of an ultrasonic wave in time to be plotted.

A disadvantage of this technique is, depending on the size of the model and the mesh, that it can be computationally demanding. An upper limit is placed on the size of the mesh by the maximum frequency of interest, f_{Max}, and the minimum wave speed in the medium, v_{Min}. In order to ensure that all of the required information may be extracted from the model, the maximum allowable dimension of an individual element, X_{Max} can be found by applying Nyquist Sampling Theorem:

$$X_{Max} > \frac{v_{Min}}{2f_{Max}} = \frac{\lambda_{Min}}{2}. \tag{4.25}$$

From this equation it can be seen that the maximum element size is half of the minimum wavelength, λ_{Min}. However, in most FE models a much finer mesh is used to prevent artefacts such as numerical dispersion [98, 99] , allowing the model to better replicate experimental results. A more common value of the maximum dimension of an individual mesh element is [100, 101]:

$$X_{Max} > \frac{\lambda_{Min}}{15}. \tag{4.26}$$

However, this is still used more as a guideline than as a rule. In when using finite element modelling it is usually advisable to check for convergence. This involves repeatedly running the model, each time with an increased number of elements and comparing the results between each run of the model, usually up to a much finer mesh than the one produced using the above rule. Once the results from two of these models are indistinguishable it can be said that the model has converged and the mesh of the model should have no effect on the results. This technique was used throughout all of the FM modelling used later in this work to optimise the models.

This requirement can lead to a very large number of individual elements, which can be very computationally expensive. For some model geometries this can be offset by reducing the model to two dimensions or using planes of symmetry to reduce the number of elements to be simulated.

4.2.4 Semi-Analytical Finite Element Modelling

An additional method of studying guided waves is to use the Semi-Analytical Finite Element (SAFE) method, which combines elements of the two techniques discussed previously [102, 103]. Generally, when applying this technique, the cross-section of the waveguide is divided into small elements and used as the basis of the model. The possible modes in the waveguide geometry can then be calculated by solving for the eigenvalues of the system [103]. Various techniques have been implemented to solve these systems. One commonly used technique uses the cross-section of the waveguide as the basis of an axisymmetric model, with a radius much greater than the dimensions of the cross-section. This large radius allows the effect of the curvature to be neglected, as on the scale of the cross-section, the waveguide is approximately straight [102, 104]. This technique is less computationally intensive than a standard FE modelling, but it relies on the waveguide having the same cross-section along its entire length. As such this technique was not suitable for some of the more complex geometries considered in this work.

4.2.5 Two-Dimensional Fast Fourier Transform Techniques

In addition to the analytical techniques discussed previously, the dispersion curves for a propagating wave may be obtained from the results of FE modelling or experimental measurements. There are several methods to do this, in this work a technique which utilises two-dimensional fast Fourier transforms (2D-FFT) was used [105]. The basis of this technique is that the surface displacement of a wave, propagating

in the x direction, may be described as:

$$u(x,t) = A(\omega)e^{i(\omega t - kx - \theta)}. \tag{4.27}$$

Here $A(\omega)$ is a frequency dependent amplitude and θ is a phase angle. Thus it can be seen that the displacement can be considered to have a spatial and temporal dependence. By applying a 2D-FFT to equation 4.27, a new amplitude is obtained which is a function of frequency and wavenumber:

$$H(k,f) = \iint_{-\infty}^{+\infty} u(x,t)e^{-i(kx-\omega t)}dxdt. \tag{4.28}$$

The peaks in this amplitude function correspond to the propagating wave modes. As such, this technique can be used to obtain dispersion curves with relative ease, even when there are multiple modes present in the signal.

This technique can be very useful for obtaining dispersion curves for waveguides with complex geometries, as the surface displacement $u(x,t)$ may be measured experimentally, or obtained from FE modelling, measured at a series of closely spaced points along a line. The spacing of these measurement points must be kept much smaller than the minimum wavelength of interest, again to prevent any aliasing. The time traces from each of the measurement positions can then be arranged into an array of amplitudes dependent on position and time, effectively $u(x,t)$, to which the 2D-FFT may be applied in order to obtain the dispersion curves.

4.3 Conclusions

This chapter has introduced some of the fundamental concepts related to wave propagation. Analytical models of wave propagation in both solid media and fluids have been presented, allowing the more complex case of guided waves to be introduced. The concept of dispersive wave propagation has also been discussed for the

case of Lamb waves in thin plates, through analytical modelling. This chapter has also provided an introduction to FE modelling, which will be used throughout this work as well as the ways in which this modelling may be used to study dispersion in waveguides with complex geometries. In the next chapter, the two-dimensional Fourier transform techniques discussed here will be implemented to study dispersion of low frequency ultrasonic waves propagating in a range of rectangular cross-section waveguides.

Chapter 5

Guided Waves In Rectangular Cross-Section Strips

As discussed in the previous chapter, guided waves with low dispersion, such as the S0 Lamb wave mode at low frequencies, would be ideal for many industrial applications. Additionally the S0 Lamb mode has the majority of its displacement in the direction of propagation which allows more efficient generation of compressional waves in the target fluid. However, the geometric requirements of the waveguide (e.g. the large width) to support Lamb or Lamb-like waves cannot easily be satisfied within practical experimental constraints. Low frequencies are required in ultrasonic flow measurement to reduce the effect of attenuation. These frequencies are generally below 1 MHz for gas and 5 MHz for liquid applications, meaning that we have relatively large wavelengths. In this work we are primarily operating around 150 kHz, which typically corresponds to a guided wave wavelength in the order of centimetres for the mode that we wish to use. As a result of this, the width of the waveguide strips considered in this work cannot be neglected and will lead to additional complexity.

Many analytical models have been suggested in order to include the additional boundary conditions. One of the first, and simplest of these models was

suggested by Morse in 1950 [106]. He suggested a modification to the Rayleigh-Lamb equations, including traction free boundary conditions on the two additional boundaries resulting from finite strip width, leading to the following equations:

$$\frac{\tan(q^*a)}{q^*} + \frac{4p^* \tan(p^*a)(s^2+k^2)}{(s^2+k^2-q^{*2})^2} = 0, \tag{5.1}$$

with

$$p^{*2} = p^2 - s^2, \tag{5.2}$$

$$q^{*2} = q^2 - s^2, \tag{5.3}$$

$$s = \left(n + \tfrac{1}{2}\right)\tfrac{\pi}{b}, \quad n = 0, 1, 2..., \tag{5.4}$$

where the strip width is $2b$. It can be seen that the form of this equation is very similar to that of the equation for symmetric Lamb waves, and if the term s is set to 0 then equation 4.19 may be recovered, as the strip width effectively becomes infinite. The range of s values given by equation 5.4, approximately satisfy the zero stress boundary conditions on all of the surfaces. The inclusion of this constant allows the existence of additional modes, which converge around the positions of the Lamb solutions. From these equations it is also clear that increasing the width of the strip, reduces the influence of the width of the strip on wave propagation, as s is inversely proportional to b. This very simple modification was found to agree well with experimental data, with better agreement for wider strips, when a/b was small [106].

Since this early work of Morse, many other analytical models have been developed [107]. These models are, generally, much more complex, predicting even higher numbers of modes to be present, including longitudinal, torsional and bending modes in both the thickness and width dimensions [108]. Due to the complexity of these analytical models the FE techniques introduced in Chapter 4 will be used to study the effects of the waveguide geometry on wave propagation.

Table 5.1: Material parameters used in finite element modelling

Material	Density (kgm^{-3})	Longitudinal Velocity (ms^{-1})	Transverse Velocity (ms^{-1})
Stainless Steel	7890	5790	3100
Air	1.24	343	0

5.1 Finite Element Modelling of Dispersion Curves

In order to investigate the effect of the width on the propagation of ultrasonic waves a series of simulations were conducted using the commercial FE software PZFlex [109]. In the first FE model a single, rectangular cross-section, stainless steel strip, with a thickness of 1 mm, a width of 10 mm and a length of 300 mm was simulated in a box of air, as shown in figure 5.1, using the material properties given in table 5.1. A narrowband excitation, consisting of a five cycle sine wave, was applied to one end of the strip. The in-plane displacement was then recorded along the length of the centre of the strip at intervals of 0.25 mm. This small spacing helps to prevent aliasing issues as the minimum wavelength in the frequency range of interest, below 1 MHz, is of the order of millimetres. These displacement measurements were then arranged in an array, as described previously, to allow the use of a 2D-FFT to obtain the dispersion curves.

The propagating modes, which appear as high energy regions after the application of the 2D-FFT technique introduced in the previous chapter, were identified using a peak finding algorithm in MATLAB, allowing a set of dispersion curves to be plotted. The centre frequency of the input signal was then increased and the FE simulation repeated in order to obtain higher frequency regions of the dispersion curves. In theory it should be possible to obtain the entire set of dispersion curves using a single simulation using a broadband signal. However, this method would also generate frequencies higher than those of interest in this work. This would in

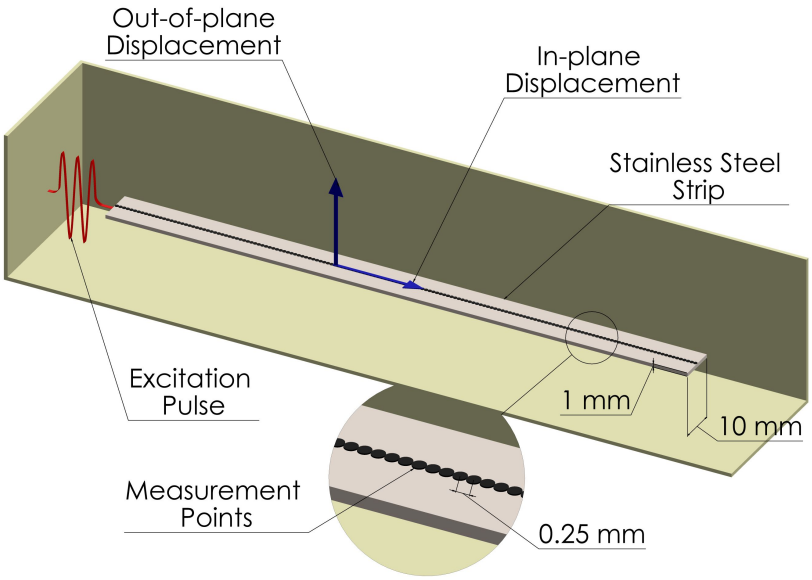

Figure 5.1: Schematic diagram of the FE model used to obtain dispersion curves. The model consisted of a single stainless steel strip driven with a narrowband excitation. The in-plane displacement was then measured at a series of points, 0.25 mm apart, along the centre of the strip.

turn require a finer mesh in the model to prevent any aliasing effects, making a large model even more computationally expensive.

The dispersion curves obtained from the simulation of the 10 mm width strip are shown in figure 5.2. Also included in this figure are the analytically calculated dispersion curve for the S0 Lamb mode in a 1 mm thick stainless steel plate, for comparison. We can see that the modes for the 10 mm width plate follow the same general shape as the S0 Lamb mode. However, as predicted by the analytical models there are additional modes resulting from the additional boundaries, which converge around the position of the S0 Lamb mode. The plurality of modes in this region, rather than the single mode, would lead to dispersive behaviour due to the loss of linearity around the gaps between the modes.

One point of note is that the modes for the 10 mm strip appear to stop abruptly as the modes deviate further from the position of the S0 lamb mode. This

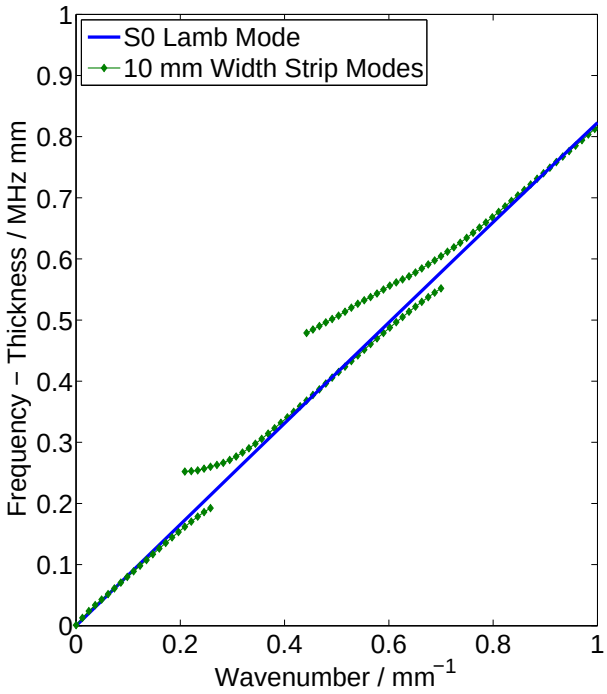

Figure 5.2: The simulated dispersion curves for a stainless steel strip waveguide with a rectangular cross-section (1 mm x 10 mm). Also shown is the S0 Lamb mode for a 1 mm thick stainless steel plate for comparison.

is due to the majority of the energy in the propagating waves being concentrated around this region, rather than being an actual physical effect. It is expected that these modes would continue on in both directions, but due to the small energy content it becomes difficult to separate the mode from the background noise using the techniques described here.

In order to further investigate the effect of the width on the wavemodes, the simulations were then repeated for stainless steel strips with the same thickness, but with a range of widths, both larger and smaller. The first of these was a strip with a width of 5 mm. From the analytical models it would be expected that the smaller aspect ratio would lead to a greater deviation from the Rayleigh-Lamb solutions. The dispersion curves from FE modelling of the 5 mm width plate are shown in figure 5.3(a). It can be seen that the reduced aspect ratio lead to a decrease in

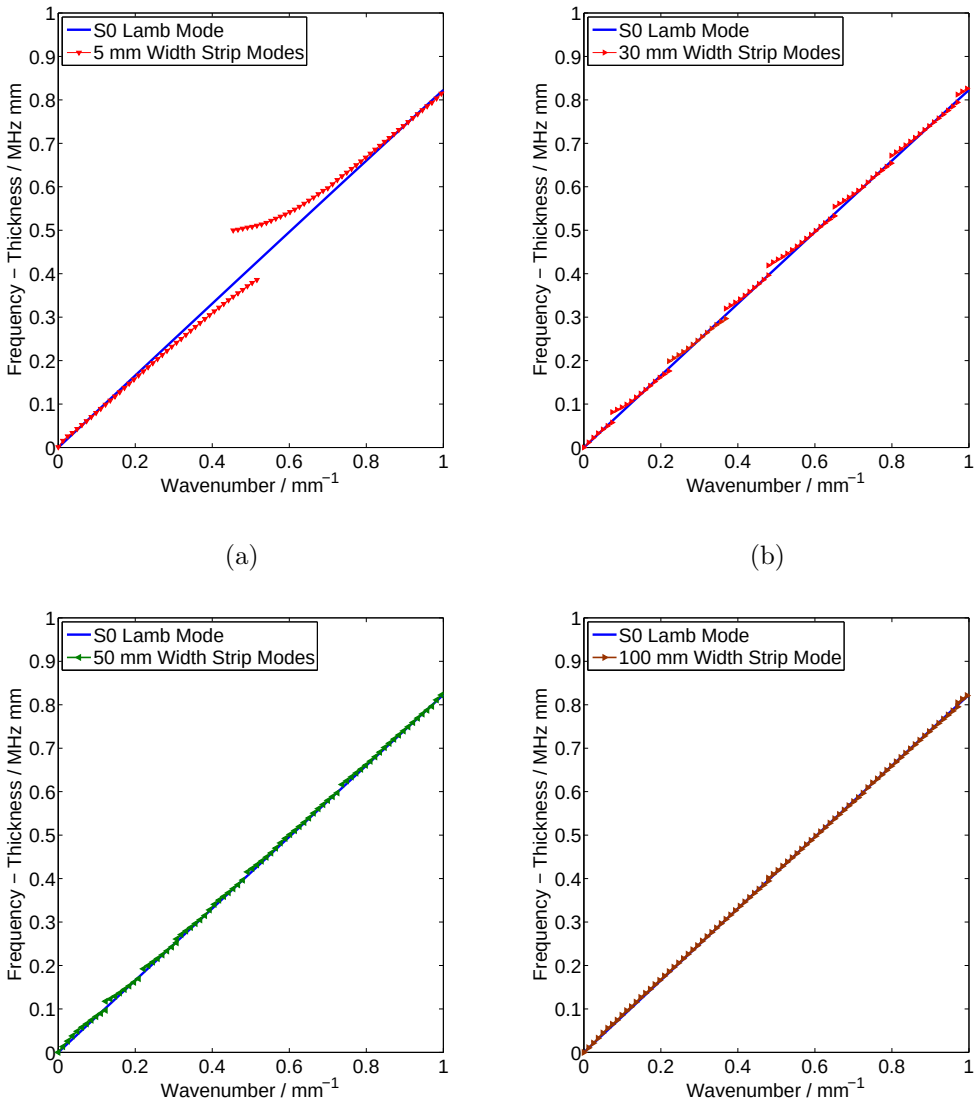

Figure 5.3: The simulated dispersion curves for 1 mm thick stainless steel strips with of widths: (a) 5 mm, (b) 30 mm, (c) 50 mm and (d) 100 mm. The S0 Lamb mode for a 1 mm thick stainless steel plate is also shown for reference.

the number of modes which could be identified in the region of interest. However, the spacing between the two visible modes is much larger than the gaps seen in the 10 mm plate case. This larger gap will cause additional dispersive behaviour, further complicating the transmitted signal and potentially reducing the viability for use as a thermal buffer in an ultrasonic flowmeter. Additionally, the smaller strip width will further reduce the size of the radiating face, lowering the energy that can be transmitted into the test fluid.

The other strip geometries investigated had larger aspect ratios, with widths of 30 mm, 50 mm and 100 mm. Again, by looking at the analytical models presented in the previous chapter, we can expect that an increased plate width, for a fixed thickness, would reduce the effect of the finite plate width and the guided waves would become more similar to Lamb waves. Looking at the dispersion curves for the strips with these larger widths, shown in figure 5.3, it can be seen that increasing the strip width increases the number of propagating wave modes in the sub 1 MHz region of interest, and the modes become more closely spaced. For the 30 mm strip, eight individual modes can be seen, and there are still noticeable gaps between them. For the 50 mm strip, some gaps can still be seen between the modes in the lower frequency region however they are much more difficult to identify as separate modes. Finally, for the 100 mm strip, the dispersion curves become essentially indistinguishable from the S0 Lamb mode.

Though increasing the width of the strip does make the dispersion behaviour much more similar to that of Lamb waves it is not a solution for many practical applications. For example, in a flow measurement application, the waveguide transducer needs to fit through a hole in a pipe, which places an upper limit of approximately 10-15 mm on the maximum width of the strip. Additionally, increasing the width of the strips may in fact negatively affect the wave propagation. With the smaller width strips, 5 mm or 10 mm, there are large gaps between the modes. However, if the transducer operates in a frequency range away from these gaps the dispersive

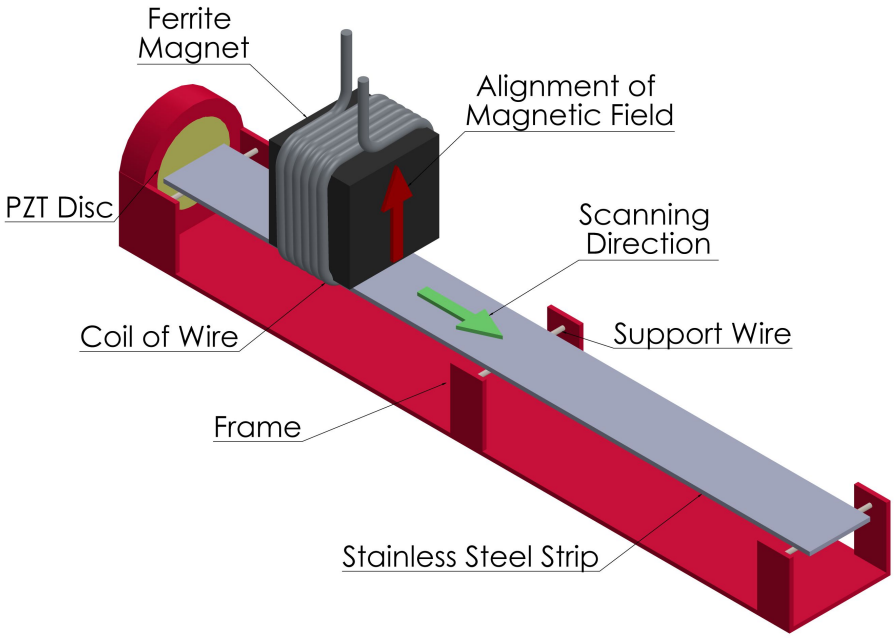

Figure 5.4: A schematic diagram of the experimental configuration used to measure the dispersion curves of a waveguide strip using an EMAT, consisting of a coil of wire and a magnet.

effects of the finite width could be minimised. With a wider strip with more modes, it becomes increasingly difficult to identify a range of operating frequencies which avoids any of these gaps.

5.2 Experimental Measurement of Dispersion Curves

In order to validate the FE modelling, the dispersion curves for a 1 mm x 10 mm x 300 mm 316 stainless steel strip were found experimentally. The strip was held in place on a frame by wires (0.1 mm diameter) at three points along its length, 20 mm from either end and in the centre. This minimised any loading of the strip to be minimised and allowed the experimental conditions to more closely replicate the FE modelling. A piezoelectric disc (PZT5A - Morgan Electro Ceramics, UK), with a

through thickness resonance of approximately 150 kHz was coupled to one end of the strip using an ultrasonic coupling gel and held in place by the frame. This PZT was then driven with a 3 cycle, 150 kHz sine wave burst, with a peak to peak voltage of 9 V. An EMAT, consisting of a 0.4 mm width linear coil (four turns of 0.1 mm diameter wire) and a permanent ferrite magnet (25 mm x 25 mm x 25 mm), was used to detect ultrasonic waves along the length of the strip at 0.1 mm intervals. An EMAT is an ideal detector for this application as it is non-contact, so can be scanned along the length of the strip easily and applies no load on the strip. An additional benefit of using an EMAT is that the direction in which the EMAT is sensitive to displacements may be selected by varying the orientation of the magnet. In this case the magnetic field was aligned in the out-of-plane direction, as shown in figure 5.4, giving enhanced sensitivity to displacements in the in-plane direction.

At each of the scanning positions along the length of the strip, the in-plane displacement was measured using the EMAT. These displacement measurements were then formed into an array of amplitudes in terms of position on the strip and time. A 2D-FFT was then applied, as with the FE modelling results to obtain information in the frequency and wavenumber domains. From this the dispersion curves could be obtained using a peak finding algorithm. Figure 5.5 shows both the experimental dispersion curves and those obtained from the FE model. It can be seen that there is a good agreement between the two sets of dispersion curves. In both cases the multiple modes resulting from the finite strip width may be observed, and the positions at which they occur align well. From figure 5.5 it can also be seen that the energy of the guided waves was not so tightly constrained to the region around the position of the S0 Lamb mode in the experimental measurements as in the FE modelling. This is clear when looking at the highest frequency of the three wave modes in the region, which extends almost across the entirety of the range of wavenumbers in the region. This is potentially due to the driving signal used in the FE model. In this model, the end of the strip was driven with an ideal, narrowband

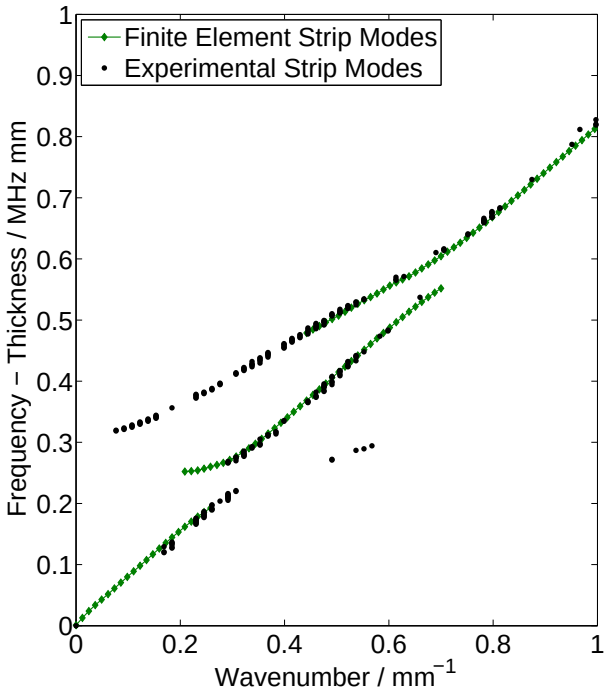

Figure 5.5: Experimentally measured dispersion curves for a 10 mm width, 1 mm thick, 300 mm long stainless steel strip compared to those obtained from a FE model of a similarly dimensioned strip. Good agreement can be seen between the experimental data and the model.

pulse, however, experimentally the piezoelectric element will influence the frequency content of the input signal and as such will affect the energy distribution in the wave modes.

5.3 Alternate Strip Geometries

FE modelling has shown that a moderate increase in strip width could have the potential to change the effectiveness of the finite width strip as a waveguide, but we are limited by the constraints of any practical application. One way that the effect of the finite width could be modified is by using a strip with a taper along the length, shown in figure 5.6. This allows the width of the strip, where it would need to enter a pipe for example, to be kept small, while allowing the strip to be wider

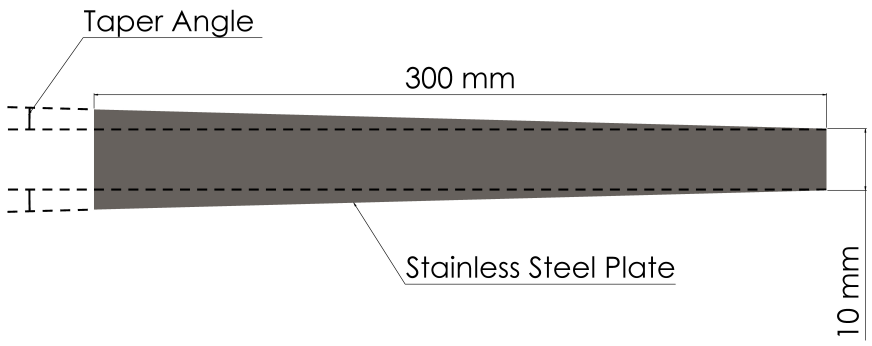

Figure 5.6: A schematic of a waveguide strip with a taper along the length. The front face of the waveguide where it contacts the fluid has a fixed width of 10 mm and the strip width is allowed to vary along the remaining length.

at the other end, where the piezoelectric element would be mounted, which could reduce any coupling across the width of the strip.

This was investigated using FE modelling. For all of the modified geometries, the length and thickness of the strips remained fixed at 300 mm and 1 mm respectively with the width at the radiating end of the strip fixed as 10 mm. Stainless steel strips with a range of taper angles, up to 0.5° were modelled. Though this may initially seem like a relatively modest range of angles, the length of the waveguide strips causes a significant increase in the strip width, with a 0.5° angle increasing the width of the strip at the non-fixed end to 15 mm.

As before, the 2D-FFT techniques were combined with the FE model in order to obtain a set of dispersion curves for the each of the tapered strips, allowing the influence of the taper on wave propagation to be demonstrated. In figure 5.7 the dispersion curves for a strip with a 0.1° taper, the smallest angle modelled, are shown in comparison to the S0 Lamb mode. As expected for such a small angle, these dispersion curves look very similar to those of the 10 mm strip with no taper, shown in figure 5.2, with gaps in the dispersion curves appearing around 200 kHz and 550 kHz.

Also shown are the dispersion curves for stainless steel strips with tapers of

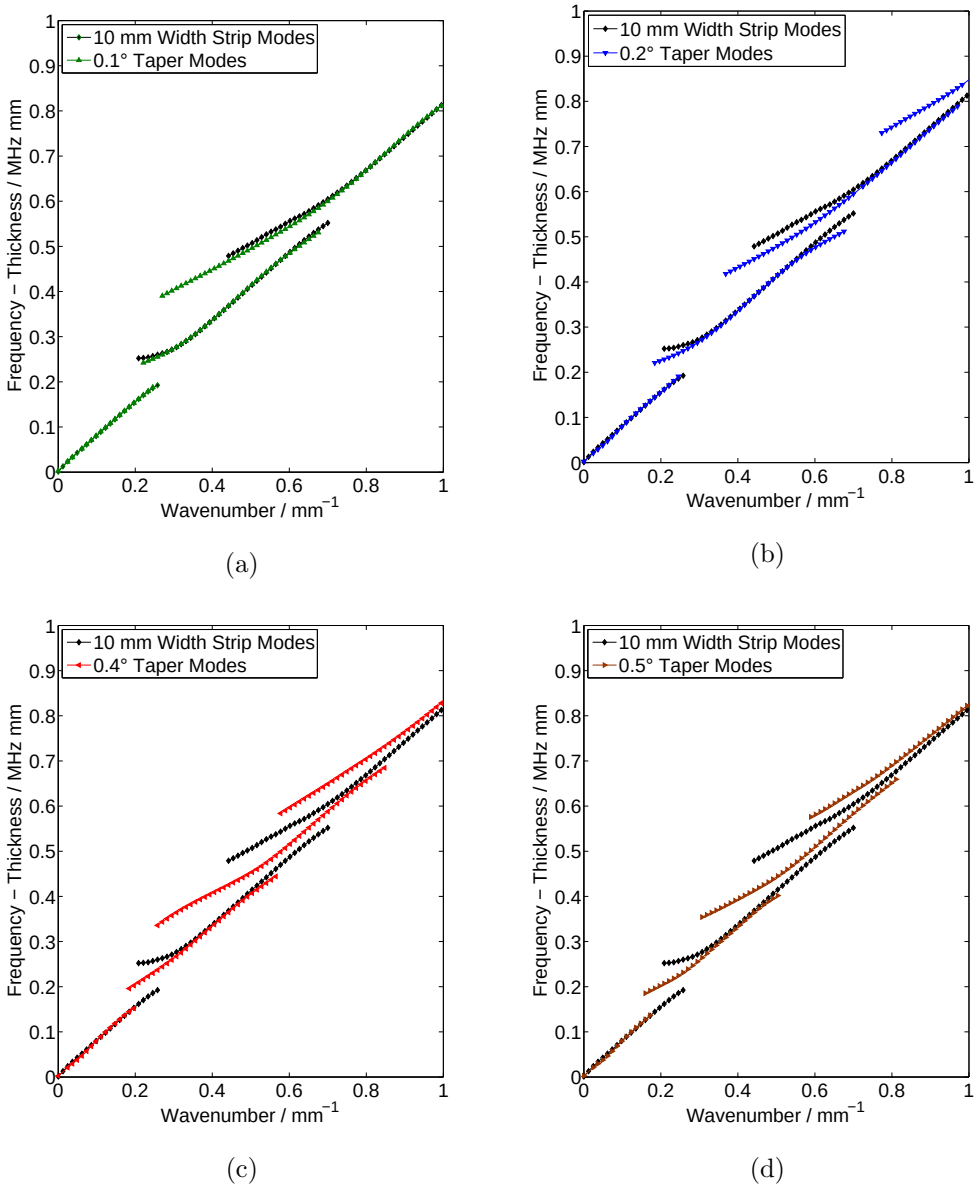

Figure 5.7: The simulated dispersion curves obtained from FE modelling of a 1 mm thick stainless steel strip with a 10 mm width radiating face and a taper in the width dimension along the length of: (a) 0.1°, (b) 0.2°, (c) 0.4° and (d) 0.5°. Also shown in each plot are the dispersion curves of a similar stainless steel strip with a fixed 10 mm width along the length (the 0° case).

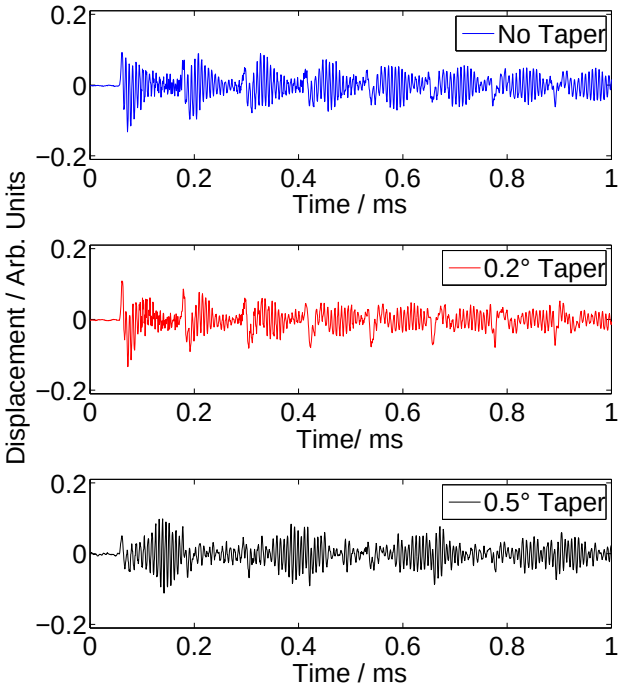

Figure 5.8: Front face displacement measured with a laser vibrometer for a 10 mm straight strip (top), a strip with a 0.2° taper along the length (middle), and a strip with a 0.5° taper (bottom).

0.2°, 0.4° and 0.5°, in figure 5.7. It is clear from these plots that the effect of the taper is to reduce the gaps between the modes, which should in turn help to reduce the dispersive behaviour of the waves propagating in the strips as the modes become increasingly more linear in this low frequency region.

In addition to the FE modelling, the effect of such tapers were investigated experimentally. Two tapered stainless steel strips were manufactured, with tapers of 0.2° and 0.5° and thickness of 1 mm, length of 300 mm and width at the radiating face of 10 mm, as in the FE model. For each of these strips a 150 kHz PZT5A disc was mounted at the wider end of the strip and driven with a 100 V square wave with a pulse width of 5 μs using an Olympus 5077PR Pulser-Receiver. The displacement of the radiating face of the strip was then measured using a Polytec

OFV-5000 laser vibrometer, with a spot diameter of approximately 150 μm. These displacement measurements are shown in figure 5.8 . It can be seen that the taper along the length of the strips has a significant effect on wave propagation in the strips. Firstly, the taper can be seen to affect the arrival times of the reverberations of the dominant guided wave mode within the strip. This is clearest in the displacement measurement from the 0.5° tapered strip, as the period of the reverberations approximately doubles, compared to the straight strip case, from 130 μs to approximately 260 μs.

It is also clear from these measurement that taper also has a significant effect on the shape of the pulse. If we compare just the initial wave packets in the two displacement measurements, disregarding the reverberations for now, we can see the two signals have very different shapes. The 0.2° strip measurement has a large, very distinct, first cycle, where as the 0.5° tapered strip has a much more symmetric signal.

Additionally, we can look at the frequency content of these signals, shown in figure 5.9. From this it can be seen that the 0.5° taper causes a reduction in the amplitude of the second frequency peak at 210 kHz, seen in the case for a straight strip, at the expense of a slight broadening of the peak centred around 150 kHz, with the full width at half maximum (FWHM) increasing from approximately 13 kHz to 16 kHz.

5.4 Conclusions

In this chapter the behaviour of guided waves in the narrow, rectangular cross-section strips has been discussed. It has been shown that when the width of the waveguide strip is of a comparable magnitude to the wavelength of the ultrasonic waves, the way in which the wave propagates in the strip differs significantly from standard Lamb waves, introducing dispersion into the wave. As the width of the

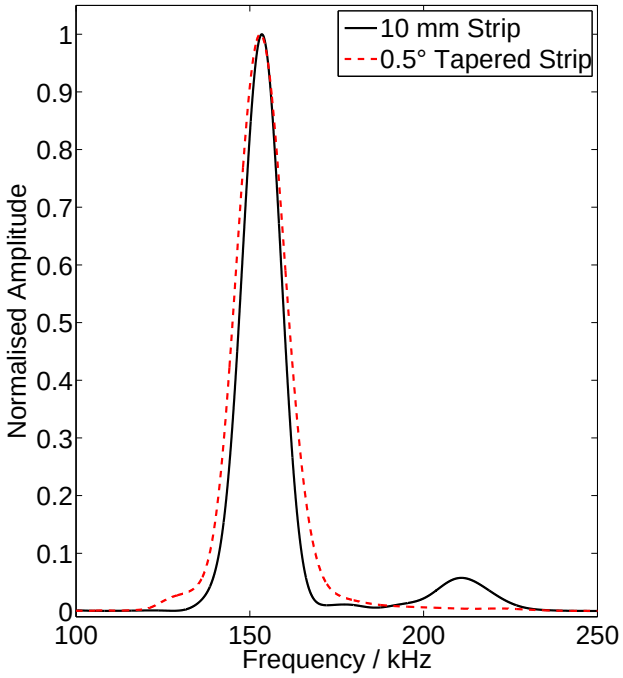

Figure 5.9: The frequency content of the front face displacement measured with a laser vibrometer for a 10 mm straight strip, solid line, and a strip with a 0.5° taper along the length, dashed.

waveguide is increased, these effects are reduced until Lamb wave behaviour is recovered. As arbitrarily increasing the width of the waveguide strips is not a practical solution for many applications, an alternative method of reducing the dispersive behaviour was investigated: the addition of a taper along the length of the waveguide. This taper was shown to bring the split modes, caused by the finite waveguide width, closer to the ideal Lamb mode. Though this is not a complete solution that eliminates all dispersion from the wave propagation, it gives a transducer designer an additional degree of freedom. By carefully selecting a specific taper angle it would be possible to limit the dispersive behaviour for a particular range of frequencies required for an application, providing an additional method by which the transducer may be optimised.

In addition to the complexity resulting from the geometry of the waveg-

uide, the operating conditions will have an effect on wave propagation within the waveguide strips. In the next chapter, the effect of a thermal gradient along the waveguide length will be discussed, both in terms of the physical effect on the wave propagation and on how such a gradient can affect the operation of a waveguide based transducer.

Chapter 6

Thermal Effects on Wave Propagation

As the waveguides used in the transducer design described in this work are intended to act as thermal buffers between a test fluid and a piezoelectric element, it is expected that there will be a large variation between the temperatures at the two ends of the strips. This will establish a thermal gradient along the length of the strip, which will in turn lead to variations of the material properties of the waveguide. These variations will influence the propagation of the guided waves along the strips and must be accounted for if found to be significant.

In this chapter these thermal issues will be addressed. Initially, the effect of elevated temperatures on Lamb wave propagation will be investigated. As mentioned in chapters 4 and 5, Lamb waves may be used as a simplified model of the propagation of guided waves in the rectangular cross-section strips. By studying the effect of heating on Lamb waves an indication of the behaviour that would be expected in the more complex geometry of the rectangular cross-section strips may be obtained. Next, experimental measurements of the effect of the thermal gradient on the propagation of guided waves in the rectangular cross-section strips will be discussed. Finally, using a computational fluid dynamics (CFD) model, the effect of

forming an array of strip waveguides on the thermal gradients along each waveguide will be investigated. Knowledge of any variations in the thermal gradients between the individual elements of the array will be essential in a practical application, where the advanced capabilities of an array transducer are to be exploited.

6.1 The Effect of Heating on Lamb Wave Propagation

In order to understand the effect that a thermal gradient will have on the propagation of ultrasonic waves in the strip waveguides, Lamb waves in stainless steel at elevated temperatures will first be discussed. Incorporating thermal effect into the Rayleigh-Lamb equations is relatively straight forward, as the material properties, dependent on temperature, may be used to determine the longitudinal and transverse sound velocities and simply be substituted into the Rayleigh-Lamb equations. However, these equations do not predict changes in attenuation so this will not be considered in the following, though a general increase in attenuation with temperature would be expected.

Dispersion curves were plotted for 316 stainless steel, with material properties taken for samples at several temperatures, over the expected operating range, at 24 °C, 150 °C, 200 °C and 470 °C [110, 111]. The dispersion curves obtained using these values are shown in figure 6.1. It can be seen that with increasing temperature, the frequency-thickness at which a particular wavenumber occurs for each mode is decreased. In addition, by looking at the linear region of the S0 mode, with a frequency-thickness below 1 MHz mm, it can be seen that as the temperature is increased the gradient of the S0 mode is reduced. Using the equations given in Chapter 4 both the phase and group velocities of the wave modes may be calculated. For the low frequency, linear region of the S0 mode, these velocities are both equal to the gradient of the curve. The wave velocity calculated for the plates at each of the temperatures are shown in table 6.1. From this it can be seen that as the

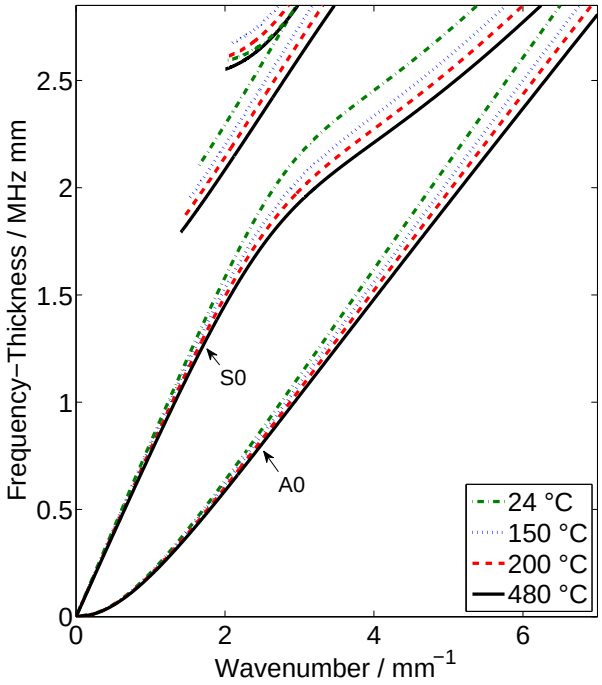

Figure 6.1: Lamb wave dispersion curves for a 316 stainless steel plate at a range of temperatures.

Table 6.1: The velocity of the S0 Lamb mode for frequencies below 1 MHz, in a 1 mm thick stainless steel plate at a range of temperatures.

Temperature (°C)	Wave Speed (ms^{-1})
24	5120
150	5050
200	4930
480	4810

temperature of the plate is increased the velocity of the wave mode is reduced, with approximately a 1.4 % reduction in the velocity for a plate at 150 °C, 3.7 % for a plate at 200 °C and 6.3 % for a plate at 480 °C, compared to room temperature.

A similar reduction in the velocity of the guided waves in the strip waveguides

would be expected, this would add an additional delay to the transmitted signal that would vary with temperature. This delay could interfere with the precise delays required for array techniques such as beam steering, and as such must be accounted for when considering transducer design such as the one described in this work.

6.2 Thermal Gradients in Finite Width Strips

Unlike the plates considered in the analytical model in the previous section, it would be expected that a waveguide acting as a thermal buffer would have a thermal gradient along its length, varying from the temperature of the test medium to the ambient temperature at the PZT element. The addition of this thermal gradient will reduce the overall effect of the elevated temperature on the mean wave velocity, however it will add further complexity to the system, preventing the effect from being calculated as simply as the previously discussed case.

In a standard contrapropagtion flowmeter, using some type of thermal buffer, knowledge of the exact magnitude of such a delay within the waveguide would not necessarily be required, as they would be cancelled in the calculation of the flow velocity. However, if the waveguide array discussed in this work is to be used to its full potential and the phased array aspects of the design utilised, knowledge of these delays becomes much more important, as additional unknown delays would make steering impossible, particularly if the individual waveguide elements in the array have different thermal gradients.

These thermal effects were investigated both experimentally and through the use of CFD modelling [112, 113]. The CFD modelling was conducted using the flow simulation package in the commercial software SolidWorks. Using this CFD technique allowed both the heat distribution through the waveguide and the heat dissipation to the surrounding medium, by conduction, convection and radiation, to be modelled simultaneously. Initially, the effect of a thermal gradient along

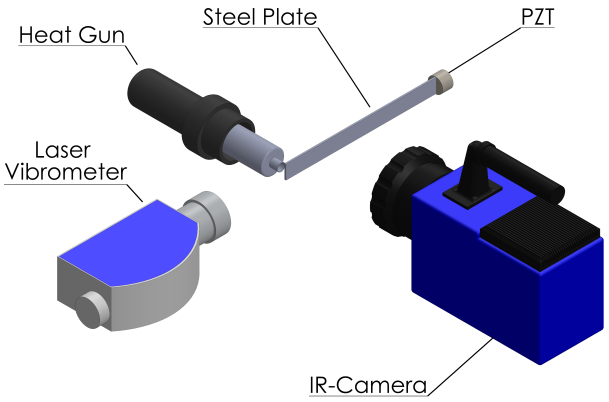

Figure 6.2: Schematic diagram of the experimental set-up used to investigate the effect of the thermal gradient on wave propagation within the waveguide strips.

a single waveguide strip was investigated experimentally. A PZT disc (PZT5A - Morgan Electro Ceramics, UK) with a through thickness frequency of approximately 150 kHz was mounted at on end of the waveguide strip. At the other end of the waveguide a hot air gun was positioned to act as a heat source, allowing a range of thermal gradients to be established along the length of the waveguide, with the temperature at the radiating face of the waveguide ranging from ambient to 250 °C. The temperature gradient along the waveguide strip was monitored using a Flir SC7000 infra-red (IR) camera, a schematic diagram is shown in figure 6.2 and an example of the IR camera images is shown in figure 6.3. For each of the temperature settings, the displacement of the radiating face of the waveguide strip was measured using a Polytec OFV-5000 laser vibrometer, while the piezoelectric element was driven with a 100 V square wave pulse, with a width of 5 μs, using an Olympus 5077PR Pulser-Receiver.

An example of one such displacement measurement is shown in figure 6.4. In this figure a series of reverberations may be seen, as the ultrasonic waves are internally reflected by the ends of the waveguide, with an associated reduction in

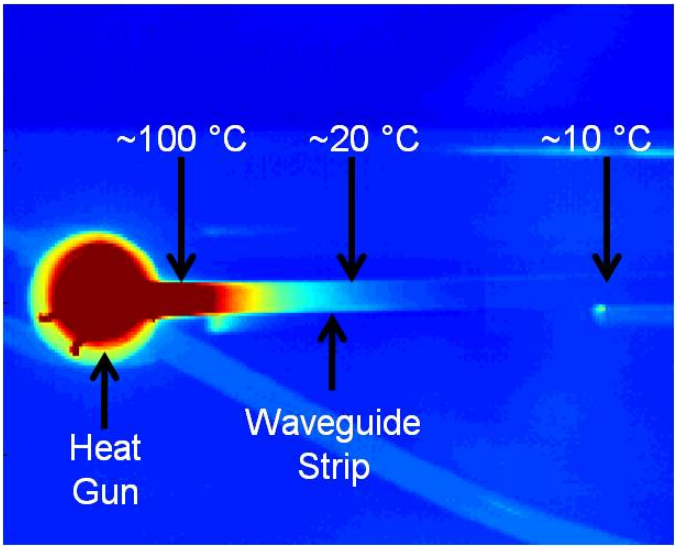

Figure 6.3: An example of an image of the strip taken with IR camera showing the thermal gradient along the strip.

amplitude with each reflection. To observe the effect of the varying thermal gradient on the propagation of ultrasonic waves within the steel strip, the mean propagation velocity may be measured experimentally. This could be done simply by finding the first zero crossing, but with this technique it is often difficult to define precisely the start of the signal, requiring more advanced techniques [114–116]. To avoid this issue, an alternate approach was used here to determine the mean propagation velocity from the frequency domain [116].

We begin by isolating the initial wave packet with a Hanning window. By applying a magnitude FFT to this measurement, the frequency response of the PZT disc and waveguide assemble may be obtained, as shown in figure 6.5. As would be expected the majority of the energy of the wave is centred around 150 kHz, the resonance of the driving PZT element. As the PZT is isolated from the heat source the frequency content of the signal should remain essentially independent of the thermal gradient. In order obtain the desired velocity information, a magnitude FFT may be applied to the entirety of the unwindowed signal, including the trailing reverberations. This FFT results in a series of peaks, which is a convolution of

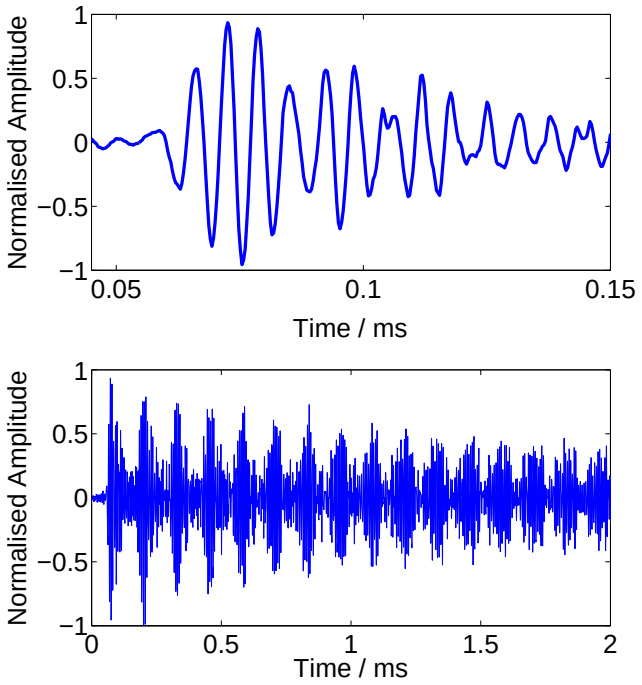

Figure 6.4: An example of the displacement measured at the front face of the waveguide strip using the laser vibrometer. At the top the initial wave packet has been isolated, below a longer trace is shown which includes the series of internal reflections.

the frequency response of the transducer and a second frequency arising from the reverberations of the pulse along the length of the waveguide. The spacing of the these peaks in the frequency domain can be related to the average sound velocity, $\bar{c}$ by:

$$\omega_n = \frac{n\pi\bar{c}}{L} \tag{6.1}$$

where L is the length of the strip, ω is the frequency at which a particular peak occurs and n is an integer. This technique has previously been used in NDT, in these cases the sound speed in the material is often well known and it is the thickness of the sample that is calculated. As n in this equation is simply an integer, it can be difficult to find the particular value of n relates to each peak, hence for this application equation 6.1 was modified to allow the calculation of $\bar{c}$ with no knowledge

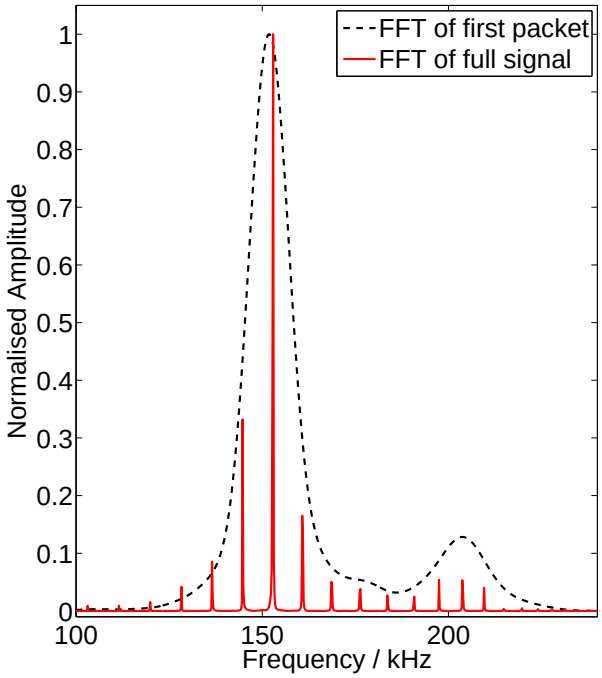

Figure 6.5: The resulting frequency spectra from applying an FFT to both the initial wave packet, shown with a dashed line, and the whole wave train including the reverberations, shown with a solid line .

of the value of n required:

$$\bar{c} = \frac{L(\omega_{n+1} - \omega_n)}{\pi}. \tag{6.2}$$

This allows the average sound velocity to be calculated from the spacing of adjacent peaks in the frequency domain. From the displacement measurements taken at a range of temperatures, the effect of the thermal gradient on the wave velocity may be plotted (figure 6.6). It can be seen that as the temperature at the radiating face is increased there is a gradual decrease in the mean velocity of the ultrasonic waves, as expected from the analytical modelling of Lamb waves. The reduction in velocity in the experimental measurements is less pronounced than in the Lamb wave model due to the presence of the thermal gradient along the length of the waveguide strips. Due to the poor thermal conductivity of stainless steel the majority of the

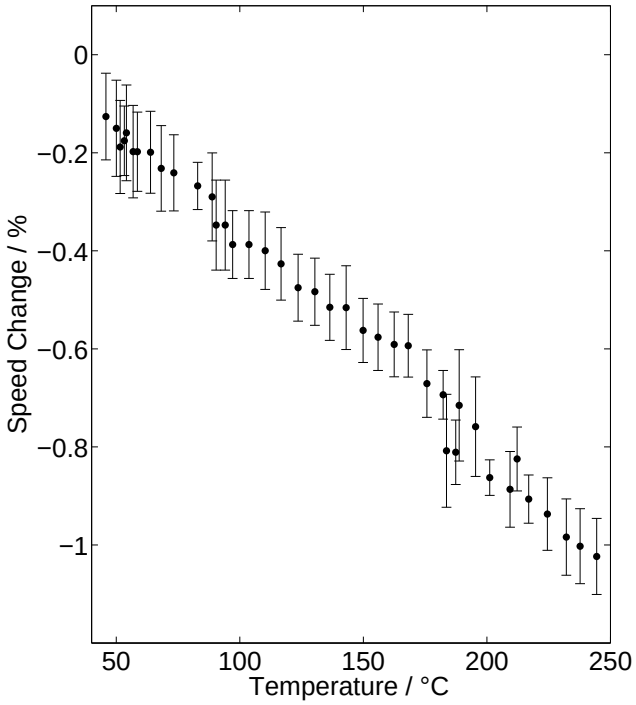

Figure 6.6: The change in average speed with increasing temperature calculated using the spacing between the peaks in the magnitude Fourier transform data. It can be seen that as the temperature at the radiating end of the strip is increased there was a drop in the average velocity of the ultrasonic waves travelling in the waveguide.

waveguide remains at ambient temperature when a heat source is applied to one end. This ensures that the piezoelectric element is well isolated from the potentially hostile environment. In turn, this causes the mean velocity in the waveguide to be higher than predicted by the simple analytical model at a fixed temperature, with increasing deviation as the temperature is increased.

6.3 Thermal Variation Across the Waveguide Bundle

These variations in velocity could be a particular problem if the thermal gradients along each of the waveguide strips in the array are not the same, which could occur as a result of variation in cooling of the strips due to their positions in the array.

This would add a different delay to each of the individual elements, negating the possibility of steering, without significant calibration. In order to fully investigate these effects the waveguide strips cannot be considered in isolation, as this is not a practical design, and must instead be considered inside some type of sealed housing, as they would be in an application.

This imposes practical limitations, as monitoring the thermal gradient along five individual waveguides with the IR camera used previously would be difficult, even without the transducer housing. Other techniques which may be able to provide this temperature information inside the housing, such as an array of thermocouples, would almost certainly interfere with the cooling of the waveguides, limiting the usefulness of the obtained data. Instead, it was decided to use a CFD model to simulate the heat distribution within the transducer, allowing the temperature distribution along each of the waveguides to be obtained.

Before simulating the entirety of the transducer, a single waveguide strip was modelled, in order to allow experimental validation of the modelling technique. The initial model consisted of a single stainless steel strip inside a box of air, with the box being large enough that any heating of the waveguides would have little effect on the surrounding ambient temperature. A 1 mm length at one end of the strip was set to have a fixed temperature and the model was then allowed to continue until an equilibrium state was achieved. The temperature profile along the length of the strip was then recorded and compared to the experimentally measured temperature profile, shown in figure 6.7. A high degree of correlation can be seen between the experimental data and the CFD modelling with less than a 5 % variation between the two over the length of the waveguide. A small discontinuity can be seen in the experimental temperature profile. This is a result of experimental limitations, as it was necessary to remove the heat source to allow the IR camera to measure only the temperature profile of the strip, as this would be masked by the high temperature of the hot air gun. This allowed a small amount of time in which the waveguide

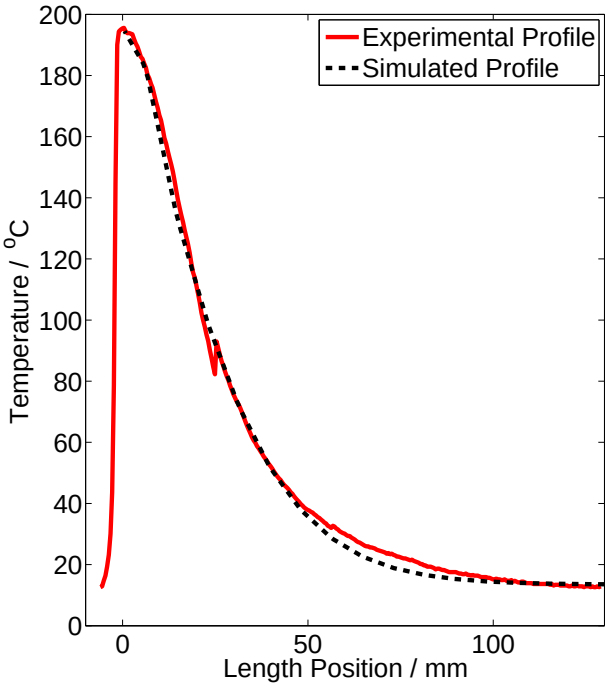

Figure 6.7: The experimentally measured temperature profile along the length of a 1 mm x 10 mm x 300 mm strip, solid line, and the temperature profile from a computational fluid dynamic model of a similarly heated strip, the dashed line.

began to cool, leading to the small discontinuity.

As the model agreed well with the experimental measurements, the model was modified to incorporate the full five plate array inside a sealed casing. As before, a fixed temperature heat source was applied to one end of each of the strips in the array and the system was allowed to reach an equilibrium state. The temperature gradient along the length of each of the strips was recorded to assess the degree of variation in the temperature gradients between the individual elements. This simulation was repeated for a range of strip separations to assess how this affects the variation between the elements. Figure 6.8 shows the variation between the temperature profile along the central strip in the bundle, and that of one of the outermost elements for a range of element spacings. These two particular elements of the array were selected as these would be expected to have the largest variation.

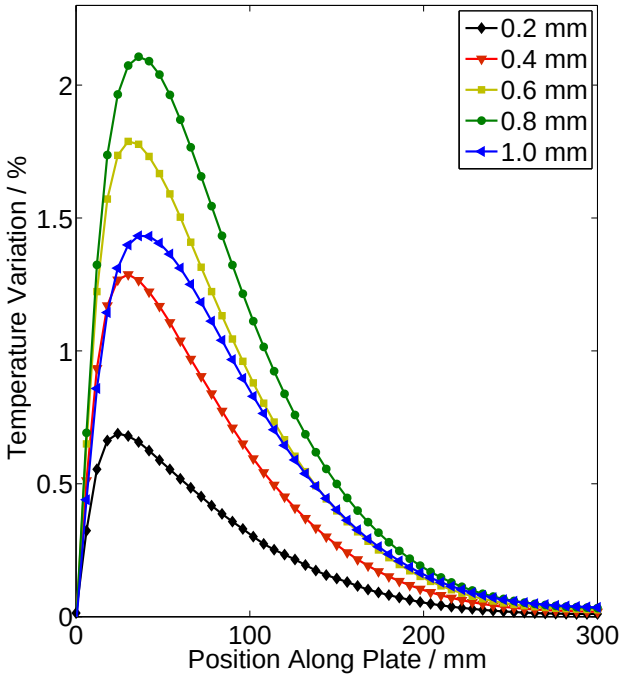

Figure 6.8: Shown here is the variation in the temperature with length between the strip in the centre of the bundle and a strip at the edge of the bundle, inside a sealed housing. It can be seen that as the spacing between the strips is increased the variation increases. However a spacing greater than 0.8 mm causes a reduction in temperature variation.

From figure 6.8 it can be seen that the smallest variation between the waveguides occurs when the spacing is small, with less than a 0.7 % variation in the thermal gradients between the central strip and the edge strip for plate separation of 0.2 mm. With increasing separation between the waveguides this variation between the inner and outer waveguide strips increases, implying that by keeping the separation small the temperature profiles along each of the waveguide elements may be kept consistent across the bundle of waveguides. One interesting point of note is that when the spacing between the strips is larger than 0.8 mm the variation between the temperature gradients on the two waveguides decreases. This was found to result from the air inside the housing reaching a higher temperature than with the smaller spacings, which is most likely a result of the larger effective volume

inside the housing that was occupied by the waveguides which in turn prevented convective currents from cooling the system as efficiently. The result of this is that the temperature gradients along each of the waveguide strips are more similar than for a slightly smaller spacing, however a larger length of waveguide is required to isolate the PZT element as the strips are not cooled as efficiently.

It is this variation between the individual strips in the array that could negatively influence the array performance. If we look at the case of one of the waveguide strips radiating into a fluid at 250 °C a reduction in average velocity of approximately 1 % was observed. This corresponds to a delay of around 0.6 μs due to thermal effects. Next if we assume the "worst case scenario" from figure 6.8 and say that there is a 1 % variation between adjacent strips this would give a delay between adjacent elements of 0.06 μs, with the largest delay on the centre element. The effect of these delays would be a slight focusing the emitted waves, with the focal point becoming closer as the thermal variation between the strips increases. In this case, in air the focal point would be approximately 40 mm from the front face of the transducer, thought the case described here is slightly exaggerated compared to what would be expected practically. If these delays were found to cause a significant problem in practical operation it should be possible to use the reverberation technique described in this chapter to calibrate the transducer, removing these delays.

6.4 Conclusions

In this chapter it has been shown that the thermal gradient along the length of the waveguide will cause some variations in the way in which an ultrasonic wave will propagate along the waveguide. As the temperature of the target fluid is increased, a reduction of the average wave speed in the waveguide was observed, as expected from the Lamb wave models. In addition it has been found, using CFD models,

that small variations exist between the thermal gradients of the individual elements in the waveguide array, with a dependence on the spacing of the array elements. Though these effect are small, the combination of the varying wave speed and the differing thermal gradients could combine to add unknown delays to the signals from each of the array elements, preventing the possibility of using the waveguide array for applications such as steering if not accounted for.

Thermal consideration will also play a key role in the following chapter where a matching layer suitable for the waveguide transducer will be discussed. The addition of a matching layer should improve the efficiency of the transducer. However, the potentially hostile operating conditions must also be considered when selecting a material for use as matching layer.

Chapter 7

Matching Layers for a Waveguide Transducer

Although the waveguide transducer has been shown to function effectively as a thermal buffer, the next concern is whether the transducer is capable of efficiently transmitting energy into the target medium. One factor which may reduce this efficiency is the mismatch between the acoustic impedances of the material of the strip waveguides and the target fluid. In this chapter, a potential solution to the issues caused by such an impedance mismatch will be discussed. To begin, the properties of an ideal matching layer for this application will be considered, in terms of acoustic impedance and thickness. Next two materials are suggested as potential candidates as matching layer materials for the waveguide transducer to operate in harsh environments. The optimisation of the acoustic properties of these materials through the use of filler loading is then discussed. These optimised materials are then studied using FE modelling to determine the appropriate matching layer thickness for the waveguide application. Finally, the manufactured prototype matching layers were mounted onto strip waveguides and assessed in water.

7.1 Acoustic Impedance

The acoustic impedance of a material describes the degree to which a material opposes the propagation of acoustic waves. This property, Z, can be calculated as:

$$Z = \rho c, \tag{7.1}$$

where ρ is the density of the material and c is the sound speed. When an acoustic wave meets a boundary between two materials with differing acoustic impedances, the energy of the incident wave will be split, with part of the wave continuing onwards through the boundary and the other part reflected. The relative energies of the two components may be calculated as a pair of coefficients, R and T, for reflection and transmission respectively:

$$R = \left(\frac{Z_2 - Z_1}{Z_2 + Z_1}\right)^2, \tag{7.2}$$

$$T = 1 - \left(\frac{Z_2 - Z_1}{Z_2 + Z_1}\right)^2 = 1 - R, \tag{7.3}$$

where Z_1 and Z_2 are the acoustic impedances of the material in which the wave originates, and the target material respectively. These equations are only valid for the simplest case of normal incidence on the boundary. If this was not the case an additional term would be needed to account for the angular dependence. From equations 7.2 and 7.3 it can be seen that if the two materials have highly dissimilar acoustic impedances the reflection coefficient, R, will be significantly higher than the transmission coefficient, T. As such, the majority of the energy incident on a boundary will be internally reflected, which is not useful in many practical applications.

For an acoustic transducer, it is clear that it would be desirable to avoid such an impedance mismatch between the transducer material and the target medium

Table 7.1: Acoustic properties of the materials used in this work at 20.0 °C

Material	Density (kgm^{-3})	Longitudinal Velocity (ms^{-1})	Acoustic Impedance (MRayl)
Stainless Steel	7900.0	5900.0	46.0
Air	1.24	343.0	0.43×10^{-3}
Water	1000.0	1500.0	1.5
Bakelite	1599.4	3248.1	5.2
Stycast	2263.2	3110.5	7.0

to ensure efficient transmission into the target. However, in many applications, particularly fluid coupled applications, this is not possible. For the example of the waveguide transducer discussed in this work, it is desired that the ultrasonic waves are transmitted from the stainless steel waveguides into a fluid, for example air or water. Using the acoustic properties given for these materials in table 7.1 the relevant reflection coefficients can be calculated to be 0.878 and 0.999 for water and air, respectively. Clearly with such large reflection coefficients it is difficult to design an efficient transducer, as the majority of the wave energy is reflected back into the waveguide.

In order to reduce these large energy losses, it is common practice to place one or more layers of an additional material between the source material and the target material [56, 117, 118], called matching layers. The addition of a matching layers allow a boundary with a large impedance mismatch to be broken down into a series of boundaries. Each of these individual boundaries has a smaller mismatch in acoustic impedance, allowing a net increase in the magnitude of the transmission coefficient, giving a more efficient transducer.

Ideally the transition between the two acoustic impedances, of the source and target materials, would be very gradual, using a series of infinitesimally small matching layers, each with a small variation in acoustic impedance, allowing a grad-

ual transition and maximising the transmitted energy [118]. However, such matching layers are not commonly used in ultrasonic transducers due to the high manufacturing costs that would be associated with the production of such matching layers [12]. Instead, it is more common to use a single matching layer with an intermediate acoustic impedance, Z_{ML} given by [119]:

$$Z_{ML} = \sqrt{Z_1 Z_2}, \tag{7.4}$$

where Z_1 and Z_2 are the acoustic impedances of the materials to be matched.

If we substitute the values give in table 7.1, for stainless steel and water for example, into equation 7.4 it can be seen that the ideal acoustic impedance to use as a single layer matching layer would be 8.3 MRayls. If this value is substituted into equation 7.3, it can be shown that the fraction of the energy that is transmitted into the water from the steel, through the matching layer, increases to 0.269, from 0.122, allowing more efficient operation.

In addition to the matching layer material, the geometry of the matching layer can have a significant effect on the effectiveness of the layer. It is common practice when designing matching layers ensure that it has a thickness equal to $\lambda/4$, where λ is the wavelength of the ultrasonic wave [12]. Using a matching layer with this thickness allows any fraction of the wave that is internally reflected within the matching layer to constructively interfere with the subsequent wave, giving a net increase in transmitted energy. However, this narrows the bandwidth of the transducer, as this enhancement is only valid for the single frequency selected.

7.2 Matching Layer Material Selection and Characterisation for a Strip Waveguide

For this application, the matching layer material cannot be selected purely for its acoustic properties. The desired operating conditions, discussed in the previous chapter, must also be considered. With this in mind, two materials were identified as being potentially suitable for use as a matching layer for the strip waveguide transducer, stycast (2850-FT, Emerson & Cuming) and bakelite (Polyfast, Struers). Rather than attempt to select one material which is suitable for all potential applications two materials were chosen for opposite ends of the temperature range, stycast, a polymer often used in cryogenic applications for the lower temperature range (the manufacturer stated operating range is between -40 °C to 130 °C, however, this polymer has been shown to be usable at temperatures as low as -270 °C [120–122]), and bakelite, a phenolic resin for the higher temperature range (from -10 °C up to around 200 °C).

The relevant acoustic properties for these materials are also given in table 7.1. From this it can be seen that the acoustic impedance of the two materials are lower than the ideal value of 8.3 MRayl, with values of 5.2 MRayls and 7.0 MRayls respectively for bakelite and stycast. When designing matching layers for ultrasonic transducers it is not uncommon to add some type of filler, such as hollow glass beads, to the matching layer material. These filler materials usually have very different densities to the matrix material, which is often some type of epoxy, allowing the density and acoustic impedance of the formed composite material to be controlled by varying the quantity of filler material added. However, when using filler materials there are a few additional factors that must be considered. Firstly, the particle size of the filler should be sub-wavelength. This prevents scattering from the particles of the filler material, which would increase attenuation and allows the composite to appear as a single material to any incident ultrasonic waves, rather than two separate

components. Secondly, the filler material must be distributed evenly throughout the matrix to ensure the desired acoustic properties.

In order to increase the acoustic impedances of the materials to closer match the ideal value, samples of both stycast and bakelite were produced, loaded with tungsten powder, containing particles sized between 0.6 μm and 1.0 μm (Sigma-Aldrich). Tungsten was selected for its very high density, which should minimise the amount needed as a filler material to achieve the required acoustic impedance. There are a range of models which may be used to predict the acoustic properties of a two phase material consisting of a matrix, such as a polymer, with a filler [123–125]. One of the most commonly used of these models, the Ruess model [125], states that the acoustic impedance, Z_{comp}, and the density ρ_{comp} of a composite material may be calculated as:

$$Z_{comp}^2 = \frac{Z_M^2 Z_F^2 (m_M + m_F)}{Z_M^2 m_F + Z_F^2 m_M}, \tag{7.5}$$

$$\rho_{comp} = \frac{\rho_M \rho_F (m_M + m_F)}{\rho_M m_F + \rho_F m_M}, \tag{7.6}$$

where m refers to the mass fraction and the subscripts M and F refer to the matrix and filler materials respectively.

To ensure the validity of these models in predicting the properties of the materials used here, a series of samples (30 mm diameter discs, with thickness of approximately 10 mm) of both stycast and bakelite were produced, with a range of tungsten loadings. The two materials are manufactured in very different manners. Stycast is manufactured using two fluid components, which when mixed cure over a period of a few hours at a temperature of 65 °C. This material required substantial degassing to prevent air bubbles from being present in the final sample discs. The bakelite starting material is a powder, which was ground and sieved such that the grain size was comparable to that of the tungsten particles, to allow a more even distribution. The bakelite samples were then manufactured by compressing the powder under a pressure of 250 bar at an elevated temperature. Each of these

samples was then characterised to obtain the sound speed, density and acoustic impedance.

The longitudinal velocity in the matching layer was measured using a simple, contact method. A 2.25 MHz PZT transducer was coupled to the surface of each the samples, a 400 V negative square pulse, with a width of 0.23 μs was then applied to the transducer, using a pulser-receiver (Olympus 5077PR), in a pulse-echo configuration. The sound velocity was then calculated from the separation of the echoes in the received signal, and the known thickness of the sample. The density of each sample was then measured using a technique based on Archimedes' principle. To measure the density of the samples with this technique, each sample was weighed twice, first in air, W_{air} and then submerged in distilled water, W_{water}, at a known temperature. When the sample is fully submerged in water there is an upward buoyant force which acts on the sample, reducing the effective weight of the sample by an amount equal to the weight of the displaced water, allowing the density of the sample to be calculated as:

$$\rho = \frac{W_{air}\rho_{water}}{W_{air} - W_{water}}. \tag{7.7}$$

This method allows the density to be measured accurately, without the need for any knowledge of the volume of the sample, reducing the number of factors which could add uncertainty to the measurements, as features such as texture on the sides of the samples from the mould in which the sample was manufactured can make accurate volume measurements difficult.

The experimentally measured acoustic impedance, density and acoustic velocity for the samples with a varying mass ratio were then plotted against the theoretical values, calculated using equations 7.5, 7.6 and 7.1, shown in figures 7.1 and 7.2 for the loaded stycast and bakelite samples respectively. From these figures it can be seen that equations 7.5 and 7.6 describe these tungsten loaded materials well,

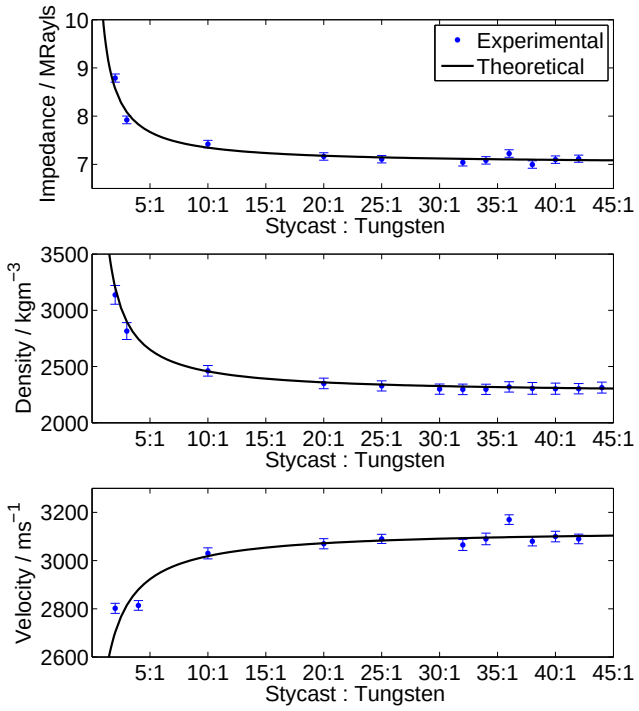

Figure 7.1: The acoustic impedance, density and velocity for stycast loaded with tungsten at a range of mass ratios.

with a high degree of correlation between the theoretical values and those measured experimentally. From these plots it can be seen that the ideal acoustic impedance of 8.3 MRayls a mass loading ratio of 2.5:1 and 0.6:1 would be required for stycast and bakelite respectively. The samples with the acoustic impedances closest to this value were selected: a 2:1 ratio for stycast, with an acoustic impedance of 8.7 MRayls, and a ratio of 1:1 for bakelite, with an acoustic impedance of 7.2 MRayls. The bakelite sample selected had an acoustic impedance that was still significantly smaller than desired, which was due to manufacturing limitations. For mass fractions higher that 1:1 the bakelite was found to saturate, causing the samples produced to crumble and limiting their usefulness as a matching layer.

Another important property of the samples that was measured for each of these four materials is the ultrasonic attenuation. The attenuation was measured

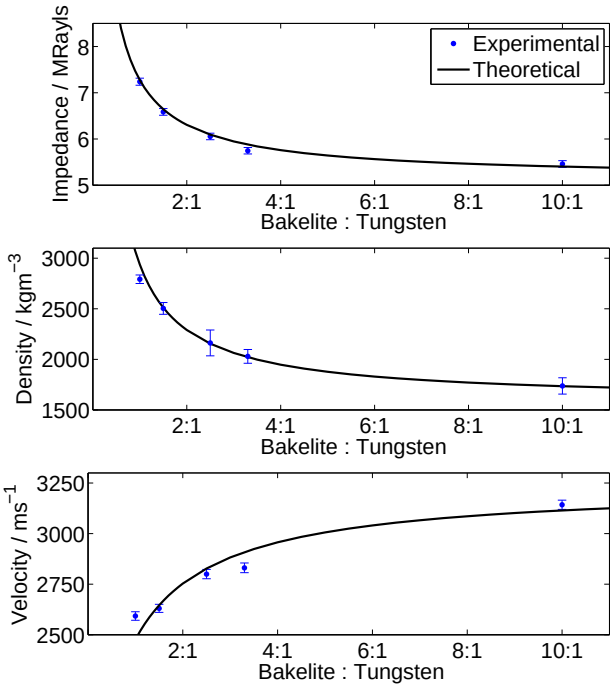

Figure 7.2: The acoustic impedance, density and velocity for bakelite loaded with tungsten at a range of mass ratios.

using through transmission immersion technique. Each sample was placed between a pair of identical transducers, with a separation of 300 mm between them, in a tank of water at 20 °C [125–128]. One of the transducers was then driven using a pulser-receiver with the signal transmitted through the sample recorded on the second transducer. A second measurement was then taken without the sample present, allowing the attenuation of the sample material, α_s to be calculated from the spectra of the two signals using:

$$\alpha_s = \alpha_w + \frac{\ln(T) + \ln(A_w) - \ln(A_s)}{L}, \tag{7.8}$$

where α_w is the attenuation of water, T is the transmission coefficient, and A_w and A_s are the amplitudes of the measured signals in the frequency domain for water and with the sample respectively.

Table 7.2: The measured attenuation of the matching layer materials.

Material	Attenuation		
	at 0.5 MHz (dBm^{-1})	at 1.0 MHz (dBm^{-1})	at 2.25 MHz (dBm^{-1})
Stycast	227 ± 1	262 ± 14	359 ± 11
Stycast Loaded	239 ± 1	291 ± 10	425 ± 27
Bakelite	101 ± 5	110 ± 7	134 ± 12
Bakelite Loaded	254 ± 8	283 ± 1	576 ± 8

For each sample these measurements were repeated using three pairs of transducers, with frequencies of 0.5 MHz, 1.0 MHz and 2.25 MHz. Although these frequencies are higher than the frequencies at which the waveguide transducer is intended to operate, they can give an indication of the relative attenuation of each of the samples at a frequency around 150 kHz. These values are given in table 7.2. From this table it can be seen that the addition of the tungsten increased the attenuation of both the stycast and the bakelite, as would be expected. This increase was found to be much larger for bakelite, which may offset some of the expected improvements expected from the bakelite samples from the better impedance matching.

7.3 Optimum Matching Layer Dimensions

With the loaded samples selected, a series of FE models were conducted to optimise the dimensions of the matching layers. In the FE models, a single rectangular cross-section stainless steel waveguide (1 mm x 10 mm 300 mm) was simulated with a matching layer of either stycast, bakelite, 2:1 stycast loaded with tungsten or 1:1 bakelite loaded with tungsten at one end. At the opposite end of the waveguide a single cycle sine wave with a frequency of 150 kHz was applied as a force to the 1 mm x 10 mm cross-section face. The emitted pressure was then measured 5 mm

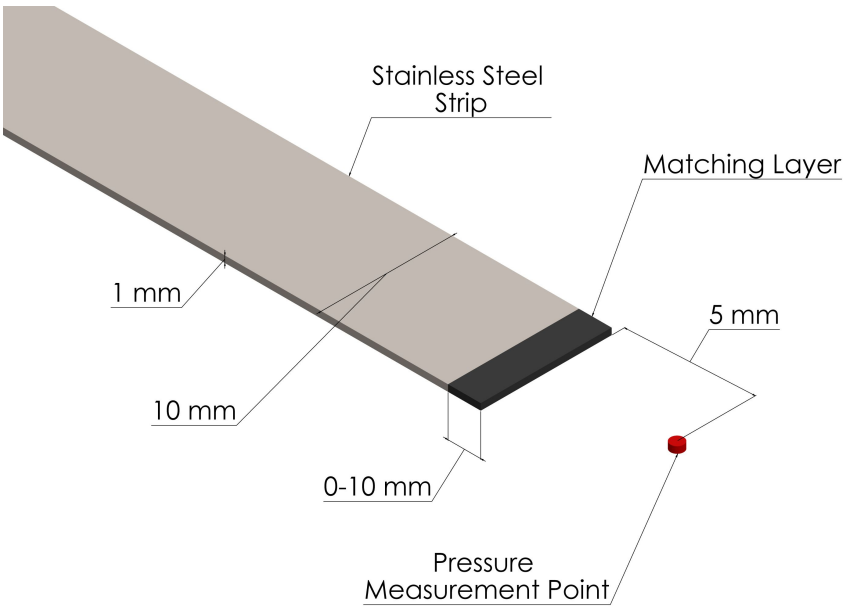

Figure 7.3: A schematic diagram of the FE model used to study the effect of the matching layer thickness on the emitted pressure from a stainless steel waveguide.

in front of the radiating face of the waveguide and the maximum pressure recorded. For each of the four matching layer materials the model was repeated for a range of thicknesses between 0 mm and 10 mm in increments of 0.1 mm, as shown in figure 7.3. This range includes the $^{\lambda}/_{4}$ thickness value for each of the materials, and would allow the optimal thickness to be found.

The results from these simulations are shown in figure 7.4, and summarised in table 7.3. The values plotted in figure 7.4 have been scaled to allow the effect of varying the matching layer thickness to be seen more clearly. From these results it can be seen that the optimum matching layer thickness was found to be consistently smaller than $^{\lambda}/_{4}$ which is expected for a traditional transducer design.

This difference between the matching layer for a traditional transducer and the waveguide transducer is thought to occur as a result of the complex way in which the ultrasonic waves propagate within the waveguide strips. The geometry of the strip causes the different frequency components of the signal to travel with

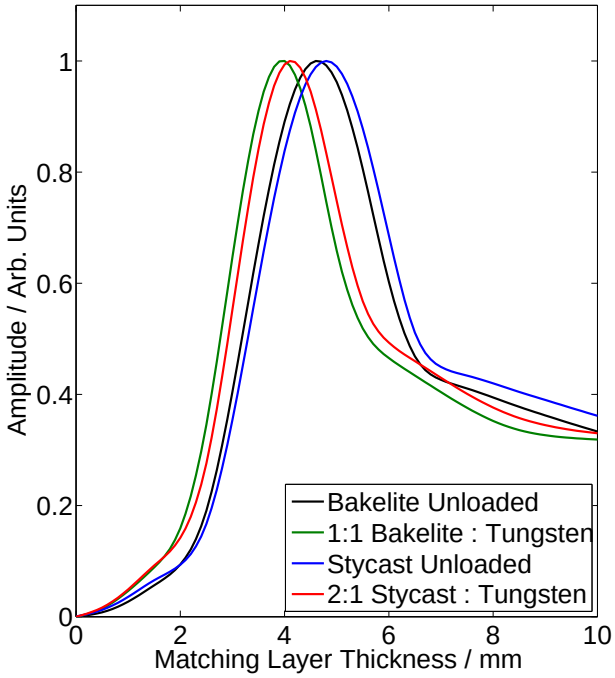

Figure 7.4: The effect of matching layer thickness on the emitted amplitude for stycast, bakelite and their loaded counterparts from FE modelling.

Table 7.3: Acoustic properties of the materials used in this work

Material	Mass Ratio Material : Tungsten	$\lambda/4$ at 150 kHz (mm)	Optimum Thickness (mm)
Stycast	1 : 0	5.2	4.8
Stycast Loaded	2 : 1	4.7	4.1
Bakelite	1 : 0	5.4	4.6
Bakelite Loaded	1 : 1	4.3	3.9

slightly different velocities. As such, a matching layer with a thickness of $\lambda/4$ of the desired operating frequency would not necessarily provide the greatest increase in output amplitude, as the trailing waves would be expected to have a slightly different frequency.

To confirm this, another set of simulations was undertaken. As before the thickness of a stycast matching layer was varied, with the maximum pressure recorded 5 mm from the radiating face when driven with a single cycle, 150 kHz, sine wave pressure load. However, in these models the length of the waveguide was also varied between 50 mm and 700 mm, with the optimum matching layer thickness found for each waveguide length. If this deviation from the $^{\lambda}/_{4}$ optimum thickness is a result of dispersive propagation in the strip waveguide, then it would be expected that the optimum matching layer thickness would be dependent on the length of the waveguide. The results of these simulations are shown in figure 7.5. From this figure it can be seen that is a clear dependence of the optimum matching layer thickness and the length of the waveguide. A line has been added to highlight the observed trend as the length of the waveguide strip was varied. As the length of the waveguide is increased, the optimum matching layer thickness also increases. However this effect does not follow a simple trend, making it difficult to predict the optimum matching layer thickness for such an application, requiring additional work to ensure the matching layer is ideally suited to the desired application.

7.4 Experimental Validation

As the optimum matching layer thickness for each of the materials had been identified with the FE modelling, a set of waveguide strips (1 mm x 10 mm x 300 mm, 316 stainless steel) were manufactured, one with each of the optimised matching layers, to allow experimental validation. The emitted pressure from each of the waveguide strips was then measured in a tank of water. In order to assess the effectiveness of the matching layer any other factors that could cause variations in the emitted amplitude should be minimised. One factor that could cause such a variation is the way in which the strip is driven. With a piezoelectric element, it is possible that the coupling between the PZT and the waveguide could be inconsistent, for exam-

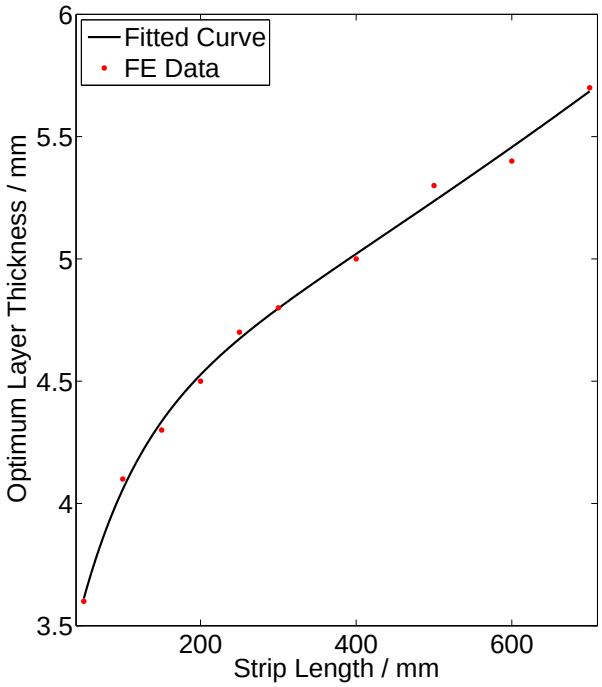

Figure 7.5: The affect of the waveguide length on the optimum matching layer thickness.

ple the piezoelectric element may not be perfectly aligned with the relatively small face of the waveguide strip. In an effort to reduce this effect an EMAT was used to generate the ultrasonic signals in the strips, which should reduce any inconsistencies in the ultrasonic generation source and conditions. The EMAT used for this work consisted of a coil with a fixed magnetic field, aligned as shown in figure 7.6. By aligning the electric and magnetic fields in this manner an in plane force aligned along the direction of the length of the strip would be generated.

The EMAT was driven using a 5 cycle, 150 kHz signal with a RITEC RPR-4000 pulser-receiver. The pressure emitted from the waveguide was then measured with a hydrophone at a distance of 5 mm from the radiating face. The maximum pressure measured for each waveguide and matching layer combinations is shown are given in table 7.4. The values in this table have been normalised with respect to the

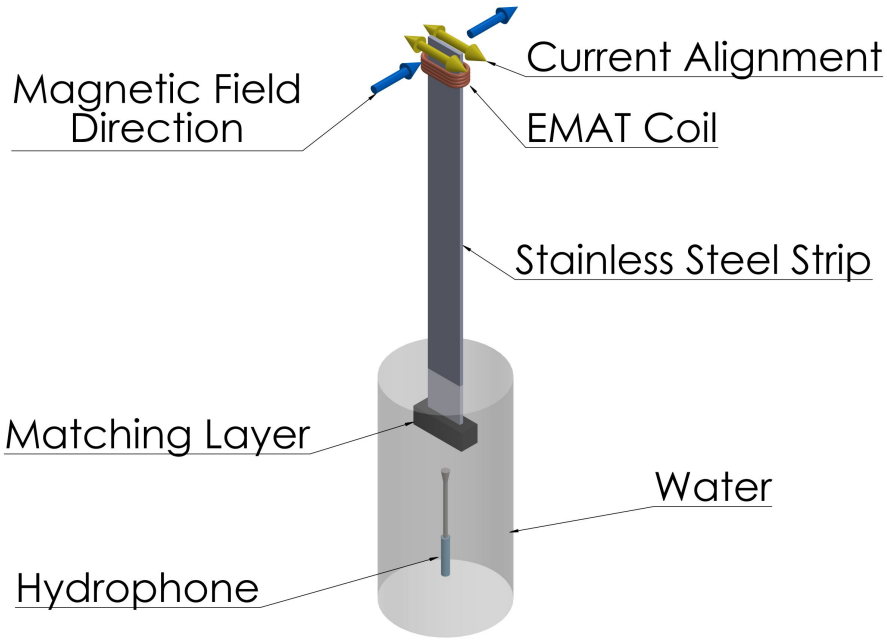

Figure 7.6: A schematic diagram of the experimental set up used to measure the emitted pressure from the waveguide assembly.

pressure measured with no matching layer to ease comparison. From these results it is clear that the addition of any of these materials as a matching layer provides a significant increase in the transmitted pressure, with an increase of between 2.15 and 3.40 times in the emitted pressure. The loaded stycast was found to give the greatest increase in emitted pressure, which would be expected as it had an acoustic impedance closest to that of the ideal matching layer material for this application. The pure stycast and the tungsten loaded bakelite were found to give similar increases in performance, with an increased pressure of 2.19 and 2.15 respectively. This again is expected as the two materials were found to have similar acoustic properties, with the loaded bakelite having a slightly better impedance match, but a higher attenuation. Unloaded bakelite however was found to perform much bet-

Table 7.4: The maximum measured pressure with the addition of a matching layer normalised with respect to the no matching layer case.

Material	Maximum Pressure
None	1.00
Stycast	2.19
Stycast Loaded	3.40
Bakelite	2.89
Bakelite Loaded	2.15

ter as a matching layer than expected, giving an increase in emitted pressure of a factor of 2.89. Although this sample was not as optimised as the loaded sample in terms of acoustic impedance, it can be seen that the significantly lower attenuation, compared to the other three materials studied, allowed a larger improvement in the emitted pressure than either the unloaded stycast or the loaded bakelite.

7.5 Conclusions

In this chapter a matching layer for a waveguide transducer has been discussed. Two materials, stycast and bakelite, were selected for their thermal properties as potential matching layer materials. The acoustic properties of these materials were then tailored, through the addition of tungsten loading, such that their acoustic impedances more closely resemble that of a theoretical ideal matching layer for the transition from stainless steel to water. For other fluids with significantly different acoustic impedances this optimisation would need to be repeated. However, the basis presented here should allow this process to be repeated more rapidly.

The optimum matching layer thickness for coupling waves into water at room temperature for these materials was then investigated using FE modelling. From

these models it was shown that the design rules used in traditional transducer construction do not necessarily apply for waveguide transducers. From the FE modelling presented in this chapter, it has been shown that the optimum matching layer thickness for a waveguide transducer in not simply the conventional $^{\lambda}/_{4}$ thickness, but is also dependent on the length of the waveguide. For the waveguide discussed in this work, this results in an optimum matching layer with a thickness which is slightly smaller than $^{\lambda}/_{4}$. It was then demonstrated experimentally that the addition of such a matching layer to a waveguide strip can provide an increase in the maximum emitted pressure of up to 3.4 times, when operating in water, compared to the case where there is no matching layer. From these studies it has also been shown that the attenuation of the matching layer material can play as an important role as the acoustic impedance, as it was shown that the bakelite matching layer, with an acoustic impedance of 5.2 MRayls gave a larger increase in the emitted pressure than the better impedance matched stycast or loaded bakelite. Though the addition of such a matching layer is beneficial for many applications, including fluids such as steam, the materials discussed here would not be suitable for temperatures above 200 °C. Though this range could be extended slightly through the use of alternate bakelite compositions and stycast with other catalysts, however this would not cover all temperature ranges, particularly at very high temperatures. If the transducer needed to operate under such conditions, further work may be required find a suitable material material which can act as a matching layer and withstand the elevated temperatures. If a suitable matching layer could not be identified for a particular application, then the results indicate that one could rely instead on larger driving voltages to achieve the desired signal amplitudes.

In the following chapter, the capabilities of the strip waveguide transducer to function as a phased array will be assessed, demonstrating the full capabilities of the transducer design presented in this work.

Chapter 8

Characterisation of the Array Waveguide Transducer

One of the main advantages of the transducer design suggested in this work, compared to those currently in use, is the ability to exploit the additional power and flexibility offered by inclusion of an array of transducers. In a field such a flow measurement, the ability to steer the output from the array would allow the correction of phenomena such as beam drift at high flow velocities or even to interrogate the flow along multiple paths with a single pair of transducers. Additionally, the steering capability may allow the transducer to be mounted normal to the pipe wall, both minimising any protrusion into the flow.

In this chapter the steering capabilities of the strip waveguide array transducer will be investigated. To begin, a series of FE models will be discussed. Initially these models will be used to determine a suitable array geometry, identifying the maximum allowable array pitch, which will provide suitable beam properties for the desired application. Once the required array pitch has been determined, further FE models will be presented to demonstrate the steering capabilities of the strip waveguide array. In addition the inclusion of the waveguide strips in the array we also suggest an alternative method of driving an ultrasonic array. Rather than us-

ing a traditional diced piezoelectric element to drive the array, each element will be driven using the radial motion of a cylindrical piezoelectric rod, providing a simpler, method of constructing a phased array probe, with minimal crosstalk. This crosstalk will also be discussed further, using both FE modelling and experimentally, in order to assess the influence of crosstalk in the waveguide array. To allow this experimental validation, a custom low frequency phased array controller has been designed and constructed to drive the array, which will also be described here.

8.1 Finite Element Study of a Strip Array Transducer

8.1.1 The Effect Array Pitch on Directivity

As the waveguide geometry was determined by practical considerations, i.e. an array consisting of five rectangular, stainless steel elements with a width of 1 mm and length of 300 mm, the main feature which we may vary in the design is the pitch of the array. As a starting point, we may calculate the theoretical $^{\lambda}/_{2}$ limit, the maximum pitch at which the side lobes will be suppressed. In air a frequency of 150 kHz corresponds to a wavelength of 2.29 mm, giving a pitch of 1.145 mm. A series of FE models were then conducted to investigate the effect of varying the pitch on the performance of the array. Three array pitches were instigated using two dimensional FE models, 1.15 mm (approximately fulfilling the $^{\lambda}/_{2}$ requirement), 1.25 mm and 1.50 mm. Two dimensional models allowed the computational requirements to be minimised, but should have a limited effect on the directivity of the transducer. This is a result of the large aspect ratio of the physical array elements, allowing the field to be considered in a single plane, as discussed in chapter 3.

In the model, the array was positioned in the centre of a large box of air and a single cycle sine wave, with a frequency of 150 kHz, was applied to one end of each of the strips as a pressure load. This avoids any additional complications that would be added with the inclusion of a piezoelectric element, allowing the directivity of the

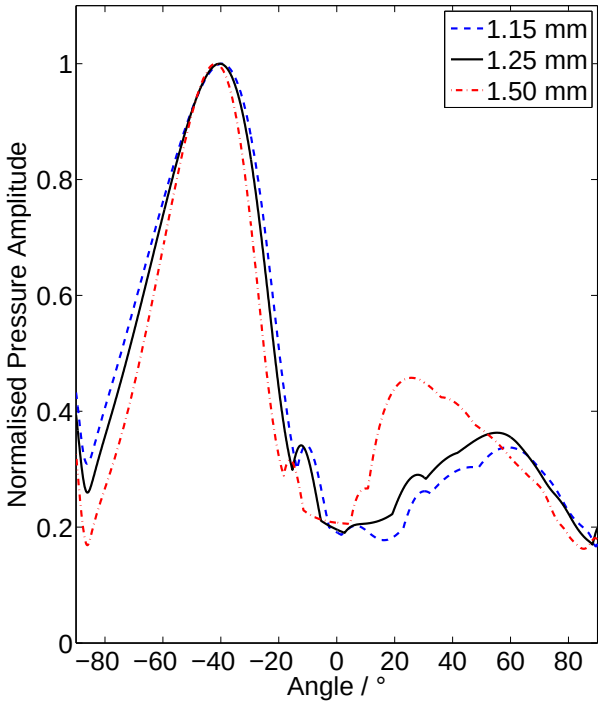

Figure 8.1: The simulated directivity profile for a five element strip waveguide array transducer steered to 45° for a array pitches of 1.15 mm, 1.25 mm and 1.50 mm.

strip array to be studied in isolation. The directivity was measured at a distance of 200 mm from the radiating face, with the beam steered to an angle of 45° using appropriate delays on each of the elements. By measuring the directivity while steering at a high angle (in this case, at 45°, which is towards the upper end of the angular steering range desired for this application), any side lobes should be more pronounced.

The measured directivity profiles may be seen in figure 8.1, with the key characteristics relating to each of the profiles given in table 8.1. As would be expected from the theory for conventional arrays discussed in chapter 3, the width of the main beam decreases with increasing pitch, as the aperture of the array increases, with the FWHM decreasing from 54.7°, for a pitch of 1.15 mm, to 42.6° for a pitch of 1.50 mm. However, the main effect of varying the pitch may be seen in the

Table 8.1: Properties of the beam steered to 45 ° for a range of array pitches

Pitch (mm)	Relative Delay (μs)	Main Beam FWHM (degrees)	Side Lobe Centre (degrees)	Mean Side Lobe (arb. units)
1.15	2.37	54.7	-59.2	0.29
1.25	2.58	50.4	-55.5	0.33
1.50	3.09	42.6	-25.8	0.39

variation in the side lobes. As the pitch of the array is increased, the mean side lobe amplitude increases, making the side lobes more likely to be an issue in a practical application. Additionally, the angular separation between the main beam and the highest amplitude side lobe decreases from 104.2°, to 70.8°, bringing the side lobe much closer to the main beam, increasing the likelihood of interference with any measurements using such an array. Although the array with a pitch of 1.25 mm does not fulfil the $^{\lambda}/_{2}$ requirement the difference in performance between a pitch of 1.25 mm and 1.15 mm is minimal. As such a pitch of 1.25 mm was selected for the following work as a compromise between good performance and ease of construction.

8.1.2 Simulated Steering Using a Waveguide Array

Further sets of simulations were then conducted based upon the waveguide array with an element pitch of 1.25 mm. The first set of simulations involved producing directivity profiles for the array transducer, with the output steered to a range of angles, shown in figure 8.2. From the summary of the properties of the directivity profiles given in table 8.2, it can be seen that the waveguide array behaves in much the same way as would be expected from a conventional ultrasonic array. As the steering angle is increased, the mean side lobe amplitude increases (shown in figure 8.2 with a horizontal line) and the width of the main beam increases. These

Table 8.2: Simulated Beam profiles For a 1.25 mm pitch array

Angle (degrees)	Relative Delay (μs)	FWHM (degrees)	Mean Side Lobe (arb. units)
0	0.00	28.3	0.10
-10	0.63	29.2	0.12
-20	1.25	32.1	0.17
-30	1.82	38.0	0.22
-45	2.58	50.4	0.33

increases could potentially limit the maximum angle to which the array could be used practically, but this limit should be outside of the angular steering range that would be required for most of the intended applications of the waveguide array.

8.1.3 Crosstalk in a Waveguide Array

The current strip waveguide design has only air between the individual elements, in some applications it may be beneficial to add some other material between the waveguide strips. This could be in the form of some solid filler which could provide additional robustness to the transducer or a fluid which could provide a more efficient method of transferring heat away from the strips. However, the addition of such a material could negatively impact the operation of the transducer, both by loading the faces of the strip waveguides and increasing crosstalk between the individual elements [129].

To investigate these effects, a series of FE models were conducted. In these models, a single cycle 150 kHz sine wave was applied as a pressure load to the central element in the waveguide array, with 1.25 mm spacing between the elements. The displacement at the front face of each of the waveguides was then recorded, as any crosstalk between adjacent elements would cause a signal to be detected on the non-driven elements. This model was repeated for three filler materials; firstly for air

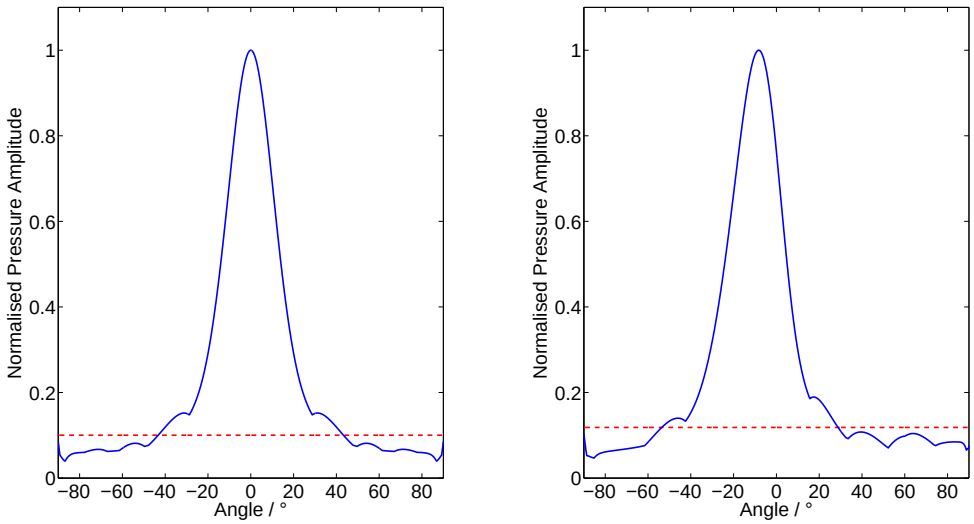

(a)

(b)

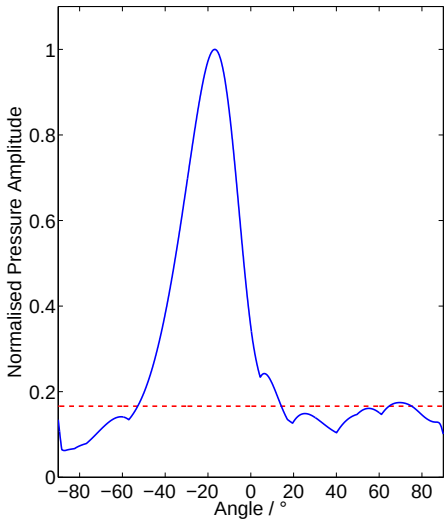

(c)

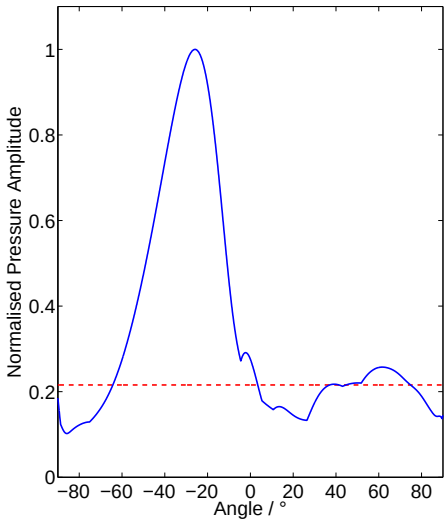

(d)

Figure 8.2: The directivity profile from 2D FE model of the five element strip waveguide array transducer with a pitch of 1.25 mm, steered to (a) 0°, (b) 10°, (c) 20° and (d) 30°.

Table 8.3: The relative amplitude of the displacement on the front face of the five elements in the strip waveguide array transducer (compared to the case of air between the elements), when driven only on element 3, for a range of filler material between the elements.

		Element Number				
		1	2	3	4	5
Filler	Air	< 0.1 %	< 0.1 %	100.0 %	< 0.1 %	< 0.1 %
	Water	3.9 %	8.2 %	92.9 %	8.2 %	3.9 %
	Epoxy	15.1 %	15.4 %	15.5 %	15.4 %	15.1 %

as a reference, then with water between the strips and finally with a hard setting epoxy (Araldite CY1301/HY1300).

For each of the simulations, the maximum amplitude measured on each element was normalised against the maximum amplitude measured on the driven element in the case with air between the strips, with the result given in table 8.3. As expected, having air between the waveguides produces very little crosstalk between the elements, with less than 0.1 % of the amplitude measured on the driven strip present on any of the surrounding strips. Water also gives a reasonable amount of mechanical isolation between the individual elements, with 92.9 % of the amplitude retained on the central element, with less than 9 % on the adjacent element and less than 4 % on the waveguides even further away. In contrast to the fluid filler, the solid filler material (hard setting epoxy), is not an ideal material to use as a filler between the waveguides. The similarities between the solid material of the filler and the waveguides causes the plates and filler material to behave more like a single block of bulk material, allow the incident waves to propagate throughout the whole solid. This leads to a large decrease in the energy that is present at the front face of the waveguide strip, with an amplitude on strip 3 of only 15.4 %. The remainder of the energy is distributed almost evenly across the bundle of waveguides with 15.4 % on the adjacent elements, and 15.1 % on the elements further away. Such a filler

material is clearly far from ideal, but there may be some applications where the additional robustness of a solid filler could be required. In these cases perhaps a filler material such as a low density polymer, filled with a material such as small air-filled glass balloons, could be considered to keep the crosstalk levels minimal. However, the material selection would again be limited by many of the constraints discussed in chapter 7. Having purely a fluid between the waveguide strips is clearly not a practical when constructing a physical prototype, as some supporting structure will be required to hold the strips in place. Ideally, this structure would make minimal contact with the surface of the waveguide strips to limit any coupling between them, using a spacer such as a thin wire, making a line contact with the strip.

8.1.4 Cylindrical Piezoelectric Elements

Traditional piezoelectric transducer arrays are constructed by mechanically dicing a block of piezoelectric material of a thickness which corresponds to the desired frequency, in order to form the individual elements. For low frequency arrays this method can pose some issues, as a typical PZT material with a through thickness mode at 150 kHz will typically be of the order of 10 mm thick, compared to the sub-millimetre thicknesses which relate to the high frequencies commonly found in NDT imaging and medical arrays. Dicing such a thick material can be difficult. In an attempt to avoid this issue and simplify the manufacture of such an array, an alternative method of driving the waveguide elements was investigated, using discrete piezoelectric elements.

Rather than using a single, diced, piezoelectric, each waveguide element in the array would instead be driven using a separate cylindrical piezoelectric element. The cylindrical element would be positioned such that it is aligned tangentially to the end of the waveguide strip, forming a line contact with the 1 mm x 10 mm face of the waveguide, as shown in figure 8.3. The piezoelectric element would then be excited in the thickness mode, generating ultrasonic waves in the waveguide with

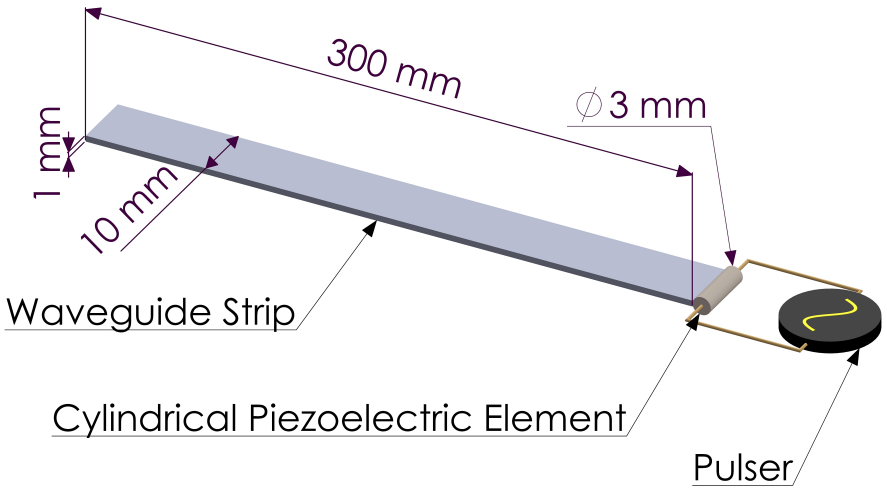

Figure 8.3: A schematic diagram of the individual elements in the strip array, consisting of a stainless steel waveguide strip and a cylindrical piezoelectric element.

the resulting radial motion of the piezoelectric rod.

A FE simulation was carried out to allow the use of a cylindrical piezoelectric element to be compared to standard a thickness mode piezoelectric element. In the first of the models, a stainless steel waveguide (1 mm x 10 mm 300 mm) was driven with a block of PZT5H, with the same cross-section as the waveguide and a thickness of 9 mm mounted at one end. In this model the direction of polarisation of the piezoelectric element is aligned with the length of the strip, giving an optimal geometry for generating ultrasonic waves in the waveguide strip to use as a reference. In the second model, an identical waveguide strip was driven by a 3 mm diameter, 10 mm length PZT5H cylinder, aligned as shown in figure 8.3. The two types of piezoelectric elements were designed such that they have a resonance which occurs around 150 kHz. These elements were driven with identical input voltages (a single cycle sine wave with a frequency of 150 kHz) and the displacement of the front face

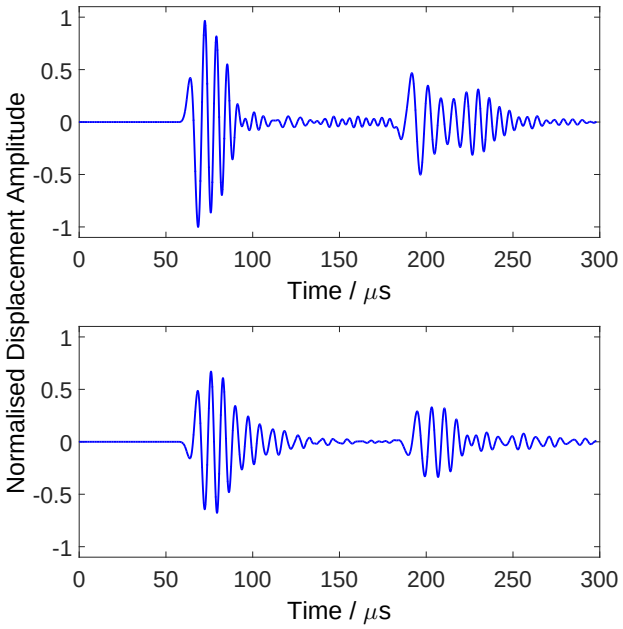

Figure 8.4: The displacement of the front face of the waveguide strip, driven with a thickness mode of a piezoelectric element, top, and the radial displacement of a cylindrical piezoelectric element, bottom.

was recorded. These displacement measurements are shown in figure 8.4, with the displacement from the strip driven by the through thickness PZT shown at the top, and the strip with the cylindrical PZT at the bottom.

The amplitudes in figure 8.4 are normalised relative to the amplitude of the maximum displacement measured on the waveguide driven with the standard through thickness piezoelectric element to assist in comparing the data. Clearly the use of the cylindrical piezoelectric element changes the shape of the transmitted pulse, with a longer, decaying, tail on the wave packet. However, the amplitude of both of the signals remain comparable, with approximately two thirds of the maximum amplitude retained when the waveguide is driven with a radial motion of the cylindrical PZT. The frequency content of the first wave packet of each of the two signals can be seen in figure 8.5. From this figure it can be seen that when driven using the cylindrical PZT the bandwidth of the transducer is reduced, with the

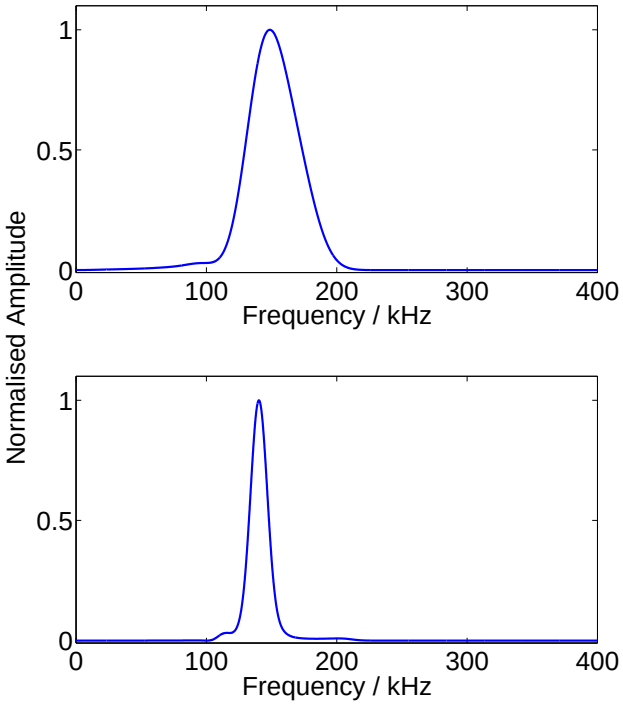

Figure 8.5: The frequency content of the displacement signals when the strip waveguide is driven with a thickness mode piezoelectric element, top, and when driven with the radial motion of a cylindrical piezoelectric element, bottom.

FWHM decreasing from approximately 44 kHz to 15 kHz, with a slight shift in the centre frequency, to 140 kHz. These effects, along with the reduction in amplitude should not pose an issue in a practical application. The loss of amplitude could be offset by driving the PZT with a higher voltage, which is often limited as a safety precaution. For some fluids, such as natural gas, the voltage driving a transducer is often kept low to reduce the ignition risk. However, with the addition of the waveguide strips this voltage would be much further from the fluid, reducing the risk of ignition, and potentially allowing the use of higher driving voltages. Additionally, the loss of bandwidth should not effect the operation of the transducer in most circumstances. The main advantage of this method of driving the transducer in this manner is the relative ease of manufacture and the increased electrical isolation

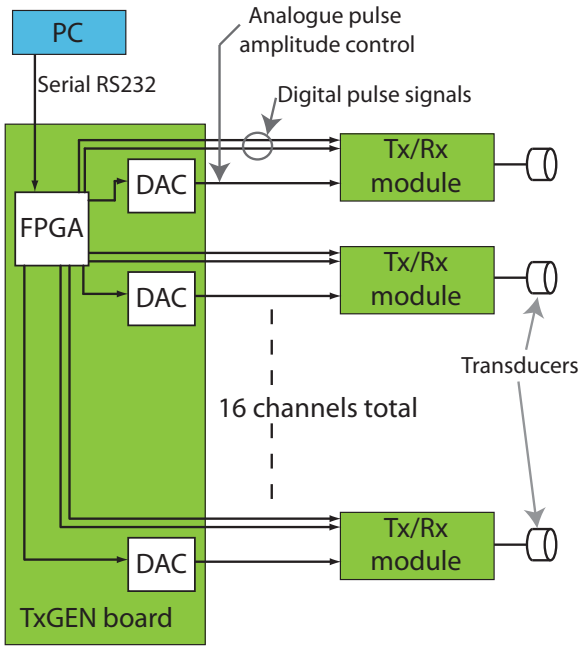

Figure 8.6: A simplified block diagram showing the operation of the LF-PAC. A PC is used to program the waveform generated by the FPGA on the TxGEN board. The FPGA has 16 channels of output. Each of these channels includes a pair of differential signals and a separate analogue voltage signal.

between the individual elements, which is beneficial for array operation.

8.2 Low Frequency Phased Array Electronics

To experimentally confirm the findings of the FE modelling, a custom low frequency phased array controller (LF-PAC) had to be designed and constructed. Phased array transducers, as introduced in chapter 3, are commonly used in medical and NDT applications. However, such applications generally require frequencies much greater than the 150 kHz used in this work and are designed to radiate into target materials with sound speeds greater than that of air. As a result of this, the commercially available phased array controllers are not optimised for driving low frequency transducers or for generating suitably large delays for many air coupled applications. As such, the LF-PAC was designed to allow the investigation of low frequency phased array phenomenon at frequencies between 30 kHz and 250 kHz; a range commonly

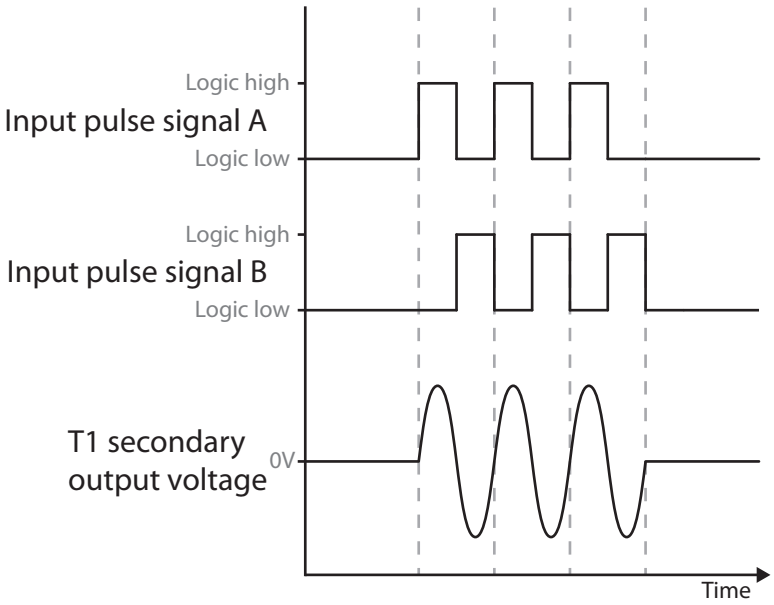

Figure 8.7: Digital differential signalling and transformer secondary output voltage.

used in industrial applications such as ultrasonic flow measurement.

The LF-PAC consists of sixteen parallel transmitter/receiver channels (Tx/Rx modules), and a separate signal generation board (TxGen). A block diagram of the LF-PAC is given in figure 8.6. These individual transmitter/receiver channels are based upon a commercially available pulser-receiver board designed for air coupled applications (T1 Transceiver Module, Airmar Technology Corporation). This design has very limited options in terms of driving frequency and transmit voltage, as these are set using mechanical jumpers on mounted on the board. Additionally, the original board has large a footprint (76 mm x 76 mm), which would make it difficult to assemble into a phased array controller with multiple channels. For the modified Tx/Rx modules it was desirable to significantly reduce the size of the board and allow a much greater control over the emitted signal (in terms of frequency, amplitude and number of cycles).

The heart of the TxGen board is a field programmable gate array (FPGA) which both generates the signals for each of the Tx/Rx channels as well as the amplitude through sets of three outputs for each of the channels, programmed via a

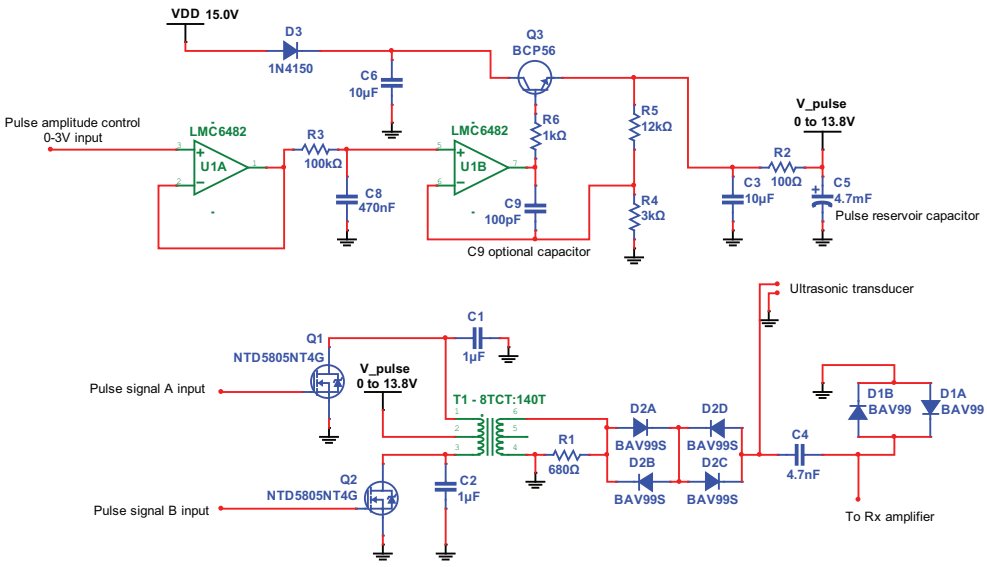

Figure 8.8: Transducer voltage generation circuit. The output pulse amplitude is controlled using the 0-3 V analogue signal from the TxGen board, which sets the voltage of the 4700 uF reservoir capacitor. The pulse signals A and B switch on alternatively during a pulse, which generates an alternating field at the primary coil of the transformer T1. T1 steps up the input voltage to give a high voltage signal to the transducer.

RS232 connection to a PC, where the delays, amplitudes and number of sine cycles may be set separately for each individual element along with a single transmit frequency. The Tx modules require three inputs to generate the output waveform, a pair of digital inputs which set the pulse shape and delay, and a single analogue input to control the amplitude of the output. An example of the digital inputs are given in figure 8.7. To form the output signal shape, the two digital inputs are subtracted from one another, giving a reduction in electrical noise in the signal as it is expected that any external source of noise will affect both of the inputs in a similar way and as such this electrical noise should be cancelled when the signals are subtracted.

The Tx module then converts the three input voltages into signal suitable for driving an ultrasonic transducer via a step up transformer, as shown in the circuit diagram given in figure 8.8. The primary coil, shown in the bottom of the circuit

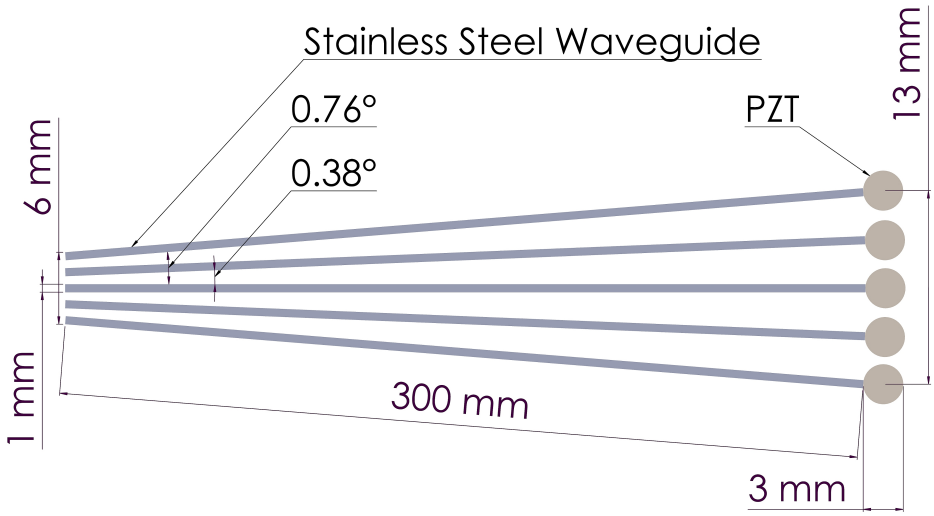

Figure 8.9: A schematic diagram showing the geometry of the array with the waveguide strips positioned at an angle to one another to allow for the diameter of the cylindrical piezoelectric elements.

is connected to the digital outputs from the TXGen board, causing them to be switched on alternately. However, the primary coil is also centre tapped, connecting to the voltage V_{pulse}. This voltage is the output form the top half of the circuit diagram which is driven by the analogue output from the TxGen board, allowing the voltage to be set. The voltage V_{pulse} can be varied between 0 V and approximately 15 V, which can allow a large voltage to be generated on the secondary coil, suitable for driving an ultrasonic transducer.

8.3 Prototype Waveguide Array Transducer

8.3.1 Prototype Geometry

As it has been shown in the FE modelling that an array pitch of 1.25 mm is suitable for the waveguide array, this was used in the prototype transducer. However, due to the 3 mm diameter of the cylindrical piezoelectric elements used to drive each of the waveguide strips, it would not be possible to have an array with the desired

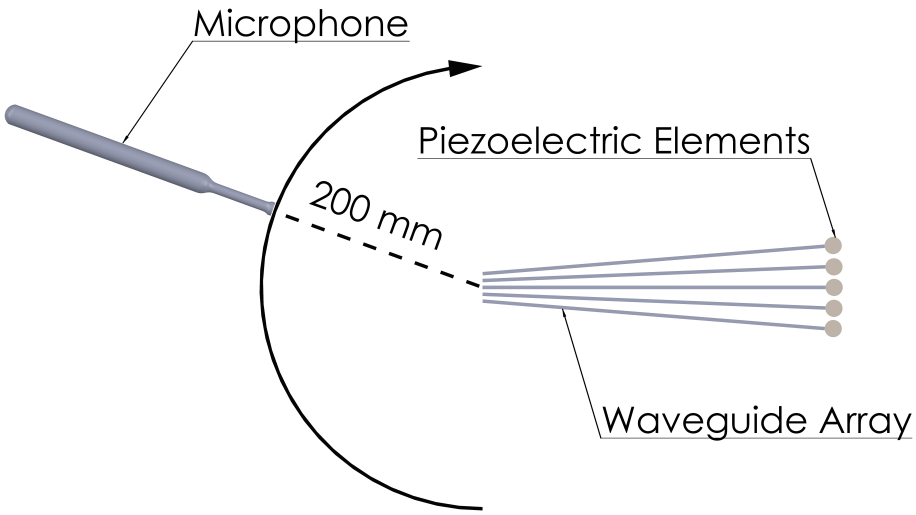

Figure 8.10: A schematic diagram of the experimental set up used to measure the directivity of the strip waveguide array transducer. The five strip array was fixed whilst a wideband microphone rotated about the radiating face of the strip waveguide array at a distance of 200 mm.

pitch and simultaneously use these piezoelectric elements if the strips were to remain parallel. To allow the correct array pitch to be retained at the radiating face of the array the strips were instead arranged such that each of the strips was at a small angle relative to the adjacent element, as shown in figure 8.9. Though the addition of this angle between the waveguide strips would cause them to have a slight angle with respect to one another the effect of this on the emitted waves should be minimal as angles of the strips are so small and as such any variation will be smaller than the manufacturing tolerances of the waveguide strips.

8.3.2 Electronic Steering

In order to assess the practical feasibility of steering the output from the waveguide array, the prototype transducer was fixed to a rail such that a wideband microphone (Brüel & Kjær 4138-A-015) could be rotated about the radiating face at a distance of 200 mm in a 180° arc, as shown in figure 8.10. The piezoelectric elements were

Table 8.4: Statistics derived from the field profile measurements of the strip waveguide array transducer steered to a range of angles.

Angle (degrees)	Relative Delay (μs)	FWHM (degrees)	Mean Side Lobe
0	0.00	25.3	0.24
10	0.63	25.0	0.19
20	1.25	25.9	0.19
30	1.82	29.5	0.23
-45	2.58	35.5	0.36

then driven using a five cycle sine wave pulse with a frequency of 150 kHz and variable delays using the LF-PAC.

The first measurement was taken with no delays on the any of the elements, corresponding to an angle of 0°. Measurements of the radiated pressure were made with the microphone at 2° increments from -90° to 90°. The directivity of the transducer was then plotted by windowing the first wavepacket, to isolate it from the following reverberations, from inside the waveguide strips, and measuring the maximum pressure in this region. The resulting field profile was then normalised to ease comparison between the amplitude of the main beam and the side lobes between the steering measurements.

From the obtained directivity profile, shown in figure 8.11(a), it can be seen that, much like the FE modelling, the majority of the transmitted energy radiated at an angle of 0°, with low side lobe levels. Though the mean side lobe amplitude level is much higher in the experimental data than was observed in the FE models. However, the mean side lobe amplitude is still significantly below that of the main beam, as such these side lobes should not cause issues. Additionally it was found that the experimentally measured directivity profile has a slightly narrower beam, with a FWHM of 25.3°, rather than the 28.3° seen in the FE model.

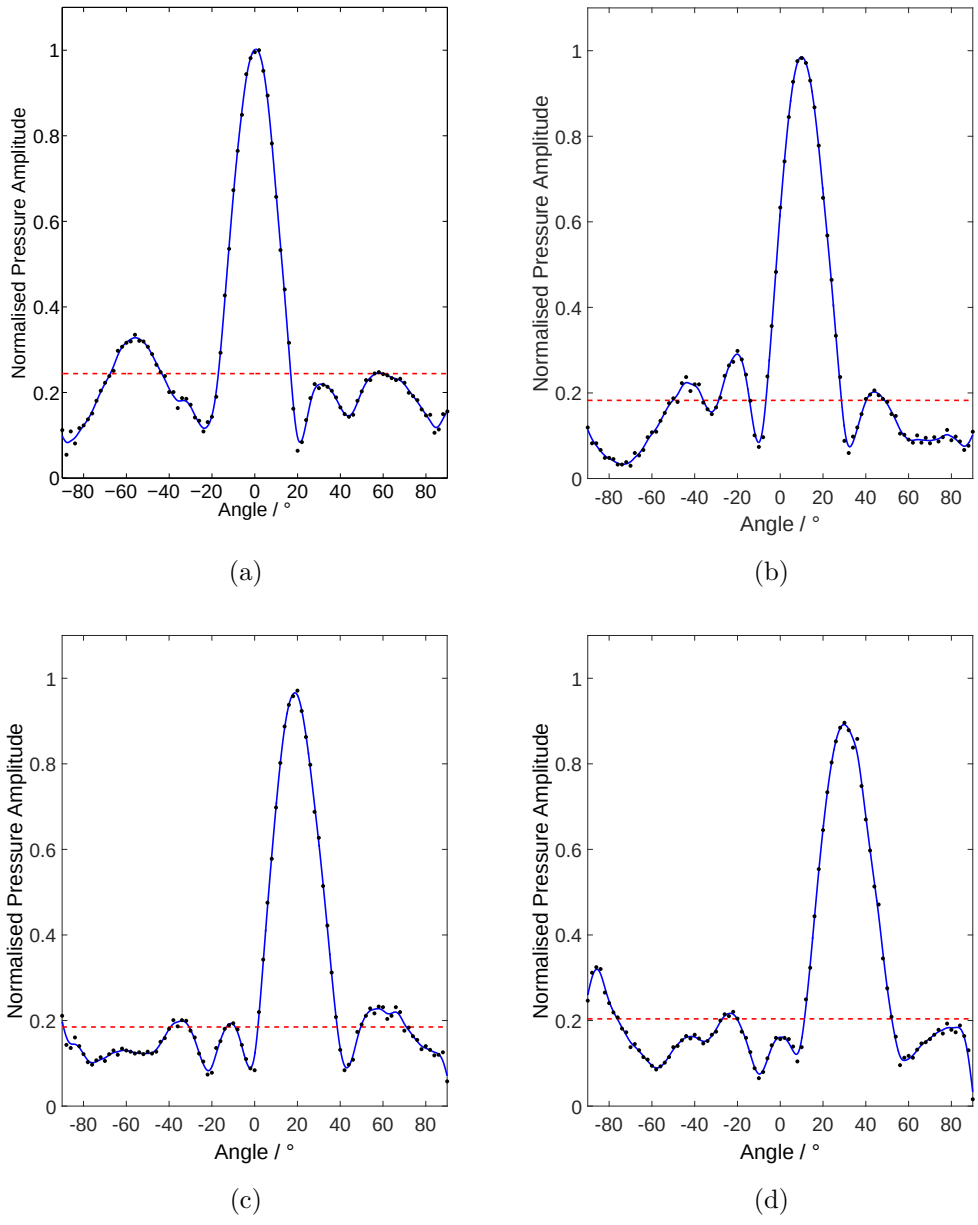

Figure 8.11: The experimentally measured directivity profile of the strip waveguide array transducer electronically steered to (a) 0°, (b) 10°, (c) 20° and (d) 30° respectively.

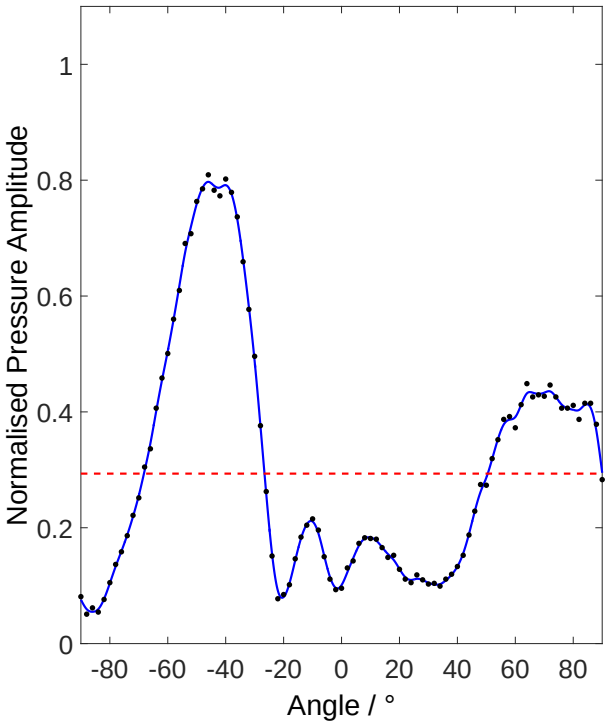

Figure 8.12: The directivity profile for the five element strip waveguide array transducer electronically steered to 45°.

As the 0° measurement gave the expected result, delays were calculated corresponding to the angles investigated in the FE modelling: 10°, 20° and 30°. The directivity measurements obtained for each of these steering angles are also given in figure 8.11, with a summary of many of the important characteristics of the profiles given in table 8.4. It can be seen from table 8.4 that the array performs as desired and is capable of steering the output energy to the correct angle. Much like the 0° case, it was found that the beam width was consistently smaller than was predicted by the FE modelling. In addition, the mean side lobe amplitude is also larger, though at higher angles the difference between the measured amplitude and the simulated amplitude is significantly smaller, as the mean side lobe amplitude is approximately constant for angles up to 30°.

As in the FE modelling, the array was also steered to -45°, to assess the

effect of steering to the maximum of the desired angular range on beam width and side lobes. Again the prototype array demonstrated an ability to steer the beam successfully to the desired angle, however the mean side lobe amplitude is again higher for the experimental measurements. In particular there is one large side lobe with an amplitude of approximately half of the main beam. Although there is a large angular separation between the man beam and the side lobe, approximately 115°, which should limit any effect on the measurement, such a side lobe diverts energy away from the main beam, which could reduce the ability to take measurements in an industrial setting.

8.3.3 Crosstalk in the Prototype Array

In addition the FE model to study the crosstalk in the array experimental crosstalk measurements were taken to confirm the FE results. It may be expected that any crosstalk may be slightly higher in the experimental measurements than was observed in the FE model as there are additional sources of interference between the strips. Firstly there may be electrical crosstalk between the piezoelectric elements, however this should be reduced by the physical separation of the piezoelectric elements. Secondly, there may be mechanical crosstalk between the strip waveguides through the strip mountings. In the FE models the strips do not require any support structure and may be simply positioned in space, however practically there must be some form of support structure through which the waveguide strips could couple to one another. To limit this the strips only were supported in three positions along their length. These mounting points consist of a block with slots for each of the five plates, the edges of these slots are tapered such that they make minimal contact with the surface of the strips, in an attempt to limit crosstalk. The spacing of the slots in each of the three block is varied to allow the array to be aligned such that the array has a 1.25 mm pitch at the radiating front face, and that there is adequate space for the cylindrical piezoelectric elements at the other.

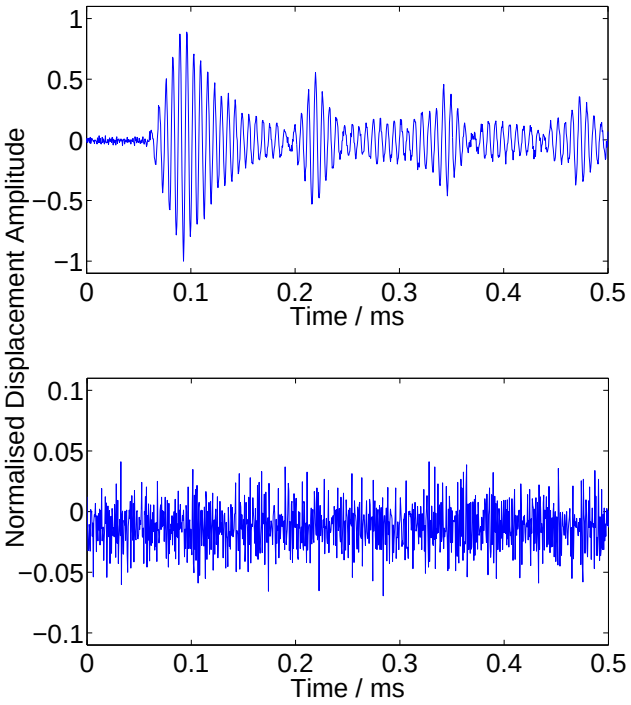

Figure 8.13: The displacement measured at the front face of the driven strip is shown in the upper graph, whilst the lower graph is the measured displacement from the adjacent element in the strip waveguide array transducer.

The experimental crosstalk measurements were obtained by driving a single element in the array with a five cycle, 150 kHz, sine wave signal using the LF-PAC as before and measuring the displacement on the front face of each of the waveguide strips using a Polytec OFV-5000 laser vibrometer.

A typical pair of displacement measurements are shown in figure 8.13, with the displacement of the radiating face of a driven strip given at the top, and the displacement measured on an adjacent, non-driven, strip shown below. From these measurements the waveguide strips appear to be entirely isolated from each other, both mechanically and electrically as there is no apparent signal, in the displacement measurement from the non-driven strip, with an amplitude greater than that of the background noise.

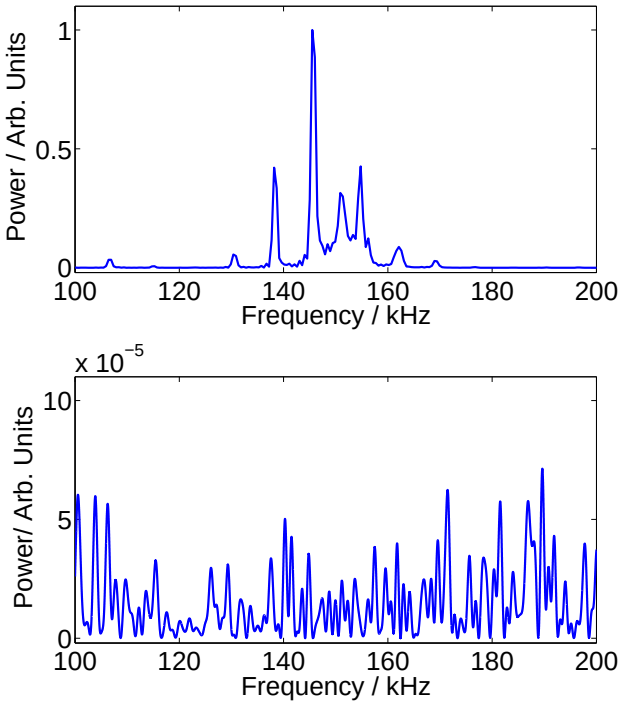

Figure 8.14: The frequency content of the displacement measurements from a driven element, top, and the neighbouring element, bottom.

This can be confirmed by looking at the frequency content of the displacement measurements corresponding to the two strips, shown in figure 8.14. For the driven strip several clear frequency peaks can be seen in the FFT power spectrum in the upper graph in figure 8.14, corresponding to the resonances of the piezoelectric element, around 150 kHz. However, in the lower graph of the frequency spectrum in figure 8.14, for the non-driven element, there is a random distribution of energy across the frequency range, at an amplitude approximately 20,000 times smaller than for the driven strip. If there was some degree of crosstalk between the two elements it would be expected that there would some significant peak in the frequency content around 150 kHz, which is clearly not the case, showing a good degree of isolation between the array elements.

Table 8.5: The measured pressure from the strip waveguide array for a range of active element configurations.

Active Elements					Measured Pressure (Pa)
1					1.05
	2				1.05
		3			1.09
			4		1.04
				5	1.01
	2	3			2.14
	2	3	4		3.10
	2	3	4	5	4.09
1	2	3	4	5	5.02

8.3.4 Array Output

As mentioned previously, the small radiating face of the waveguide strips and the use of cylindrical piezoelectric element both limit the energy which can be transmitted by a single element. However, the use of multiple elements in parallel allows a higher energy transfer, which can be used to offset these factors. This was demonstrated experimentally with the prototype array. This was achieved by placing the microphone 200 mm from the front face of the array at an angle of 0°. Each channel was then calibrated such that a peak to peak maximum pressure of approximately 1 Pa was measured with the microphone when a single element was active, with the values shown in table 8.5.

The central element, labelled 3 in table 8.5, was then activated simultaneously with an adjacent element, such that the effect on the total radiated pressure may be observed. This was then repeated, each time adding an extra active element such that 3, 4 and 5 elements were active simultaneously. From table 8.5 it is clear

that with each additional active element the pressure increases linearly. A small difference may be noted between the measured pressures with multiple elements active simultaneously and the value which would be obtained by summing the pressures for the corresponding measured from the individual elements measured separately. This become increasingly apparent as more channels are activated. This small loss in the potential maximum amplitude results from very small variations in the phase of the signals from the elements, either from the electronics of the pulser or a very small physical misalignment of the radiating faces of the waveguides.

8.4 Conclusions

In this chapter it has been demonstrated, through FE modelling, that a waveguide array consisting of as few as five elements is capable of steering ultrasonic waves to angles up to 45°. This range of steering angles should be broad enough to allow beam correction, which should only require a steering angle of a few degrees, and the investigation of alternate beam paths for applications such as flow measurement. In addition, it has been shown that the side lobes on the beam produced by the prototype array are suitably small over a large range of angles, even though the traditional $^{\lambda}/_{2}$ condition is not fulfilled.

In order to allow experimental confirmation of these FE results, a custom low frequency phased array controller was produced. These custom electronics were required due to the lack of a commercial system capable of supplying the frequencies, delays and voltages required for the investigation of low frequency array phenomena. This phased array controller was then used to drive a prototype strip waveguide array, using geometrical constraints determined by the FE models. The prototype was shown to perform as predicted by the FE model, demonstrating steering up to an angle of 45°. The side lobe amplitudes measured in the experimental directivity profiles were slightly larger than those seen in the FE model, however the amplitude

of the side lobes was still found to be suitably small that they should not cause issues in most applications of such an array. Using this prototype it was also shown experimentally that the strip waveguide array design has minimal crosstalk between the individual elements, with any crosstalk indistinguishable from the background noise of the signal, which agrees well with the FE for waveguide strips, and demonstrated minimal coupling both electrically and through the transducer mountings.

Chapter 9

Conclusions

9.1 Summary

Ultrasonic methods of flow measurement provide a wide range of advantages compared to alternative approaches, with the ability to both measure the flow rate and characterise the flow profile. Currently, ultrasonic flow meters rely on multiple pairs of transducers to interrogate several paths through the fluid flow, allowing the flow profile to be reconstructed. One the limiting factors in the use of ultrasonics is the sensitivity of the piezoelectric elements used to generate the ultrasonic waves to environmental factors, such as elevated temperature.

It has been shown in previous work that the inclusion of a waveguide, which can act as a thermal buffer between the test fluid and the sensitive piezoelectric element, can increase the range of operating conditions and allow new applications. This idea has been further expanded in this thesis by combining the use of waveguides with advances in ultrasonic phased array technology, to produce a transducer that is not only suitable for use in hostile environments, but is also versatile, with the potential to make a range of measurements with a single pair of transducers.

The rectangular cross-section waveguide strips discussed in this thesis have been shown to support guided waves which have some similarity to Lamb waves,

though with additional complexity arising from the finite width of strips. The geometry of the waveguide leads to dispersive behaviour of waves propagating in the waveguide. It has also been shown that by varying the geometry of the strips, for example with the addition of a small taper along the length of the strip, the dispersive behaviour may be modified for operation in a desired frequency range.

Thermal gradients along the length of the waveguide strips have also been shown to cause variations in the way in which an ultrasonic wave will propagate along the waveguide strips, with a general trend of a lower mean wave speed with increasing temperature. The construction of the transducer, with multiple separate waveguide strips has also been shown to cause slight variations between the thermal gradients along each of the individual strips, which should be corrected for using suitable delays, to allow practical application as a phased array transducer.

The addition of a matching layer to the waveguide array transducer has been shown to reduce the impedance mismatch between the stainless steel of the waveguide and the target fluid, allowing an increase in the efficiency with which the transducer can generate ultrasonic waves in a fluid. To allow the use of a matching layer in hostile environments the matching layer materials were selected primarily for their thermal properties. The acoustic properties were then tailored in an effort to achieve better acoustic impedance matching. Though this has been shown to be successful with one of the tested materials, the high levels of loading required to achieve the desired acoustic impedance has also been shown to contribute to an increase in attenuation. This may offset any potential gains resulting from this improved impedance matching. However, even with the unloaded materials, the addition of a matching layer to the radiating face of the transducer has been shown to provide an improvement in the amplitude of the emitted pressure wave.

Finally, it has been shown that using these rectangular cross-section waveguide strips, an array transducer may be constructed that is capable of steering the emitted beam to angles as large as 45°, using only five elements. This was initially

demonstrated using finite element modelling and was then confirmed experimentally using a custom built, phased array controller to apply appropriate delays to each element. Additionally, it has been shown that the use of waveguides allows the construction of an array that approximately satisfies the $^{\lambda}/_{2}$ requirement for the suppression of side lobes; a condition that ordinarily is difficult to meet in the low frequency regime.

9.2 Suggested Further Work

In this thesis the transducer design has been investigated and discussed, and the clear continuation would involve the assessment of the transducer capabilities in a practical application. This could involve testing the transducer in a flow loop, allowing the array transducer to be calibrated using traditional traditional flow meters. As part of this work, a suitable method of signal processing would need to be studied and optimised for this transducer design. The additional complexity of the transmitted signal, resulting from both the propagation within the waveguides and the reverberations may cause difficulties for standard processing methods. After this initial calibration, further experiments could be conducted in an industrial setting over a longer time scale, where the transducer can be exposed to the hostile environments in which it was designed to operate.This would allow for any degradation in the performance of the transducer over time to be monitored as well as providing an opportunity to determine the capability of the transducer to correct for these effects using the additional flexibility provide by the array design.

Another area where there is potential for further development is the matching layer. The loaded materials suggested here are suitable for a wide range of applications. However, these tungsten loaded matching layer materials are not suitable for temperatures greater than 200 °C, which may prevent the usage of these matching layers in some applications. To increase this operational range, alternative matching

layer materials could be investigated. Such materials may include ceramics, which can be designed to withstand much higher temperatures than polymer based materials, or even some type of metallic matching layer. These materials would allow the increased efficiency, offered by the inclusion of a matching layer into the transducer design to be retained, though it is not necessary for the operation of the transducer.

The transducer design may also be further developed by the addition of a second dimension to the array. Such an array may use either square or circular cross-section waveguides each driven with a separate piezoelectric element. This design would allow steering in an additional plane allowing even more paths to be interrogated using a single pair of transducers in a flow metering application, further increasing the versatility of the transducer. Another interesting possibility with a two-dimensional array would be the ability to shape the front face such that it conforms to the inner radius of the pipe. This would essentially remove any effect that the presence of the transducers would have on the fluid flow, though the calculation of the delays that would be required to steer the beam emitted from such a transducer would be much more complex. An additional issue with a two-dimensional array, that would require further study, are the thermal effects. The presence of a greater number of individual waveguides and the increased variability in layout of the array elements may lead to greater variation between the thermal gradients along each waveguide. This variation would need to be studied to allow appropriate compensation to be carried out.

Appendices

Appendix A

Lamb Wave Derivations

One of the most common methods used for deriving the equations describing Lamb waves involves the use of potentials. In this form, equations 4.10 and 4.11 may be rewritten as:

$$\frac{\partial^2 \phi}{\partial x_1^2} + \frac{\partial^2 \phi}{\partial x_3^2} = \frac{1}{c_L^2} \frac{\partial^2 \phi}{\partial t^2}, \tag{A.1}$$

$$\frac{\partial^2 \psi}{\partial x_1^2} + \frac{\partial^2 \psi}{\partial x_3^2} = \frac{1}{c_T^2} \frac{\partial^2 \phi}{\partial t^2}. \tag{A.2}$$

Assuming plane strain, these equations allow the displacements and stresses be rewritten as:

$$u_1 = \frac{\partial \phi}{\partial x_1} + \frac{\partial \psi}{\partial x_3}, \tag{A.3a}$$

$$u_2 = 0, \tag{A.3b}$$

$$u_3 = \frac{\partial \phi}{\partial x_3} - \frac{\partial \psi}{\partial x_1}, \tag{A.3c}$$

$$\sigma_{31} = \mu \left(\frac{\partial u_3}{\partial x_1} + \frac{\partial u_1}{\partial x_3} \right) = \mu \left(\frac{\partial^2 \phi}{\partial x_1 \partial x_3} - \frac{\partial^2 \psi}{\partial x_1^2} + \frac{\partial^2 \psi}{\partial x_3^2} \right), \tag{A.4a}$$

$$\begin{aligned}\sigma_{33} &= \lambda\left(\frac{\partial u_1}{\partial x_1}+\frac{\partial u_3}{\partial x_3}\right)+2\mu\frac{\partial u_3}{\partial x_3} \\ &= \lambda\left(\frac{\partial^2\phi}{\partial x_1^2}+\frac{\partial^2\phi}{\partial x_3^2}\right)+2\mu\left(\frac{\partial^2\phi}{\partial x_3^2}-\frac{\partial^2\psi}{\partial x_1 x_3}\right).\end{aligned} \tag{A.4b}$$

We assume solutions to these sets of equations of the form:

$$\phi = \Phi(x_3)\exp[i(kx_1-\omega t)], \tag{A.5}$$

$$\psi = \Psi(x_3)\exp[i(kx_1-\omega t)]. \tag{A.6}$$

Solutions of this form correspond to propagating waves travelling along the x_1 direction while allowing standing waves in the x_3 direction, i.e. travelling along the arbitrary length dimension of the plate. Substituting these solutions into the potential forms of the wave equations given by equations A.1 and A.2, show that suitable solutions for the functions Φ and Ψ are given by:

$$\Phi(x_3) = A_1\sin(px_3)+A_2\cos(px_3), \tag{A.7}$$

$$\Psi(x_3) = B_1\sin(qx_3)+B_2\cos(qx_3), \tag{A.8}$$

where

$$p^2 = \frac{\omega^2}{c_L^2}-k^2, \tag{A.9}$$

$$q^2 = \frac{\omega^2}{c_T^2}-k^2. \tag{A.10}$$

These solutions may be substituted into equations A.3 and A.4 which allows the following to be obtained:

$$u_1 = \left(ik\Phi+\frac{d\Psi}{dx_3}\right)\exp[(ik_1\omega t)], \tag{A.11}$$

$$u_3 = \left(\frac{d\Phi}{dx_3}-ik\Psi\right)\exp[(ik_1\omega t)], \tag{A.12}$$

$$\sigma_{33} = \left[\lambda\left(-k^2\Phi + \frac{d^2\Phi}{dx_3^2}\right) + 2\mu\left(\frac{d^2\Phi}{dx_3^2} - ik\frac{d\Psi}{dx_3}\right)\right]\exp[(ik_1\omega t)], \tag{A.13}$$

$$\sigma_{31} = \mu\left(2ik\frac{d\Phi}{d_3} + k^2\Psi + \frac{d^2\Psi}{dx_3^2}\right)\exp[(ik_1\omega t)]. \tag{A.14}$$

Where μ and λ are the Lamé parameters. The term, $\exp[(ik_1\omega t)]$, which is present in all of these solutions will generally be omitted from further results to simplify the expressions. These expressions can be further divided into symmetric and antisymmetric solutions about the $x_3 = 0$ plane. For the symmetric solutions, it is required that the displacement u_1 contains only symmetric functions, i.e. cosine functions, conversely the displacement u_3 should contain only antisymmetric functions, i.e. sine functions. The reverse is true for the antisymmetric solutions, both sets may be summarised as follows, for symmetric modes:

$$\begin{aligned}
\Phi &= A_2\cos(px_3),\\
\Psi &= B_1\sin(qx_3),\\
u_1 &= ikA_2\cos(px_3) + qB_1\cos(qx_3),\\
u_3 &= -pA_2\sin(px_3) - ikB_1\sin(qx_3),\\
\sigma_{31} &= \mu[-2ikpA_2\sin(px_3) + (k^2 - q^2)B_1\sin(qx_3)],\\
\sigma_{33} &= -\lambda(k^2 + p^2)A_2\cos(px_3) - 2\mu[p^2A_2\cos(px_3) + ikqB_1\cos(qx_3)],
\end{aligned} \tag{A.15}$$

and for antisymmetric modes:

$$\begin{aligned}
\Phi &= A_1\sin(px_3),\\
\Psi &= B_2\cos(qx_3),\\
u_1 &= ikA_1\sin(px_3) - qB_2\sin(qx_3),\\
u_3 &= pA_1\cos(px_3) - ikB_2\cos(qx_3),\\
\sigma_{31} &= \mu[2ikpA_1\cos(px_3) + (k^2 - q^2)B_2\cos(qx_3)],\\
\sigma_{33} &= -\lambda(k^2 + p^2)A_1\sin(px_3) - 2\mu[p^2A_1\sin(px_3) - ikqB_2\sin(qx_3)],
\end{aligned} \tag{A.16}$$

The values of the four unknown constants A_1, A_2,B_1 and B_2 may then be calculated by applying the boundary conditions, stated previously and summarised as:

$$\sigma_{31} = \sigma_{33} \equiv 0 \quad \text{at} \quad x_3 = \pm h. \tag{A.17}$$

This gives a set of homogeneous equations which can then be solved to find the values of these constants. For the symmetric case this can be done in the following way:

$$\begin{bmatrix} -2ikp\sin(px_3) & (k^2-q^2)\sin(qx_3) \\ (\lambda k^2 + \lambda p^2 + 2\mu p^2)\cos(px_3) & 2\mu ikq\cos(qx_3) \end{bmatrix} \begin{bmatrix} A_2 \\ B_1 \end{bmatrix} = \begin{bmatrix} 0 \\ 0 \end{bmatrix} \tag{A.18}$$

For the solutions to be non-trivial, it is required that the determinant of the coefficient matrix be zero. This determinant gives us an expression which relates the frequency and wavenumber of the wave mode, a dispersion relation. After a little manipulation this can be shown to have the form:

$$\frac{\tan(qh)}{\tan(ph)} = -\frac{4k^2pq}{(q^2-k^2)^2}. \tag{A.19}$$

Similarly, for the antisymmetric solutions a similar dispersion relation may be obtained:

$$\frac{\tan(qh)}{\tan(ph)} = -\frac{(q^2-k^2)^2}{4k^2pq}. \tag{A.20}$$

These are the Rayleigh-Lamb equations which may be used to determine how a wave of a particular frequency will propagate in a thin plate. Though the form of these equations seems relatively simple, an analytical solution is not possible and thus numerical methods must be employed to obtain solutions.

Bibliography

[1] J. F. W. Bell, "The velocity of sound in metals at high temperatures," *Philosophical Magazine*, vol. 2, no. 21, pp. 1113–1120, October 1957.

[2] C.-K. Jen, J.-G. Legoux, and L. Parent, "Experimental evaluation of clad metallic buffer rods for high temperature ultrasonic measurements," *NDT & E International*, vol. 33, no. 3, pp. 145 – 153, April 2000.

[3] L. Y. Tu, J. N. Brennan, and J. A. Sauer, "Dispersion of ultrasonic pulse velocity in cylindrical rods," *The Journal of the Acoustical Society of America*, vol. 27, no. 3, pp. 550–555, May 1955.

[4] A. Sather, "Ultrasonic buffer rod technique for the high temperature measurement of the elastic moduli of short specimens," *The Journal of the Acoustical Society of America*, vol. 43, no. 6, pp. 1291–1294, June 1968.

[5] V. Prasad, K. Balasubramaniam, E. Kannan, and K. Geisinger, "Viscosity measurements of melts at high temperatures using ultrasonic guided waves," *Journal of Materials Processing Technology*, vol. 207, no. 13, pp. 315 – 320, October 2008.

[6] Y. Liu, L. Lynnworth, and M. A. Zimmerman, "Buffer waveguides for flow measurement in hot fluids," *Ultrasonics*, vol. 36, no. 1-5, pp. 305–315, February 1998.

[7] Y. Liu and L. C. Lynnworth, "Ultrasonic path bundle and systems," U.S. Patent 6,343,511, February 5, 2002.

[8] G. G. Sherratt and E. Griffiths, "The determination of the specific heat of gases at high temperatures by the sound velocity method. I - Carbon monoxide," *Proceedings of the Royal Society London A*, vol. 147, no. 861, pp. 292–308, November 1934.

[9] A. M. Heijnsdijk and J. M. van Klooster, "Ultrasonic waveguide," U.S. Patent 6,400,648, June 4, 2002.

[10] L. C. Lynnworth, G. Jossinet, and E. Chrifi, "300 °C clamp-on ultrasonic transducers for measuring water flow and level," in *Proceedings of 1996 IEEE International Ultrasonics Symposium*, vol. 1, November 1996, pp. 407 – 412.

[11] B. Dean and L. Lynnworth, "Hockey stick developments extend range, improve accuracy of clamp-on flow measurements," in *Ultrasonics Symposium, 1999. Proceedings. 1999 IEEE*, vol. 1, October 1999, pp. 761–765.

[12] L. C. Lynnworth, *Ultrasonic Measurement for Process Control: Theory, Techniques, Applications.* London: Academic Press, Inc, 1989.

[13] R. C. Baker, *Flow measurement handbook : industrial designs, operating principles, performance, and applications.* Cambridge: Cambridge University Press, 2000.

[14] R. W. Miller, *Flow measurement engineering handbook.* New York: McGraw-Hill, 1996.

[15] S. Pirouzpanah, M. Çevik, and G. L. Morrison, "Multiphase flow measurements using coupled slotted orifice plate and swirl flow meter," *Flow Measurement and Instrumentation*, vol. 40, no. 0, pp. 157 – 161, December 2014.

[16] R. C. Baker, "Response of bulk flowmeters to multiphase flows," *Journal of Mechanical Engineering Science*, vol. 205, no. 4, pp. 217–229, July 1991.

[17] R. Pal, "Pipeline flow of unstable and surfactant-stabilized emulsions," *AIChE Journal*, vol. 39, no. 11, November 1993.

[18] R. C. Baker, "Turbine and related flowmeters: I. industrial practice," *Flow Measurement and Instrumentation*, vol. 2, no. 3, pp. 147 – 161, July 1991.

[19] R. C. Baker, "Turbine flowmeters: II. theoretical and experimental published information," *Flow Measurement and Instrumentation*, vol. 4, no. 3, pp. 123 – 144, December 1993.

[20] L. F. Olsen, *Introduction to liquid flow metering and calibration of liquid flowmeters*. Washington D.C.: National Bureau of Standards, 1974.

[21] J. D. Place and R. Maurer, "A non-invasive fibre optic pick-up for a turbine flowmeter," in *Conference on Fibre Optics 86*, October 1986, pp. 226–232.

[22] H. Tsukamoto and S. P. Hutton, "Theoretical prediction of meter factor for a helical turbine flowmeter," in *Conference of Fluid Control and Measurement*, Spetember 1985.

[23] R. E. Thompson and J. Grey, "Turbine flowmeter performance model," *Journal of Fluids Engineering*, vol. 92, no. 4, pp. 712–722, December 1970.

[24] P. Jepson and P. G. Bean, "Effect of upstream velocity profiles on turbine flowmeter registration," *Journal of Mechanical Engineering Science*, vol. 11, no. 5, pp. 503–510, October 1969.

[25] R. C. Baker, "Coriolis flowmeters: industrial practice and published information," *Flow Measurement and Instrumentation*, vol. 5, no. 4, pp. 229 – 246, October 1994.

[26] M. Anklin, W. Drahm, and A. Rieder, "Coriolis mass flowmeters: Overview of the current state of the art and latest research," *Flow Measurement and Instrumentation*, vol. 17, no. 6, pp. 317 – 323, December 2006.

[27] T. M. Agarwal, A. K., "New micro motion mass flow meters." *Energy progress*, vol. 4, no. 4, pp. 221–224, December 1984.

[28] F. Cascetta, G. Cignolo, R. Goria, G. Martini, A. Rivetti, and P. Vigo, "Experimental intercomparison of coriolis mass flowmeters," *Transactions of the Institute of Measurement and Control*, vol. 14, no. 2, pp. 99–107, April 1992.

[29] A. E. Wahed and J. Sproston, "The influence of shedder shape on the performance of the electrostatic vortex flowmeter," *Flow Measurement and Instrumentation*, vol. 2, no. 3, pp. 169 – 179, July 1991.

[30] H. Yamasaki, "Progress in hydrodynamic oscillator type flowmeters," *Flow Measurement and Instrumentation*, vol. 4, no. 4, pp. 241 – 247, October 1993.

[31] E. J. Williams, "The induction of electromotive forces in a moving liquid by a magnetic field, and its application to an investigation of the flow of liquids," *Proceedings of the Physical Society*, vol. 42, no. 5, p. 466, August 1930.

[32] A. Kolin, "An electromagnetic flowmeter. principle of the method and its application to bloodflow measurements," *Experimental Biology and Medicine*, vol. 35, no. 1, pp. 53–56, October 1936.

[33] A. Kolin, "An A.C. induction flow meter for measurement of blood flow in intact blood vessels," *Experimental Biology and Medicine*, vol. 46, no. 2, pp. 235–239, February 1941.

[34] N. V. Tobi, "Detector for an induction liquid flow meter," G.B. Patent 726,271, March 16, 1955.

[35] D. Ginesi and C. Annarummo, "Application and installation guidelines for volumetric and mass flowmeters," *ISA Transactions*, vol. 33, no. 1, pp. 61 – 72, May 1994.

[36] Emerson Process Management, "Magnetic flowmeter material selection guide," April 2013, 00816-0100-3033 datasheet.

[37] M. Sanderson and H. Yeung, "Guidelines for the use of ultrasonic non-invasive metering techniques," *Flow Measurement and Instrumentation*, vol. 13, no. 4, pp. 125 – 142, August 2002.

[38] J. G. Drenthen and G. de Boer, "The manufacturing of ultrasonic gas flow meters," *Flow Measurement and Instrumentation*, vol. 12, no. 2, pp. 89–99, April 2001.

[39] J. Kritz, *Instruments and Automation*, vol. 28, pp. 1912–1913, November 1955.

[40] S. Kivilis and V. Reshetnikov, *Measurement Techniques*, vol. 8, no. 3, pp. 276–278, March 1965.

[41] R. C. Baker and E. J. Thompson, "A two beam ulrasonic phase-shift flowmeter," in *Conference on Fluid Flow Measurement in the Mid 1970s*, April 1975.

[42] K. Mylvaganam, "High-rangeability ultrasonic gas flowmeter for monitoring flare gas," *Ultrasonics, Ferroelectrics, and Frequency Control, IEEE Transactions on*, vol. 36, no. 2, pp. 144–149, March 1989.

[43] A. Guilbert and M. Sanderson, "The development of curved reflective surfaces for ultrasonic beam redirection in high speed gas flow measurement," *Ultrasonics*, vol. 34, no. 25, pp. 441 – 445, June 1996.

[44] M. Kupnik, P. O'Leary, A. Schroder, and I. Rungger, "Numerical simulation of ultrasonic transit-time flowmeter performance in high temperature gas flows,"

in *Ultrasonics, 2003 IEEE Symposium on*, vol. 2, October 2003, pp. 1354–1359 Vol.2.

[45] M. Kupnik, A. Schroder, and M. Groschl, "Adaptive asymmetric double-path ultrasonic transit-time gas flowmeter," in *Ultrasonics Symposium, 2006. IEEE*, October 2006, pp. 2429–2432.

[46] D. Berlincourt and H. H. A. Krueger, "Properties of Morgan Electro Ceramics ceramics," Morgan Electro Ceramics Technical Publication TP-226.

[47] T. R. Shroud, R. E. Eitel, and C. A. Randall, *Piezoelectric Materials in Devices.* Lausanne: Swiss Federal Institute of Technology, 2002, ch. High performance, high temperature perovskite piezoelectric ceramics.

[48] X. Zhang, Z. Chen, L. Cross, and W. Schulze, "Dielectric and piezoelectric properties of modified lead titanate zirconate ceramics from 4.2 to 300 K," *Journal of Materials Science*, vol. 18, no. 4, pp. 968–972, April 1983.

[49] R. Georges Sabat, B. K. Mukherjee, W. Ren, and G. Yang, "Temperature dependence of the complete material coefficients matrix of soft and hard doped piezoelectric lead zirconate titanate ceramics," *Journal of Applied Physics*, vol. 101, no. 6, p. 064111, March 2007.

[50] B. Yurke, P. Kaminsky, and D. Eigler, "Cryogenic piezoelectric displacement tester," *Cryogenics*, vol. 26, no. 7, pp. 435 – 436, July 1986.

[51] J. D. N. Cheeke, *Fundamental and Applications of Ultrasonic Waves.* London: CRC Press, 2002.

[52] T. L. Szabo, *Diagnostic Ultrasound Imaging: Inside Out.* London: Elsevier Inc., 2004.

[53] D. Ensminger and L. J. Bond, *Ultrasonics Fundamentals, Technologies, and Applications.* London: CRC Press, 2011.

[54] A. Moulson and J. M. Herbert, *Electroceramics : materials, properties, applications.* New York: Wiley, 2003.

[55] B. Jaffe, W. R. Cook, and J. Jaffe, *Piezoelectric Ceramics.* London: Academic Press, 1971.

[56] M. G. Silk, *Ultrasonic Transducers for Nondestructive Testing.* Bristol: Adam Hilger Ltd, 1984.

[57] W. P. Mason, *Electromechanical transducers and wave filters.* New York: D. Van Nostrand Co, 1948.

[58] M. Redwood, "Transient performance of a piezoelectric transducer," *The Journal of the Acoustical Society of America*, vol. 33, no. 4, pp. 527–536, April 1961.

[59] R. Krimholtz, D. Leedom, and G. Matthaei, "New equivalent circuits for elementary piezoelectric transducers," *Electronics Letters*, vol. 6, no. 13, pp. 398–399, June 1970.

[60] G. S. Kino, *Acoustic waves: devices, imaging, and analog signal processing.* New Jersey: Prentice Hall, 2000.

[61] M. Lethiecq, F. Levassort, D. Certon, and L. P. Tran-Huu-Hue, *Piezoelectric and Acoustic Materials for Transducer Applications.* New York: Springer, 2008, ch. Piezoelectric Transducer Design for Medical Diagnosis and NDE.

[62] S. K. Bhargava, *Principles and Practice of Ultrasonography.* Delhi: Jaypee, 2004.

[63] M. Hirao and H. Ogi, *Noncontacting Ultrasonic Measurements.* Boston: Kluwer-Academic, 2003.

[64] J. Morrison, S. Dixon, M. Potter, and X. Jian, "Lift-off compensation for improved accuracy in ultrasonic lamb wave velocity measurements using electromagnetic acoustic transducers (EMATs)," *Ultrasonics*, vol. 44, Supplement, pp. e1401 – e1404, December 2006.

[65] P. Petcher, M. Potter, and S. Dixon, "A new electromagnetic acoustic transducer (EMAT) design for operation on rail," *NDT & E International*, vol. 65, pp. 1 – 7, July 2014.

[66] D. Rueter and T. Morgenstern, "Ultrasound generation with high power and coil only EMAT concepts," *Ultrasonics*, vol. 54, no. 8, pp. 2141 – 2150, 2014.

[67] D. Schindel, D. Hutchins, L. Zou, and M. Sayer, "The design and characterization of micromachined air-coupled capacitance transducers," *Ultrasonics, Ferroelectrics, and Frequency Control, IEEE Transactions on*, vol. 42, no. 1, pp. 42–50, January 1995.

[68] O. Oralkan, A. Ergun, J. Johnson, M. Karaman, U. Demirci, K. Kaviani, T. Lee, and B. Khuri-Yakub, "Capacitive micromachined ultrasonic transducers: next-generation arrays for acoustic imaging?" *Ultrasonics, Ferroelectrics, and Frequency Control, IEEE Transactions on*, vol. 49, no. 11, pp. 1596–1610, November 2002.

[69] B. Bayram, O. Oralkan, A. Ergun, E. Haeggstrom, G. Yaralioglu, and B. Khuri-Yakub, "Capacitive micromachined ultrasonic transducer design for high power transmission," *Ultrasonics, Ferroelectrics, and Frequency Control, IEEE Transactions on*, vol. 52, no. 2, pp. 326–339, February 2005.

[70] A. Buhrdorf, O. Ahrens, and J. Binder, "Capacitive micromachined ultrasonic transducers and their application," in *Ultrasonics Symposium, 2001 IEEE*, vol. 2, October 2001, pp. 933–940.

[71] C. Cheng, E. Chow, X. Jin, S. Ergun, and B. Khuri-Yakub, "An efficient electrical addressing method using through-wafer vias for two-dimensional ultrasonic arrays," in *Ultrasonics Symposium, 2000 IEEE*, vol. 2, October 2000, pp. 1179–1182.

[72] M. W. Sigrist, "Laser generation of acoustic waves in liquids and gases," *Journal of Applied Physics*, vol. 60, no. 7, pp. R83–R122, October 1986.

[73] C. B. Scruby and L. E. Drain, *Laser ultrasonics techniques and applications*. Bristol: IOP Publishing, 1990.

[74] A. McNab and M. J. Campbell, "Ultrasonic phased arrays for nondestructive testing," *NDT International*, vol. 20, no. 6, pp. 333–337, December 1987.

[75] B. W. Drinkwater and P. D. Wilcox, "Ultrasonic arrays for non-destructive evaluation: A review," *NDT & E International*, vol. 39, no. 7, pp. 525–541, October 2006.

[76] L. Azar, Y. Shi, and S. C. Wooh, "Beam focusing behaviour of linear phased arrays," *NDT & E International*, vol. 33, no. 3, pp. 189–198, April 2000.

[77] H. Lu, J. Y.and Zou and J. F. Greenleaf, "Biomedical ultrasound beam forming," *Ultrasound in Medicine and Biology*, vol. 20, no. 5, pp. 403–428, June 1994.

[78] J. H. Lee and S. W. Choi, "A parametric study of ultrasonic beam profiles for a linear phased array transducer," *Ultrasonics, Ferroelectrics, and Frequency Control, IEEE Transactions on*, vol. 47, no. 3, pp. 644–650, May 2000.

[79] D. Turnbull and F. Foster, "Beam steering with pulsed two-dimensional transducer arrays," *Ultrasonics, Ferroelectrics, and Frequency Control, IEEE Transactions on*, vol. 38, no. 4, pp. 320–333, July 1991.

[80] A. McNab and I. Stumpf, "Monolithic phased array for the transmission of ultrasound in NDT ultrasonics," *Ultrasonics*, vol. 24, no. 3, pp. 148 – 155, May 1986.

[81] S. C. Wooh and Y. Shi, "Three-dimensional beam directivity of phase-steered ultrasound," *The Journal of the Acoustical Society of America*, vol. 105, no. 6, pp. 3275–3282, June 1999.

[82] S. C. Wooh and Y. Shi, "Influence of phased array element size on beam steering behavior," *Ultrasonics*, vol. 36, no. 6, pp. 737 – 749, April 1998.

[83] C. Frazier and W. OBrien, "Synthetic aperture techniques with a virtual source element," *IEEE Transactions on Ultrasonics, Ferroelectrics and Frequency Control*, vol. 45, no. 1, pp. 196 – 207, January 1998.

[84] O. V. Ramm and S. Smith, "Beam steering with linear arrays," *IEEE Transactions on Biomedical Engineering*, vol. BME-30, no. 8, pp. 438 – 452, August 1983.

[85] C. A. Youngdahl and W. A. Ellingson, "Development of ultrasonic techniques for remote monitoring of erosive wear in coal-conversion systems," in *1978 Ultrasonics Symposium*, September 1978, pp. 305–310.

[86] C. K. Jen, C. Neron, A. Miri, H. Soda, A. Ohno, and A. McLean, "Fabrication and characterization of continuously cast clad metallic buffer rods," *The Journal of the Acoustical Society of America*, vol. 91, no. 6, pp. 3565–3570, June 1992.

[87] H. Soda, C. K. Jen, G. Motoyasu, S. Okumura, A. Ohno, and A. McLean, "Fabrication and characterisation of aluminium clad aluminiumcopper alloy cored rod," *Materials Science and Technology*, vol. 11, no. 11, pp. 1174–1179, November 1995.

[88] C. K. Jen and J. G. Legoux, "Clad ultrasonic waveguides with reduced trailing echoes," U.S. Patent 5,828,274 A, October 27, 1998.

[89] J. O. Kim, H. H. Bau, Y. Liu, L. C. Lynnworth, S. A. Lynnworth, K. A. Hall, S. A. Jacobson, and J. A. Korba, "Torsional sensor applications in two-phase fluids," *Ultrasonics, Ferroelectrics, and Frequency Control, IEEE Transactions on*, vol. 40, no. 5, pp. 563–576, September 1993.

[90] F. B. Cegla, P. Cawley, J. Allin, and J. Davies, "High-temperature (> 500 °C) wall thickness monitoring using dry-coupled ultrasonic waveguide transducers," *IEEE Transactions on ultrasonics ferroelectrics and frequency control*, vol. 58, no. 1, pp. 156–167, January 2011.

[91] B. A. Auld, *Acoustic Fields and Waves in Solids.* Florida: Krieger Publishing Company, 1990.

[92] J. L. Rose, *Ultrasonic Waves in Solid Media.* Cambridge: Cambridge University Press, 1999.

[93] P. Wilcox, M. Lowe, and P. Cawley, "The effect of dispersion on long-range inspection using ultrasonic guided waves," *NDT & E International*, vol. 34, no. 1, pp. 1 – 9, January 2001.

[94] J. Coulthard, "Ultrasonic cross-correlation flowmeters," *Ultrasonics*, vol. 11, no. 2, pp. 83–88, March 1973.

[95] H. Lamb, "On waves in an elastic plate," *Proceedings of the Royal Society of London A: Mathematical, Physical and Engineering Sciences*, vol. 93, no. 648, pp. 114–128, March 1917.

[96] O. C. Zienkiewicz, *The Finite Element Method: Its Basics and Fundamentals.* London: McGraw-Hill, 1977.

[97] Z. Chen, *The Finite Element Method: Its Fundamentals and Applications in Engineering.* New Jersey: World Scientific., 2011.

[98] G. S. Warren and W. R. Scott, "Numerical dispersion in the finite-element method using triangular edge elements," *Microwave and Optical Technology Letters*, vol. 9, no. 6, pp. 315–319, August 1995.

[99] W. R. Scott, "Errors due to spatial discretization and numerical precision in the finite-element method," *IEEE Transactions on Antennas and Propagation*, vol. 42, no. 11, pp. 1565–1570, November 1994.

[100] G. Wojcik, D. K. Vaughan, N. Abboud, and J. Mould, "Electromechanical modeling using explicit time-domain finite elements," in *Ultrasonics Symposium, 1993 IEEE*, vol. 2, October 1993, pp. 1107–1112.

[101] R. Goldberg, M. Jurgens, D. Mills, C. Henriquez, D. Vaughan, and S. Smith, "Modeling of piezoelectric multilayer ceramics using finite element analysis," *Ultrasonics, Ferroelectrics, and Frequency Control, IEEE Transactions on*, vol. 44, no. 6, pp. 1204–1214, November 1997.

[102] F. B. Cegla, "Energy concentration at the center of large aspect ratio rectangular waveguides at high frequencies," *Journal of the Acoustical Society of America*, vol. 123, no. 6, pp. 4218–4226, June 2008.

[103] T. Hayashi, S. Won-Joon, and J. L. Rose, "Guided wave dispersion curves for a bar with an arbitrary cross-section, a rod and rail example," *Ultrasonics*, vol. 41, no. 3, pp. 175–183, May 2003.

[104] P. Wilcox, M. Evans, O. Diligent, M. Lowe, and P. Cawley, "Dispersion and excitability of guided acoustic waves in isotropic beams with arbitrary cross section," in *AIP Conference Proceedings*, vol. 615, July 2002, pp. 203–210.

[105] D. N. Alleyne and P. Cawley, "A two-dimensional Fourier transform method for the measurement of propagating multimode signals," *Journal of the Acoustical Society of America*, vol. 89, no. 3, pp. 1159–1168, March 1991.

[106] R. W. Morse, "The velocity of compressional waves in rods of rectangular cross section," *Journal of the Acoustical Society of America*, vol. 22, no. 2, pp. 219–223, March 1950.

[107] V. V. Meleshko, A. A. Bondarenko, A. N. Trofimchuk, and R. Z. Abasov, "Elastic waveguides: History and the state of the art II," *Journal of the Mathematical Sciences*, vol. 167, no. 2, pp. 197–216, May 2010.

[108] A. A. Krushynska and V. V. Meleshko, "Normal waves in elastic bars of rectangular cross section," *Journal of the Acoustical Society of America*, vol. 129, no. 3, pp. 1324–1335, March 2011.

[109] D. Vaughan and J. Mould, *PZFlex Time Domain Finite Element Analysis Package*. Los Altos: Weidlinger Associates Inc., 2003.

[110] F. Garofalo, "Temperature dependence of the elastic moduli of several stainless steels," *Proc. ASTM*, vol. 60, no. 1, pp. 738–749, July 1960.

[111] *Austenitic Chromium-Nickel Stainless Steels at Elevated Temperatures - Mechanical and Physical Properties (INCO 2980)*, INCO Ltd., 1968.

[112] S. Patankar, *Numerical Heat Transfer and Fluid Flow*. London: Taylor & Francis, 1980.

[113] R. H. Pletcher, J. C. Tannehill, and D. A. Anderson, *Computational Fluid Mechanics and Heat Transfer*. London: Taylor & Francis, 2011.

[114] A. Pesavento, C. Perrey, M. Krueger, and H. Ermert, "A time-efficient and accurate strain estimation concept for ultrasonic elastography using iterative

phase zero estimation," *Ultrasonics, Ferroelectrics, and Frequency Control, IEEE Transactions on*, vol. 46, no. 5, pp. 1057–1067, September 1999.

[115] J. F. Figueroa and J. S. Lamancusa, "A method for accurate detection of time of arrival: Analysis and design of an ultrasonic ranging system," *The Journal of the Acoustical Society of America*, vol. 91, no. 1, pp. 486–494, January 1992.

[116] S. Dixon, C. Edwards, and S. B. Palmer, "High accuracy non-contact ultrasonic thickness gauging of aluminium sheet using electromagnetic acoustic transducers," *Ultrasonics*, vol. 39, pp. 445–453, October 2001.

[117] G. Kossoff, "The effects of backing and matching on the performance of piezoelectric ceramic transducers," *Sonics and Ultrasonics, IEEE Transactions on*, vol. 13, no. 1, pp. 20–30, March 1966.

[118] A. J. Mulholland, N. Ramadas, R. L. O'Leary, A. C. S. Parr, G. Hayward, A. Troge, and R. A. Pethrick, "Enhancing the performance of piezoelectric ultrasound transducers by the use of multiple matching layers," *IMA Journal of Applied Mathematics*, vol. 73, no. 6, pp. 936–949, December 2008.

[119] C. Desilets, J. Fraser, and G. S. Kino, "The design of efficient broad-band piezoelectric transducers," *Sonics and Ultrasonics, IEEE Transactions on*, vol. 25, no. 3, pp. 115–125, May 1978.

[120] P. Javorsky, F. Wastin, E. Colineau, J. Rebizant, P. Boulet, and G. Stewart, "Low-temperature heat capacity measurements on encapsulated transuranium samples," *Journal of Nuclear Materials*, vol. 344, no. 13, pp. 50 – 55, September 2005.

[121] "Thermal contact resistance between high-tc superconductor and copper," *Physica C: Superconductivity*, vol. 357360, no. 1, pp. 785 – 788, September 2001.

[122] F. Rondeaux, P. Bredy, and J. M. Rey, "Thermal conductivity measurements of epoxy systems at low temperature," *AIP Conference Proceedings*, vol. 614, no. 1, pp. 197–203, July 2002.

[123] S. Lees and C. Davidson, "Ultrasonic measurement of some mineral filled plastics," *Sonics and Ultrasonics, IEEE Transactions on*, vol. 24, no. 3, pp. 222–225, May 1977.

[124] J. M. Pelmore, "Acoustice impedance of composite materials," *Acoustics Letters*, vol. 3, no. 3, pp. 65–68, 1979.

[125] M. G. Grewe, T. R. Gururaja, T. R. Shrout, and R. E. Newnham, "Acoustic properties of particle/polymer composites for ultrasonic transducer backing applications," *IEEE Transactions Ultrasonics Ferroelectrics Frequency Control*, vol. 37, no. 6, pp. 506–514, November 1990.

[126] C. Lee, M. Lahham, and B. Martin, "Experimental verification of the kramers-kronig relationship for acoustic waves," *Ultrasonics, Ferroelectrics, and Frequency Control, IEEE Transactions on*, vol. 37, no. 4, pp. 286–294, July 1990.

[127] W. Sachse and Y. H. Pao, "On the determination of phase and group velocities of dispersive waves in solids," *Journal of Applied Physics*, vol. 49, no. 8, pp. 4320–4327, August 1978.

[128] P. He and J. Zheng, "Acoustic dispersion and attenuation measurement using both transmitted and reflected pulses," *Ultrasonics*, vol. 39, no. 1, pp. 27 – 32, January 2001.

[129] G. S. Kino and R. Baer, "Theory for cross-coupling," in *Proceedings of 1983 IEEE International Ultrasonics Symposium*, vol. 1, October 1983, pp. 1013–1019.